NAVAL POSTGRADUATE SCHOOL

MONTEREY, CALIFORNIA

THESIS

ENERGY HARVESTING THROUGH WAVE MOTION

by

Matthew C. Peshek

June 2022

Thesis Advisor: Young W. Kwon
Co-Advisors: Jarema M. Didoszak
Joseph T. Klamo

THIS PAGE INTENTIONALLY LEFT BLANK

REPORT DOCUMENTATION PAGE			*Form Approved OMB No. 0704-0188*

1. AGENCY USE ONLY *(Leave blank)*	**2. REPORT DATE** June 2022	**3. REPORT TYPE AND DATES COVERED** Master's thesis

4. TITLE AND SUBTITLE
ENERGY HARVESTING THROUGH WAVE MOTION

5. FUNDING NUMBERS

6. AUTHOR(S) Matthew C. Peshek

7. PERFORMING ORGANIZATION NAME(S) AND ADDRESS(ES)
Naval Postgraduate School
Monterey, CA 93943-5000

8. PERFORMING ORGANIZATION REPORT NUMBER

9. SPONSORING / MONITORING AGENCY NAME(S) AND ADDRESS(ES)
N/A

10. SPONSORING / MONITORING AGENCY REPORT NUMBER

11. SUPPLEMENTARY NOTES The views expressed in this thesis are those of the author and do not reflect the official policy or position of the Department of Defense or the U.S. Government.

12a. DISTRIBUTION / AVAILABILITY STATEMENT
Approved for public release. Distribution is unlimited.

12b. DISTRIBUTION CODE
A

13. ABSTRACT (maximum 200 words)

Wave energy has the potential to become a large source of renewable energy, but there is no consensus on the most efficient mode of extracting power. One major component of all wave energy converters (WECs) is the power take off (PTO) mechanism, which converts the absorbed energy of the system to useful power. Triboelectric nanogenerators (TENGs) generate electricity through friction of two dissimilar materials, and previous studies have shown potential for this technology to be used as a PTO mechanism. This study tested different models of a horizontal-axis hydro turbine in order to evaluate the performance of a rotational TENG in the ocean environment. The hydro turbine models were tested in the tow tank to observe how much rotation can be produced by incoming waves and how each model parameter impacted the performance or rotational speed. The conclusions drawn from the experiment were used to determine how a similar model could be realistically implemented on unmanned undersea vehicles (UUVs). The number of blades on the hydro turbine most significantly impacted performance, and single blade models had the highest average angular speed compared to any other model.

14. SUBJECT TERMS	**15. NUMBER OF PAGES**
triboelectricity, wave energy, hydro turbine, renewable energy, wave energy converter, WEC, power take off, PTO, triboelectric nanogenerator, TENG, unmanned undersea vehicle, UUV	123
	16. PRICE CODE

17. SECURITY CLASSIFICATION OF REPORT	**18. SECURITY CLASSIFICATION OF THIS PAGE**	**19. SECURITY CLASSIFICATION OF ABSTRACT**	**20. LIMITATION OF ABSTRACT**
Unclassified	Unclassified	Unclassified	UU

NSN 7540-01-280-5500

Standard Form 298 (Rev. 2-89)
Prescribed by ANSI Std. 239-18

THIS PAGE INTENTIONALLY LEFT BLANK

Approved for public release. Distribution is unlimited.

ENERGY HARVESTING THROUGH WAVE MOTION

Matthew C. Peshek
Ensign, United States Navy
BS, United States Naval Academy, 2021

Submitted in partial fulfillment of the
requirements for the degree of

MASTER OF SCIENCE IN MECHANICAL ENGINEERING

from the

NAVAL POSTGRADUATE SCHOOL
June 2022

Approved by: Young W. Kwon
Advisor

Jarema M. Didoszak
Co-Advisor

Joseph T. Klamo
Co-Advisor

Garth V. Hobson
Chair, Department of Mechanical and Aerospace Engineering

THIS PAGE INTENTIONALLY LEFT BLANK

ABSTRACT

Wave energy has the potential to become a large source of renewable energy, but there is no consensus on the most efficient mode of extracting power. One major component of all wave energy converters (WECs) is the power take off (PTO) mechanism, which converts the absorbed energy of the system to useful power. Triboelectric nanogenerators (TENGs) generate electricity through friction of two dissimilar materials, and previous studies have shown potential for this technology to be used as a PTO mechanism. This study tested different models of a horizontal-axis hydro turbine in order to evaluate the performance of a rotational TENG in the ocean environment. The hydro turbine models were tested in the tow tank to observe how much rotation can be produced by incoming waves and how each model parameter impacted the performance or rotational speed. The conclusions drawn from the experiment were used to determine how a similar model could be realistically implemented on unmanned undersea vehicles (UUVs). The number of blades on the hydro turbine most significantly impacted performance, and single blade models had the highest average angular speed compared to any other model.

THIS PAGE INTENTIONALLY LEFT BLANK

Table of Contents

List of Figures

THIS PAGE INTENTIONALLY LEFT BLANK

List of Tables

THIS PAGE INTENTIONALLY LEFT BLANK

List of Acronyms and Abbreviations

AI	Artificial Intelligence
ISR	Intelligence, Surveillance, and Reconnaissance
NPS	Naval Postgraduate School
PTO	Power Take-Off
TENG	Triboelectricity Nanogenerator
USN	U.S. Navy
USW	Undersea Warfare
UUV	Unmanned Undersea Vehicle
WEC	Wave Energy Converter
PLA	Polylactic Acid

THIS PAGE INTENTIONALLY LEFT BLANK

Acknowledgments

I would like to thank Dr. Kwon, Professor Didoszak, and Professor Klamo for their guidance during my thesis research. This project was very exploratory in nature, and their advice allowed me to thoroughly investigate this topic. I would also like to thank my roommates, Alex Richmond and Andrew Waldron, for their help throughout my year at NPS.

THIS PAGE INTENTIONALLY LEFT BLANK

CHAPTER 1:
Introduction

1.1 Motivation

The future of Undersea Warfare (USW) will rely on unmanned systems. Submarines and other stealth platforms thrive in the vast ocean environment, but this domain inhibits effective communication and thus real-time command and control. Also, several mission sets that require extensive data collection, that are high cost, or that are an increased risk for human personnel make undersea warfare a promising domain for technological integration. Therefore, Artificial Intelligence (AI) and advanced systems such as an Unmanned Undersea Vehicles (UUVs) will be used to "extract and exploit actionable patterns among an ocean of data" [1]. Over the past three decades, UUV technology has become a prominent component in Navy and submarine force operations, and will continue to play a major role due to its ability to provide increased battlespace awareness for manned platforms, produce a quantitative threat to deny adversaries' use of the undersea, respond to asymmetric threats such as mines while limiting the risk of human lives, strike warfare, and more. While UUVs utilize advanced AI technology, they are relatively inexpensive and can conduct missions on the seabed and in depths that submarines cannot operate under.

However, significant improvements need to occur, specifically in UUV speed and endurance, in order to enable longer range UUV tracking and forward deployed operations. These limitations restrict its capability to either be long range or duration Intelligence, Surveillance, and Reconnaissance (ISR) missions, or missions close to its "mother ship", land, or certain chokepoints. While UUV's still provide a useful benefit to a ship or submarine in its anti-submarine and ISR missions, these factors render its capability less useful in time critical missions.

One potential solution to increasing UUV operational endurance and duration is through renewable energy harvesting, specifically from waves. Wave energy has the capability to provide 2 TW of energy throughout the world [2], and is the most available source of energy for undersea vehicles. Wave Energy Converters (WECs) possess Power

Take-Off (PTO) mechanisms that are used to convert wave motion to useful power, and one possible form of PTO is through a Triboelectricity Nanogenerator (TENG). TENGs have the capability of extracting wave energy through relative contact motion between two compatible materials, and this available power would be able to charge a UUV's battery or at least maintain its charge while in a lower power loiter mode. The wave motion at or under the surface would cause contact friction between the two materials and produce electricity. A benefit of this type of renewable energy is the fact that this recharging can be done below the surface. This would allow for some stealth and protection from the harsh open ocean environment. Previous studies at the Naval Postgraduate School (NPS) have investigated the benefits of a TENG that utilizes rotational motion as compared to linear sliding, so this study ultimately investigated the ability of a rotational TENG to be integrated in on-board UUV wave energy conversion by designing, modeling, and testing a hydro turbine PTO mechanism.

1.2 Literature Review

A literature review was conducted in order to investigate methods currently employed in TENG and wave energy conversion. This influenced how a WEC would be designed to convert wave energy to mechanical motion and thus optimize the rotational TENG.

1.2.1 Review of TENG and Applications

Triboelectricity is often referred to as static electricity, and it occurs due to two dissimilar materials rubbing against each other and exchanging electrons from one material to the other, balancing the potential difference [3]. A chemical bond between parts of the surfaces is formed due to the contact, and this allows the charges to be transferred [3]. This effect can be seen in everyday life, including rubbing your head with a balloon or receiving a shock from a door knob. A TENG attempts to use this effect to create useful power for smaller scale devices. One of the most important design decisions in the process of creating a TENG model is the two materials that are in contact with each other. The triboelectric series lists materials in order (from top to bottom) of their tendency to acquire a positive charge [4]. In other words, more positive materials (top) would be more willing to lose electrons to more negatively charged materials (bottom), and the materials in the middle of the series do not want to give or receive any electrons. This means that the triboelectric effect will

occur more prominently between two materials far away from each other on the triboelectric series. In summary, a TENG needs two compatible materials on the triboelectric series and contact motion between the two materials to create useful electricity.

There are four principle modes in which a TENG will generate an electric charge. They are vertical contact-separation, contact-sliding, single-electrode, and freestanding triboelectric layer as seen in Figure 1.1 [5].

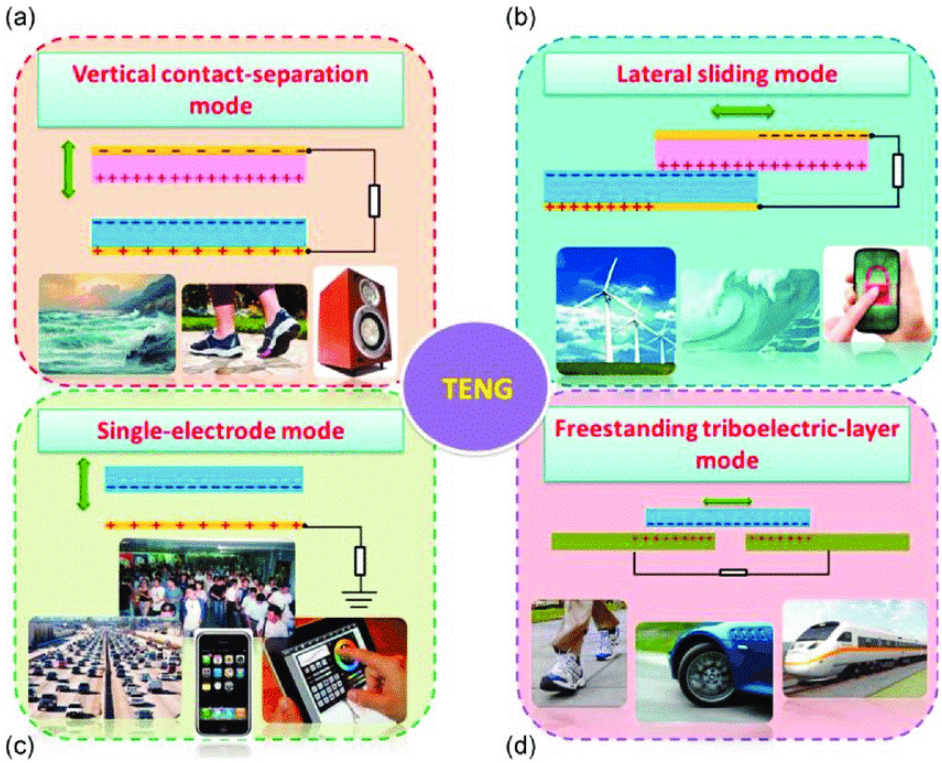

Figure 1.1. TENG Principle Modes. Source: [5].

In the vertical contact separation-mode, there are two metal electrodes and a dielectric film. During movement, the top electrode will become positively charged, the dielectric will become negatively charged, and once the two materials are separated, the electrons will flow from the bottom electrode to the top electrode due to the potential difference [5]. The lateral sliding mode is very similar, except that the two dielectrics are in contact, and their

separation is what causes the potential difference. The single-electrode mode only has a bottom electrode that is connected to the ground, and in the freestanding triboelectric mode, the dielectric is the moving component.

TENGs have been used to harness energy in several different sources such as from walking (foot and arm motion), wind, vibration, finger tapping, and more [5]. Most previous research focuses on power sources at the micro-scale due to its availability in everyday life and its ability to be lightweight and cost-effective. In order to scale TENGs to the macro-scale, the energy sources would have to be greater. Current research that is focusing on larger size TENG models includes energy sources from the ocean or rivers. Also, due to its low current output, arrays of TENGs in parallel have been proposed to increase the total harvested electricity [5].

While TENG design is not a focus of this study, it is important to understand how TENG could work as a PTO mechanism and how to convert the energy source to motion that would optimize this technology.

1.2.2 Previous NPS TENG Design

The most recent TENG design iteration from NPS is a rotational model designed and constructed by LT June Capelle, as seen in Figures 1.2 and 1.3 [6].

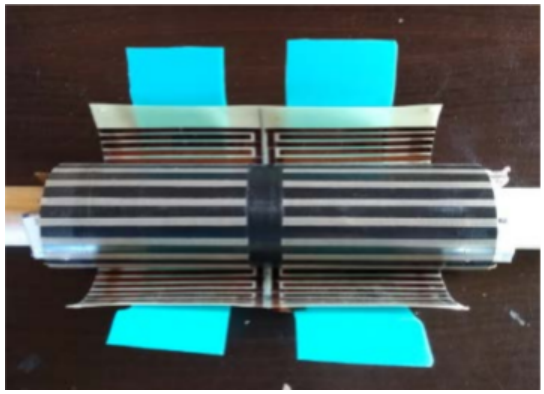

Figure 1.2. NPS TENG Design (Internal). Source: [6].

Figure 1.3. NPS TENG Design (External). Source: [6].

This TENG design utilizes the freestanding triboelectric-layer mode, which generates alternating voltage and current. Copper foil tape is used as the electrode medium and Teflon tape is the dielectric medium. The cylindrical hardwood serves as a shaft that rotates the Teflon tape and thus causes the triboelectric effect to occur. The main concept of this design is that the external energy source rotates the Teflon (inner layer), the Teflon rubs against the copper, and then the charge build-up in the copper is stored using a capacitor or displayed using LEDs.

Different iterations of the model based on the copper and Teflon width and spacing were tested using a DC motor or a bicycle as the external energy source. Voltage, current, frequency, and shaft rotational speed were measured. This study does not attempt to significantly alter the design of this TENG; it is more focused on the concept of this design and its integration to wave energy. Using the DC motor, the TENG models were capable of charging a 10 μF capacitor in 171 seconds at 125 RPM, and the highest rated design iteration was able to generate 126 VAC at 37 Hz for the generated AC voltage at a motor speed of 180 RPM [6]. These values were concluded to be practical for use in everyday applications.

This study provides a baseline on the performance of the TENG in optimal conditions. The rotation of the shaft and the performance of the PTO mechanism depend on the waves as an energy source. In a practical application, there would be losses between the

input energy and the rotation of the model. This study did not assess the efficiency of the design in regards to the energy input required to charge the 10 μF capacitors.

1.2.3 Wave Energy and Wave Energy Converters

In order to determine how to best extract energy from a water wave, a review of wave energy and current WEC technology was conducted. Figure 1.4 provides an illustration about how wave energy propagates in water [7].

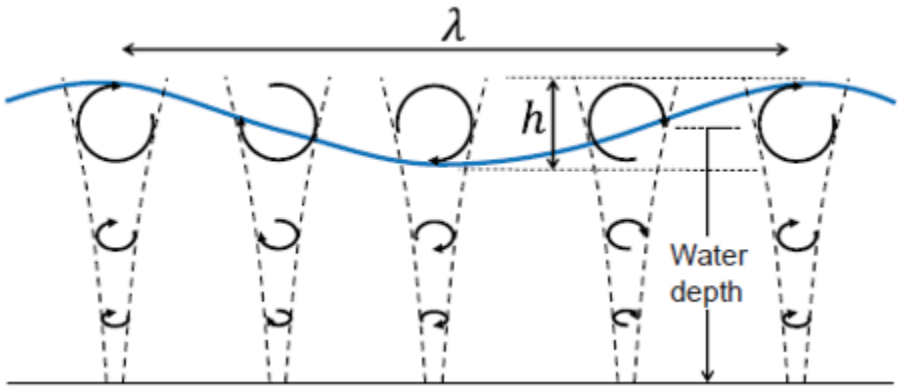

Figure 1.4. Wave Energy Propagating in Water. Source: [7].

As seen in Figure 1.4, fluid particles travel in an orbital motion and the energy from the wave decays exponentially with the depth of water. The influence of the wave travels as far as one half of the wavelength and the flow is irrotational [7]. Therefore, the flow does not provide the torque required to rotate a conventional drag turbine. This is significant because in a below surface application, a typical turbine would not provide a high efficiency or power output. Also, the closer the turbine or energy converter is to the surface, the more power that could be potentially extracted out of the wave.

There are many different types of WECs, which are utilized based on conditions such as the distance from the shore, size of the WEC, and how it extracts energy from a wave. Most WECs extract energy through heave (vertical), surge (horizontal), or pitch (rotational) motion. In the context of providing localized power to a UUV where the energy harvesting

can occur both in the open ocean and near the shore, the main types of WECs are attenuators, point absorbers, and an oscillating water column. Figure 1.5 provides illustrations of each type of WEC [8].

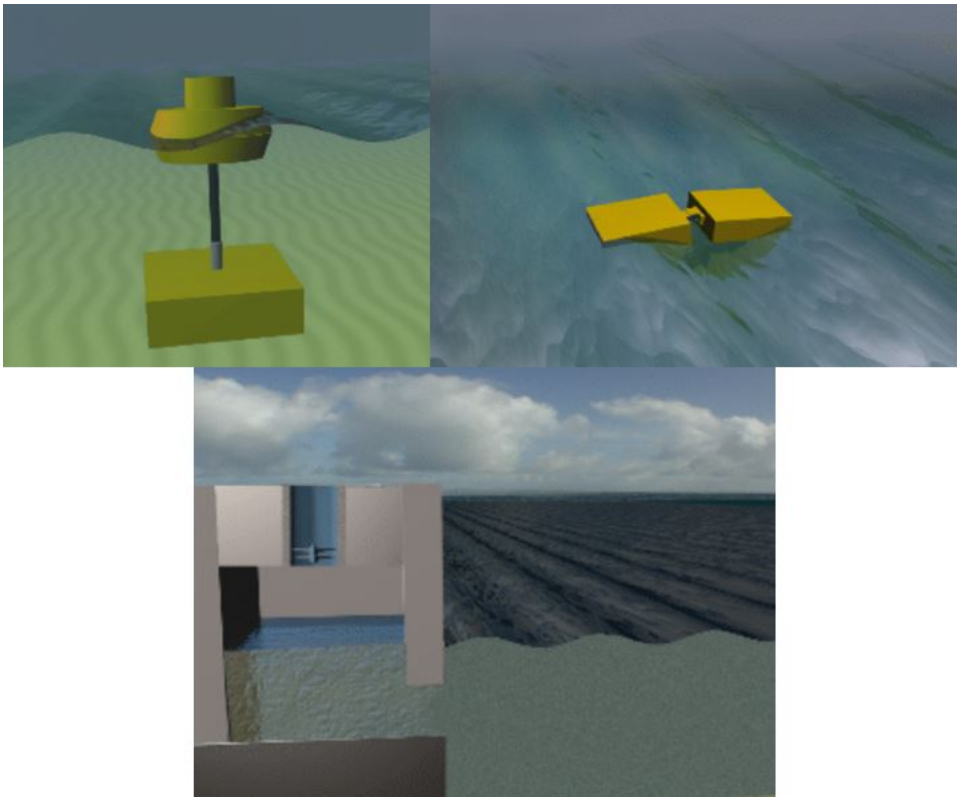

Figure 1.5. Main Types of WECs: Point Absorber (left), Attenuator (right), Oscillating Water Column (bottom) Source: [8].

Point absorbers can be either floating or submerged, and it involves a body absorbing the motion in heave and/or sway. Attenuators are oriented parallel to the incident waves, and capture energy from the relative motion of the two arms [8]. An oscillating water column uses a water column to compress and decompress the air in the column, which causes a turbine to spin [8]. In general, the power absorption of attenuators and point absorbers are rated as energy per unit width of the incident wave (W/m). Therefore, the wider the WEC is along the incident wave, the more energy that can be potentially captured. These WECs

are all paired with a PTO mechanism that converts the relative motion of the body to useful power.

Using TENG as a PTO for wave energy is not a novel idea, as the original design using a network a TENGs was created by the SKKU Advanced Institute of Nanotechnology (Figure 1.6) [9].

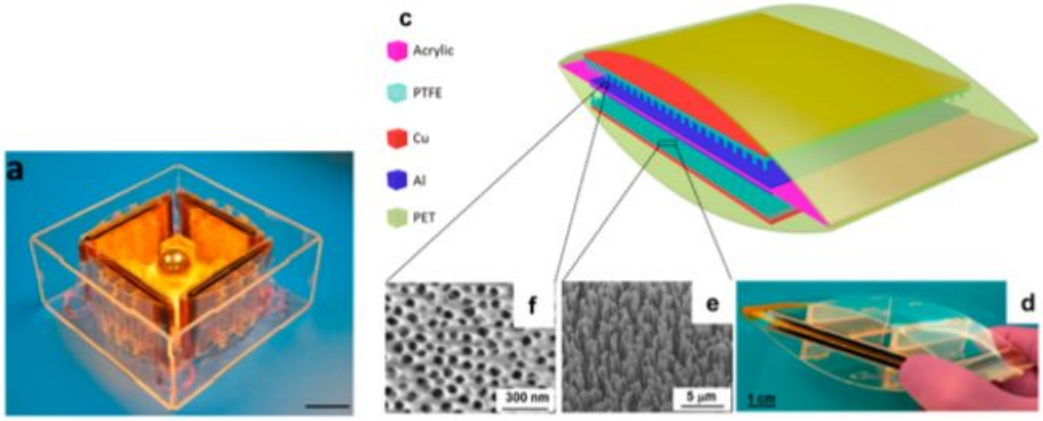

Figure 1.6. TENG for Wave Energy Harvesting Design. Source: [9].

This design featured a box structure with walls of arch-shaped TENGS with a metal ball enclosed. The metallic balls would collide with the arch-shaped TENGs, and that motion would produce power. With a network a four TENGs, it produced 200V, a current of 320μA, and a peak power of 60 mW [9]. The benefit of this technology is that it is lightweight, cheap, and can convert the power from the random frequencies and forces of waves in an ocean environment. However, there are still some challenges with this technology. For example, the electrodes are not water-proof, so durability is an issue when in a harsh ocean environment. Also, due to its relatively low currents, a network of TENGs in parallel is required for more significant power output. Lastly, since the power from ocean waves is irregular, TENGs are limited to storing energy in batteries and then made available for larger-scale applications instead of simply connecting them to the power grid. The use of TENG in this applications was at a small scale so utilizing the method in the previous NPS work would provide energy at a more relevant scale for UUVs.

1.2.4 Hydro-Turbine Designs

Hydro-turbines are used in electricity-generating systems, and their motion typically drives a shaft. Since the previous TENG from NPS involved rotating a shaft connected to the inner Teflon layer, research into hydro-turbine design was conducted to determine characteristics of an efficient design for an onboard UUV WEC system. Figure 1.7 displays the most common types of hydro-turbines [10].

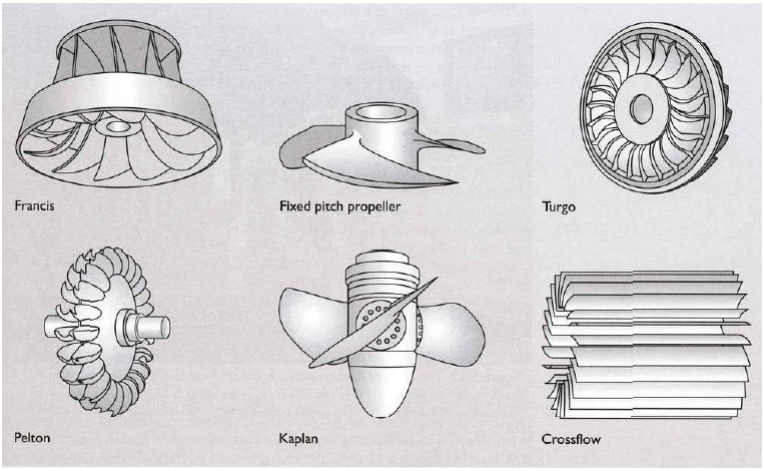

Figure 1.7. Hydro-Turbine Designs. Source: [10].

As previously discussed, the orbital flow in water waves is irrotational and does not provide torque for the conventional drag turbines, so the only types of hydro-turbines that could potentially work in this situation is the Kaplan or crossflow type turbines. The Kaplan design would allow a large surface area in the blades to catch the water waves, but the crossflow turbines would best utilize the orbital motion of the wave. The most common use of crossflow turbines is shown in Figure 1.8 [11].

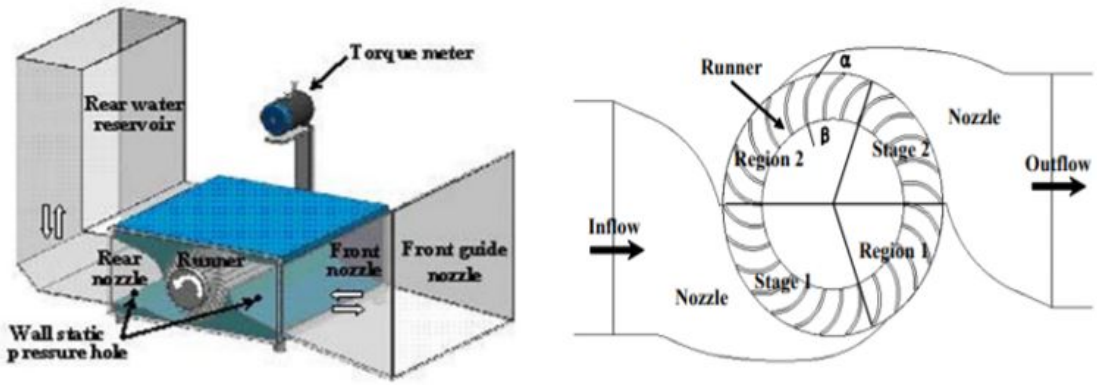

Figure 1.8. Direct Drive Hydro-Turbine WEC. Source: [11]

In this design, the flow is ducted into a nozzle in order to increase the velocity of the water hitting the blades. The benefit of this design is that the water goes through the turbine twice, creating a higher efficiency. Adding a nozzle to the crossflow turbine ultimately increases the rotational speed, but in regards to a UUV design, a nozzle capturing a large mass flow of water would interfere with the mobility of the UUV. Also, this design relies more heavily on a flow of water into the nozzle, and in this case, the orbital motion would make it difficult to replicate this concept. A similar crossflow type turbine was designed by Waterotor and was made for slow moving currents in Figure 1.9 [12].

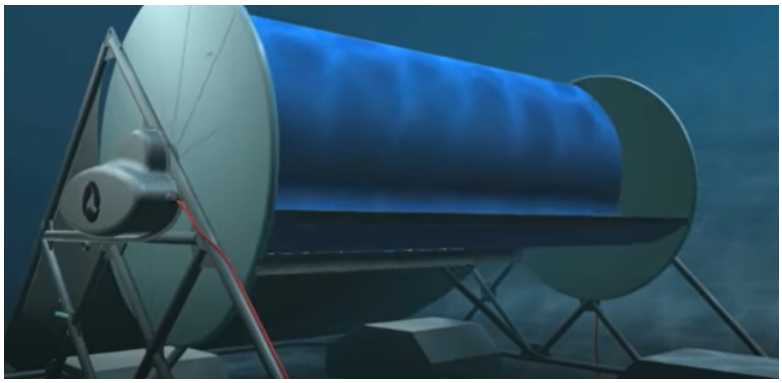

Figure 1.9. Waterotor WEC. Source: [12].

This design does not have a nozzle to increase the velocity of the flow, but it relies on slow moving currents that are perpendicular to the turbine blades. It can achieve a high energy output at current speeds as slow as 0.894 to 2.68 meters per second [12], but it is mainly deployable in flowing rivers and streams. While this type of hydro-turbine has potential to rotate due to water waves, it was designed for horizontal fluid flow. Figure 1.10 displays a "single bucket" approach to utilize orbital fluid motion [7].

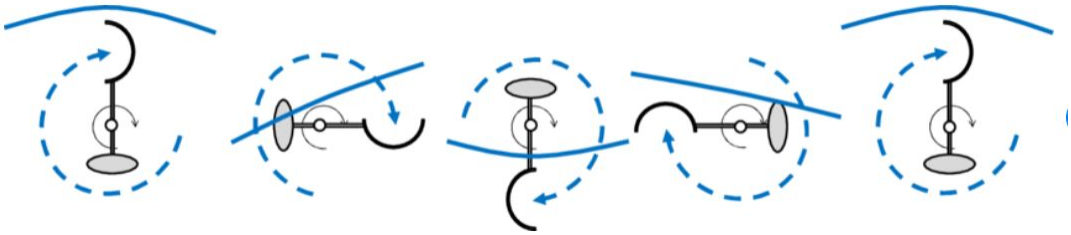

Figure 1.10. Single-Bucket Wave Turbine. Source: [7].

The solid blue lines represent the water surface and the dotted lines are the instantaneous wave velocity at the bucket position. The design features a torque control system in order to account for a load from the PTO system. The counterweight on the opposite end of the bucket allows the turbine to rotate in synchronization with the wave, and therefore keep the correct angle to rotate the turbine. When there is a controlled load from a PTO mechanism, the "rotation of the turbine delays and the bucket will maintain the correct angle" [7]. However, Akimoto et al [7] calculated that the conversion efficiency for this system was only 4.5% at wave heights of 0.20 meters. They concluded that this was satisfactory due to its compact and lightweight design. This was the first researched turbine that relied on the orbital motion of the wave and operated just below the free surface. In terms of applying this concept to a UUV, the bucket would significantly alter the hydrodynamics of the vehicle. Therefore, a system to deploy the buckets and counterweight would be required. Also, in this experiment, it was assumed that the wavelength from the ocean wave was in tune with the bucket system. In other words, the diameter of the orbital motion of the particles would constantly provide positive force on the bucket. In a UUV situation, the wavelength would be much greater than the diameter of the model. Therefore, there might be positions where the wave is not contributing towards rotation.

Figure 1.11 displays a traditional propeller design from the Okinawa Institute of Science and Technology (OIST) to harvest wave energy along the Japan coastline [13].

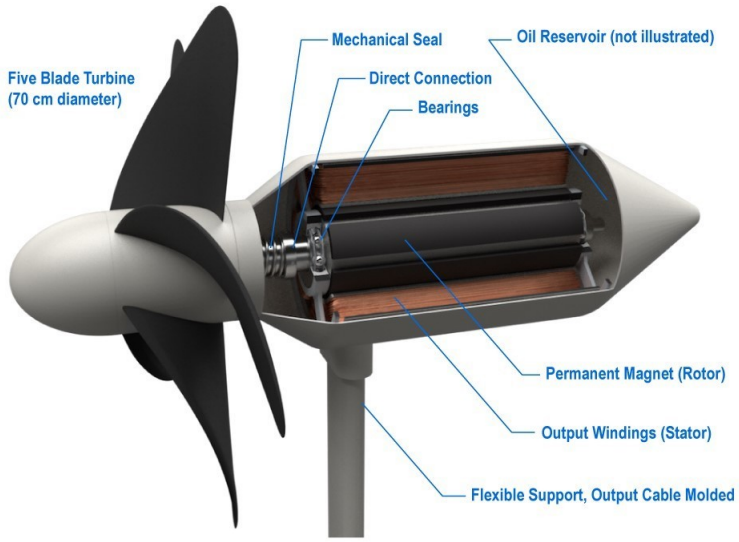

Figure 1.11. OIST Turbine. Source: [13].

These turbines are placed just above sea level so the waves could wash over them, and each turbine would have five blades. As the blades spin, the shaft rotates and creates electricity through a permanent magnet electric generator [13]. This system also has a ceramic body that protects the electric components from sea water. While the efficiency of a single turbine is not analyzed, it is suggested that a large array of turbines could produce gigawatts of energy [13]. While this turbine is designed for crashing waves, the large surface area of the blades would allow them to rotate. Also, this design rotates a shaft, and the shaft would be the inner Teflon layer of the TENG is this application. In comparison, the outer portion of the crossflow turbine would have to be the outer layer of the TENG itself. All in all, more investigation would be required to determine the effectiveness of this design compared to a crossflow turbine. Figure 1.12 illustrates a horizontal axis turbine designed by Maldar et al. [14].

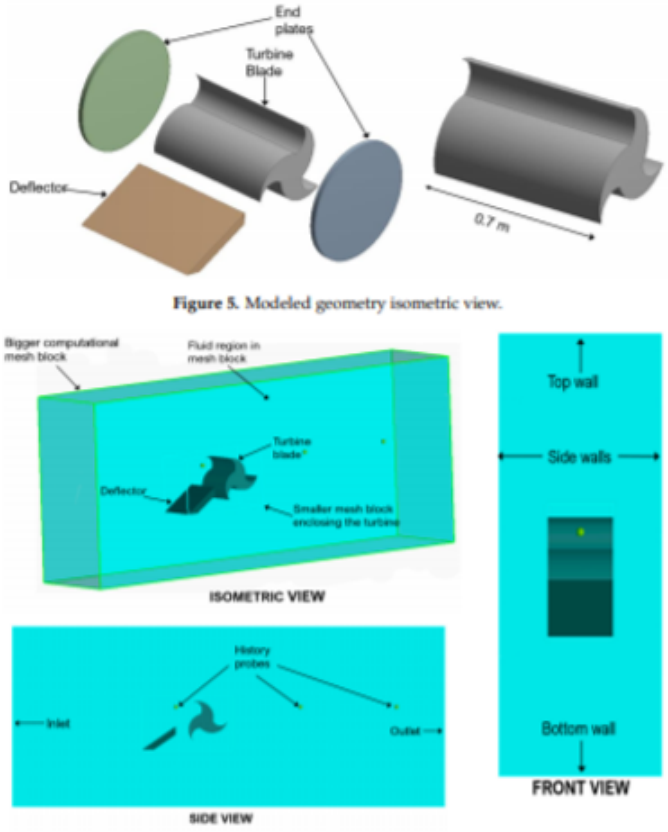

Figure 1.12. Horizontal Axis Ocean Current Turbine with Deflector. Source: [13].

This turbine operates similarly to the other crossflow designs, but it also includes a deflector. The deflector redirects the ocean current to better angle the flow onto the blades. The optimum angle of the deflector depends on the geometry of the turbine, and needs to be experimentally determined. It was calculated that the presence of a deflector increased the torque of the system by 30% [13]. While the use of a deflector would increase the overall power output of a hydro-turbine, it would be difficult to implement into an on-board UUV system without interfering with the hydrodynamics of the vehicle.

1.2.5 Existing UUV Renewable Energy Technology

Harvesting renewable energy for UUV's is being currently utilized and researched, but mostly in the context of building a recharging station or hub. Solar power has been used previously, but some disadvantages to solar power include cloud cover, low altitude of the sun at higher latitudes and winter months, water damage to the photo-voltaic cells, and non-efficient angles to collect solar arrays. Thus, wave energy has the benefit of being the more reliable renewable energy source. An example of a UUV WEC design is the Triton WEC by Oscilla Power in Figure 1.13 [15].

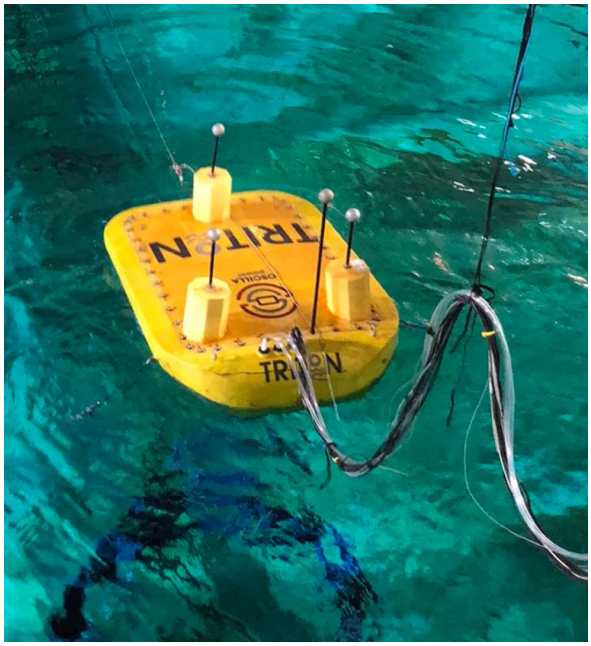

Figure 1.13. Triton WEC. Source: [15]

The Triton is a point-absorber WEC that floats on the surface of the water. It can extract energy in six degrees of freedom, which allows it to capture energy at various wave frequencies and ocean conditions. These hubs would be placed strategically throughout the ocean, and the UUV would be able to connect itself to the Triton under the water and recharge its batteries. While this extends UUV operations, a large infrastructure of these recharging stations would be required. In addition, they would not be able to be deployed

in contested waters, as adversaries would destroy this technology. Therefore, even though on-board WEC technology would be less efficient than a recharging station for a UUV, it would extend its operations while also making it more independent.

1.2.6 Current Number of Blades and Curvature of Blade Studies

The efficiency of a drag based turbine was studied by Pei et al. [16]. In this study, a water faucet was placed directly under the turbine model as seen in Figure 1.14, and the rotational speed was measured. Multiple different turbine models were tested with varying number of blades and curvature of the blades.

Figure 1.14. Number of Blades and Curvature Drag Turbine Experimental Set-up. Source: [16].

There are several differences in this study and what was researched in this thesis. First, this experiment only had one blade impacted by the flow at a time. In a wave environment, each blade will most likely have some effect, positive or negative, on the rotation of the entire turbine. Also, the fluid flow in a wave will not resemble the faucet flow seen in the figure. Figure 1.15 details the results that were seen from the experiment.

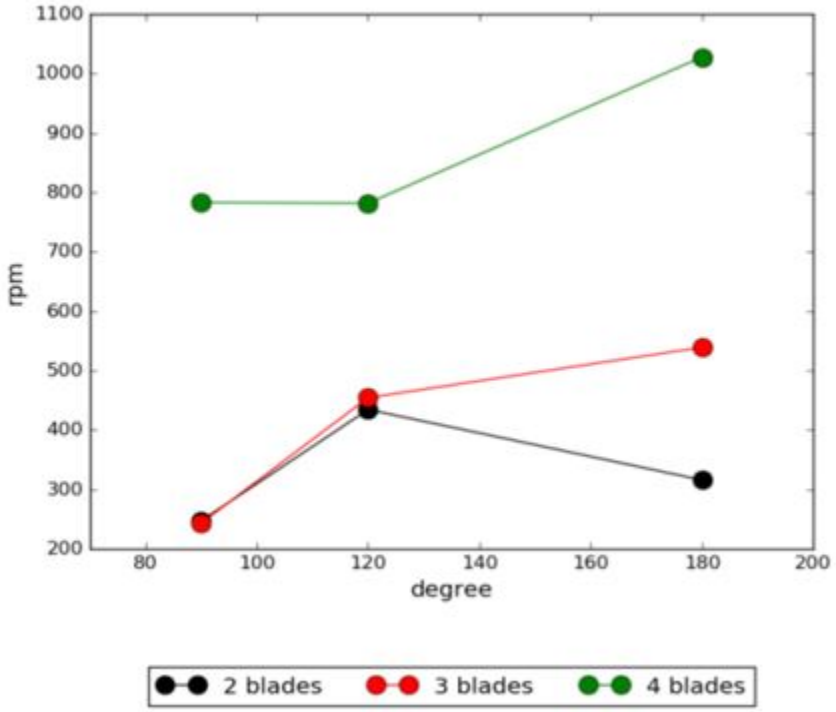

Figure 1.15. Number of Blades and Curvature Drag Turbine Experiment Results. Source: [16]

the x-axis is the curvature of the blade, where 90 degrees is a flat and 180 degrees is a semi-circle. The rotational speed in rpm was measured from the constant flow. There was a significant increase in rotational speed with four blades as compared to three and two, and the greater curvature of the blades also increased the speed for most cases. If the water was able to encounter a blade more frequently, then it resulted in more rotational speed. The results from this experiment suggested that the number of blades and the blade geometry had an influence on rotational speed.

CHAPTER 2:
Experimental Process

2.1 Objective and Experiment Matrix

The objective of this study is to understand how a fully submerged, wave-powered hydro turbine performs in multiple conditions. In addition, the design parameters, such as blade size and number of blades, along with the wave environment, specifically wavelength and wave height, were iterated in order to understand how they impacted the rotational speed and behavior. Ultimately, the observations influenced the design of a wave-powered rotational TENG. The "performance" of a model relates to the amount of rotation that occurred from the waves. The more rotation, or rotational speed, results in a greater number of electrons transferred between the two materials in the TENG.

Based on of the lessons learned in the literature review, a horizontal axis turbine, similar to the one in Figure 1.12, was decided to be the used in the experiment. Theoretically, a horizontal axis turbine would be able to rotate due to the circular motion of an ocean wave, unlike common propeller designs. A diagram of the tested model is shown in Figure 2.1.

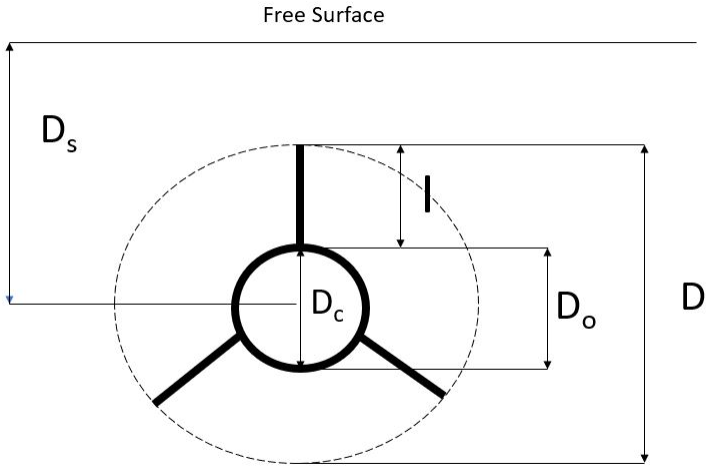

Figure 2.1. Diagram of Model and Variable Abbreviations

The waves would travel from right to left of the diagram, which would create counterclockwise rotation. This diagram features the model with three straight blades, but those parameters were subject to change in the experiment. D_s is the submergence depth from the free surface to the axis of rotation of the model, I is the single blade length, D_o is the outer diameter of the base, and D is total diameter of the model. The center diameter D_c represents the hollow portion of the body of the model.

To determine the optimal design for this turbine, the following parameters were tested:

- D_o
- Wave Height, H
- Wavelength, λ
- D/D_o Ratio
- Submergence Depth
- Number of Blades
- Blade Separation Angle
- Blade Mass
- Blade Geometry/Moment of Inertia

This list influenced how a model was studied, and multiple different models were created in order to observe differing performance with differing parameters. It is important to note that this list does not include every parameter that could potentially impact the performance of the model. For example, the blade curvature and camber could also affect the rotation of the turbine. However, it was decided to maintain a straight and flat blade design for this study due to time constraints. Descriptions of all the tested models are shown in Table 2.1.

While the D_o values seem arbitrary, they were selected so the models could fit around 1/2", 3/4", and 1" Schedule 40 PVC pipe. The thickness of each model was also set at a fixed value of 0.16 cm. All of the models listed in Table 2.1 were not initially planned. Throughout the experimental process, more models were added to the table if it was determined that more data was necessary to observe any trends in the listed parameters.

To test how the submergence impacts the performance, two different test approaches

Table 2.1. Experimental Models

Number of Blades (#)	Blade Separation Angle (deg.)	D_o (cm)	D/D_o (—)
3	120	2.578	4
3	120	2.578	6
3	120	2.578	8
3	120	3.112	4
3	120	3.785	4
3	120	2.578	3
3	120	2.578	2
3	120	2.578	1.5
3	120	2.578	1.25
2	180	2.578	4
2	120	2.578	4
2	90	2.578	4
2	60	2.578	4
1	N/A	2.578	4
1	N/A	2.578	2
1	N/A	2.578	2.5

were conducted. First, multiple models were tested at two major depths below the free surface. Since the maximum orbital force from the wave should occur right before the free surface, the models were placed so the tip of the blade was directly below the trough of the wave. This would allow the model to maintain its submergence. The second depth was set at a fixed value of 13.335 cm. This allowed the largest blade size model to remain fully submerged while allowing a fixed position for all other models. The difference in this test was the distance from the blade to the free surface. The second submergence test took one model and tested it at varying depths until it no longer rotated due to the wave.

2.2 Facilities

The experiments were conducted in the 11 meter water tank in the NPS Hydro-Mechanics Laboratory. One side of the tank is made of aluminum frames with plexiglass windows that allow for easy viewing of the experiment. The tank is approximately 0.9441 meters in width with a nominal water depth of 0.9441 meters, and the waves are produced

by a wave-maker as seen in Figure 2.2.

Figure 2.2. Tank Wave-Maker

The tank is capable of producing 2.54 cm and 5.08 cm wave heights at wavelengths from 0.762 meters to 2.13 meters, and 7.62 centimeter waves from 1.68 meters to 1.98 meters. The models were tested in this range of wave heights and wavelengths to observe changes in performance due to these two variables. To create the waves, the front plate is pushed up and down by the apparatus at a certain frequency and amplitude. At the higher wave height and amplitude inputs, the wave maker wedge would attempt to oscillate faster, and the load on the apparatus would be greater than its limit. The wave maker would then stop the run prematurely. This was the reason why only three different wavelengths at a height of 7.62 cm were tested. Table 2.2 shows all of the inputs to the wave maker that were used to achieve the specified wave heights.

The waves were measured using a ruler against the plexiglass walls of the tank to ensure that wave heights were approximately accurate. At the end of the experiments, wave probes were placed in the tank to acquire accurate measurements of the wave height. The

Table 2.2. Wavemaker Inputs

Desired Height (cm.)	Desired Wavelength (meters)	Frequency Command (Hz)	P2P Amplitude Command (mm)
2.54	0.762	1.439	20.232
2.54	1.07	1.213	24.485
2.54	1.22	1.134	26.58
2.54	1.37	1.068	28.675
2.54	1.524	1.013	30.781
2.54	1.68	0.965	32.912
2.54	1.83	0.923	35.082
2.54	1.98	0.886	37.305
2.54	2.13	0.852	39.594
5.08	0.762	1.462	39.796
5.08	1.07	1.223	48.493
5.08	1.22	1.141	52.742
5.08	1.37	1.074	56.975
5.08	1.524	1.017	61.221
5.08	1.68	0.968	65.511
5.08	1.83	0.926	69.872
5.08	1.98	0.888	74.334
5.08	2.13	0.854	78.925
7.62	1.68	0.974	97.497
7.62	1.83	0.930	104.089
7.62	1.98	0.891	110.82

wave probes were used to measure the surface elevation in the tank after testing to more accurately determine the wave height that was achieved for each combination of commanded frequency and amplitude. Also, reflection inside the tank was a concern in the experiment. The waves could bounce off of the back wall and interfere with the incoming waves, which would create inaccurate wave heights. In order to reduce the effect, there is a "beach" located at the end of the tank as seen in Figure 2.3. The beach would absorb most of the energy from the incoming wave, so the effect of the reflection would be negligible by the time it reached the experimental apparatus at the other end.

Figure 2.3. Tank Beach

2.3 Experimental Set-Up

The general purpose of the experimental set-up was to submerge the model underneath the wave in a fixed state and revolve around the PVC pipe which ran through the hollow interior of the body. When this technology would be put into practice, this PVC pipe would be replaced by the body of a UUV. With a fixed PVC pipe, this assumes that the UUV would not be subjected to oscillations due to waves. While this is not practical to the real world situation, this variable was left out in order to better assess the performance of the model.

The model was created in SolidWorks, and printed using a Ultimaker 5 3D printer. The material used was Polylactic Acid (PLA). An example of one of the models is shown in Figure 2.4.

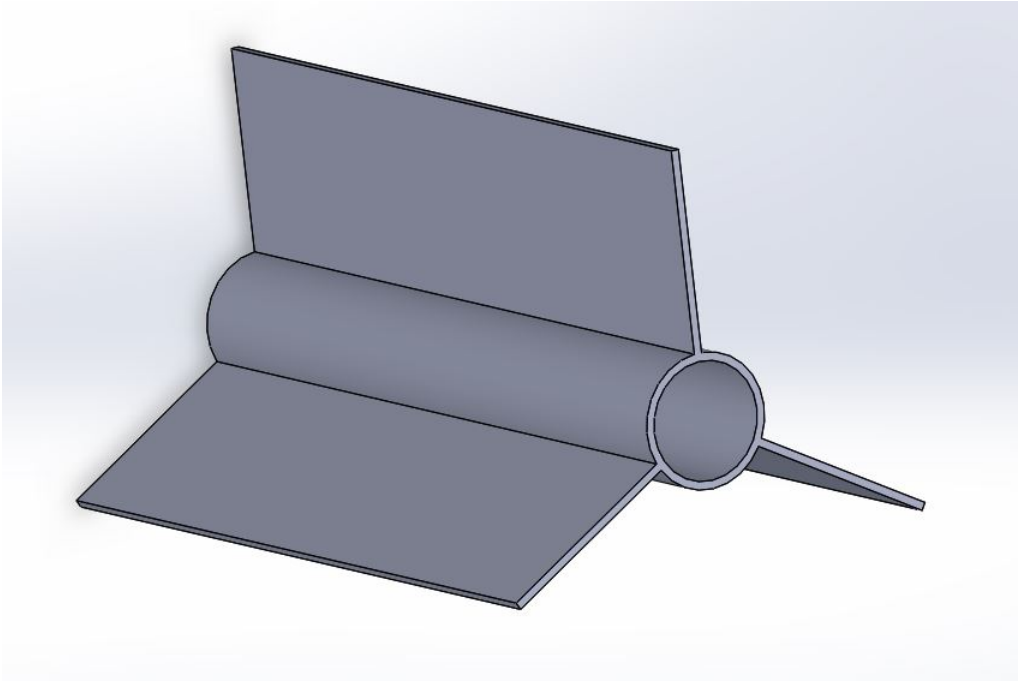

Figure 2.4. Example of Solidworks Model: D_o = 2.5781 cm, D/D_o = 4

The measurement for D_c was calculated by allowing a 0.127 centimeter tolerance between the PVC pipe and the model. This allowed smooth rotations without creating excess wobbling around the PVC. The width of each model was 15.24 centimeters. The energy of a wave is typically viewed in the units of W/m (per unit width). Therefore, the width of the piece would not theoretically matter. However, the width was chosen as a constant and to maintain compatibility with the experimental apparatus. The PVC was then connected to two end caps, which served as a joint between the PVC and two vertical 80/20 pieces. 80/20 is an extruded aluminum frame structure. The PVC was approximately 20 cm in order to reduce horizontal sliding of the model. The SolidWorks model of the end caps are shown in Figure 2.5. Separate end caps were printed for each unique model diameter.

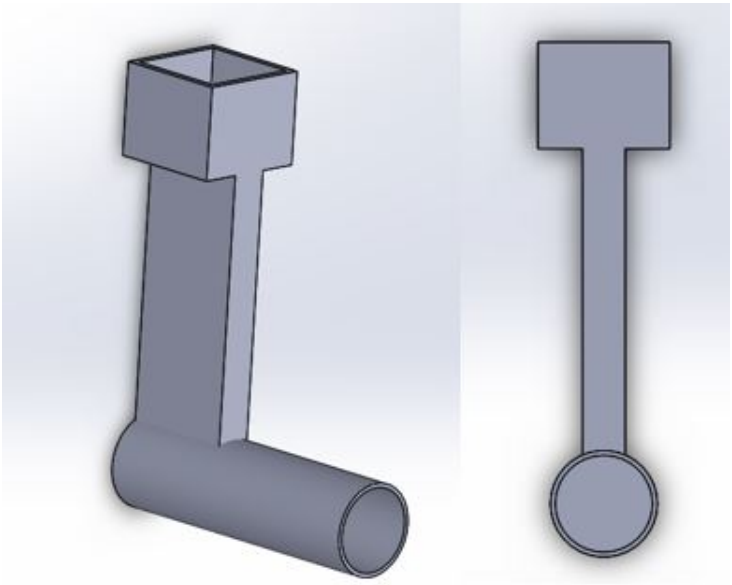

Figure 2.5. Solidworks Model of End Caps

The vertical 80/20 arms were connected to the bridge that spanned the width of the tank. In order to change the depth of the model, the vertical 80/20 sliders had to slide up and down its connection to the bridge. Set screws were placed through the end caps and the PVC pipe in order to ensure that the pipe would not rotate during a run. Also, with the width of the apparatus, the end caps served as bumpers that kept the model in the center of the tank. Pictures of the experimental apparatus in the tank is provided in Figure 2.6.

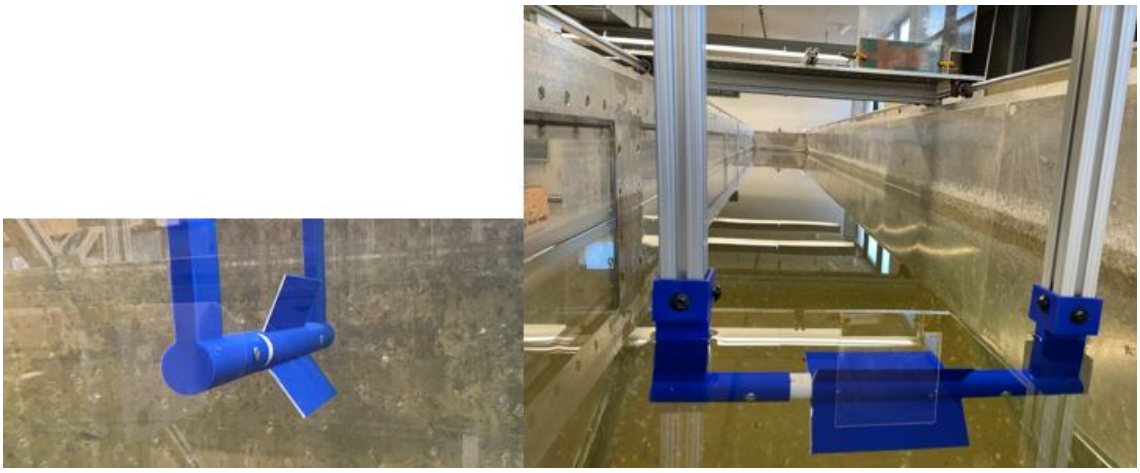

Figure 2.6. Experimental Apparatus in Tank

Using this experimental apparatus, the model was stable at all wave conditions. There was minimal shaking, and the only time where rotation was impeded was when there was debris in-between the model and the PVC pipe. In that event, the apparatus was taken out of the tank and the PVC pipe was cleaned.

To test the variability of the wave maker and to achieve a more accurate measurement of the wave amplitudes, the model was removed from the tank, and four ultrasonic sensors were placed above the tank. The ultrasonic sensors detected displacement of the water. The sensors were installed at the same approximate location of the models, and each probe was 20.32 cm apart. Figure 2.7 shows the testing set-up.

Figure 2.7. Wave Maker Variability Test Setup

Using the input values in Table 2.2, the wave maker was run for 60 seconds. The data collection was started slightly after the beginning of the waves in order to only collect the steady state values for the wave height. The data was then fit to a sine curve in order to approximate the average wave height for each run.

CHAPTER 3:
Data Collection and Processing

3.1 Data Collection

Videos of each run were taken on a GoPro Hero 4 digital camera at 30 frames per second. The GoPro was mounted on the side of the tank, giving a side view of the model. A small black sticker was placed on one of the blades, and the image processing toolbox in MATLAB was used to track this circle in the frame as a function of time. Figure 3.1 shows a frame collected in one of the runs.

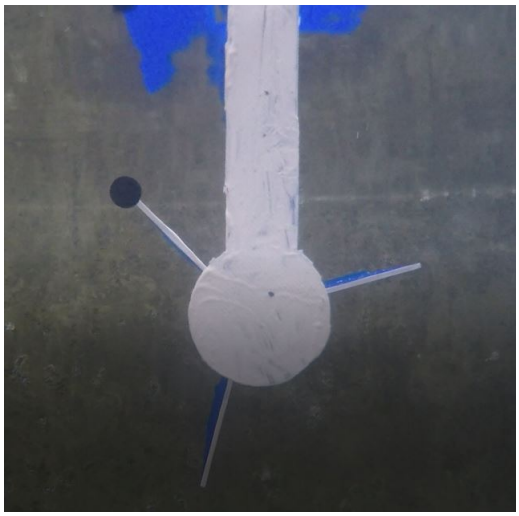

Figure 3.1. Experimental Model from GoPro Perspective. Frames Used for Data Analysis

There were several inherent difficulties with using image processing to collect data. First, the end caps caused a blind spot at the top of the blade's circular motion. The cross section of the vertical piece of the end cap was reduced in order to decrease the blind spot, but in order to have a fixed model, two end caps were needed. To analyze this data, the speed of the blade was interpolated as constant between the beginning and end of the blind spot.

Also, contrast was an issue. The side of the tank was made of aluminum, and this did not provide sufficient contrast with the black dot. Therefore, extra image filtering was necessary before analyzing the frame. Lighting also changed with each day, so the image filtering had to be adjusted depending on the conditions. Bright rays of sunshine also caused blind spots on some trials. After each run was finished, the video was trimmed so it contained at least one full rotation. An experimental log with visual comments about each trial is provided in Appendix A.

3.2 Image Processing

The MATLAB image processing toolbox was used to analyze each video run. As previously mentioned, the first objective was to filter the image in order to increase contrast on the black circle. To do this, the frame was converted to grey-scale and the *imadjust* function was used. An example of the *imadjust* function is provided.

$$J = imadjust(I, [LOWIN; HIGHIN], [LOWOUT; HIGHOUT]) \tag{3.1}$$

Essentially, this function takes the values in image I from the "in" ranges to the "out" ranges. The values below "low in" and above "high in" are clipped, so that feature is important in increasing the contrast or removing the dark back drop. Also, if "high out" is greater than "low out", then the image would be inverted. Figure 3.2 displays the outputs of this function.

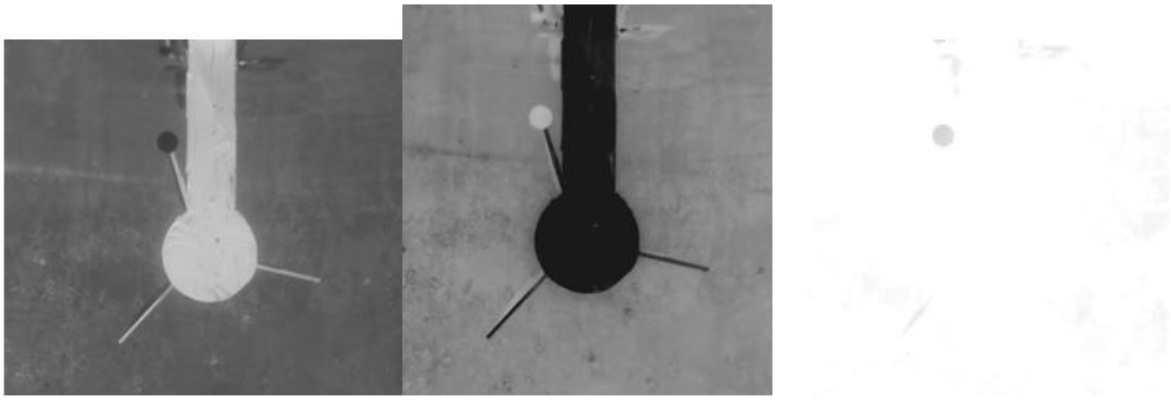

Figure 3.2. Image Filtering Outputs. Left: Grey-scale image, Middle: Imadjust and Inverting Photo, Right: Imadjust only

On the right, the black dot is the only discernible image in the frame. While the black dot became fainter, the image processing toolbox was still capable of tracking the circle with high accuracy. In some light conditions, the dot would be too faint. Therefore, the *imadjust* parameters would have to be adjusted in order increase the visibility of the dot. Consequently, more of the background would show in the frame. If the background was outside the arc path of the black dot, then the *imerase* function was used to remove parts of the frame that were unnecessary. If it was too difficult to achieve the image on the right, then the frame was inverted. While there was less contrast in this image, the toolbox was able to track the circle with high accuracy. The downside of inverting the image was computational time. With more pixels that the toolbox had to analyze, it would significantly increase the time it took to process a video.

In the MATLAB image processing toolbox, the *imfindcircles* function was used to track the circle. An example of this function is provided.

$$[CENTERS, RADII] = imfindcircles(I, RADIUSRANGE, PARAMETERS) \quad (3.2)$$

where I is the frame to be analyzed. The function needs an approximate range to search for the black dot, and the multiple different parameters that were used in this analysis were object polarity, sensitivity, and edge threshold. Depending on if the frame was inverted or not, the polarity parameter told the function to search for a circle that was "bright" or "dark" compared to its surroundings. The sensitivity increased the likelihood that a circle or multiple circles were found in the frame, and the edge threshold determined how much contrast between the dot and the surroundings was needed to register a circle location. If the sensitivity was increased to its maximum value, there was a greater likelihood of false detection. In order to find the desired circle with a high order of accuracy, the edge threshold was set to an extremely low value of 0.0125, and the sensitivity was raised until multiple false circles were detected in the frame.

With this function, it returned the center of the circle in pixels with the radius of the detected circle. This function was used in every frame of a run, and it would return the position of the circle as a function of time. Figure 3.3 displays an example return after the video was fully processed in MATLAB.

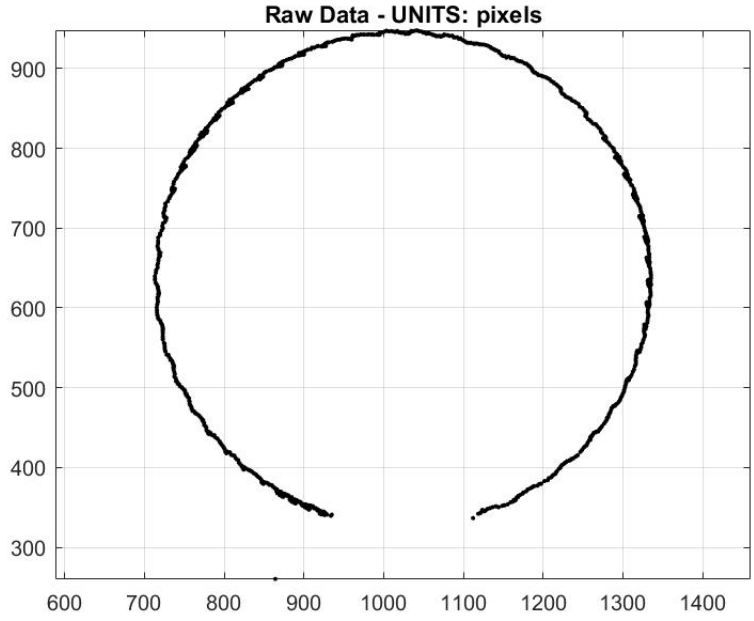

Figure 3.3. Image Processing Raw Data

3.3 Data Filtering

If a circle was not detected in the frame, then that time step was removed from the data. The bottom portion of the figure represents the blind spot area. Errors in the *imfindcircles* function would most likely occur directly before or after the blind spot. This is the point where the function would attempt to recognize a circle that was partially covered by the end cap. While this example run was fairly accurate, in order to remove any "bad" data points, an equation of a circle was best-fit to the data using a least-squares approach. Then, for each data point, the radius between the center of the best fit circle was found, as seen in Figure 3.4.

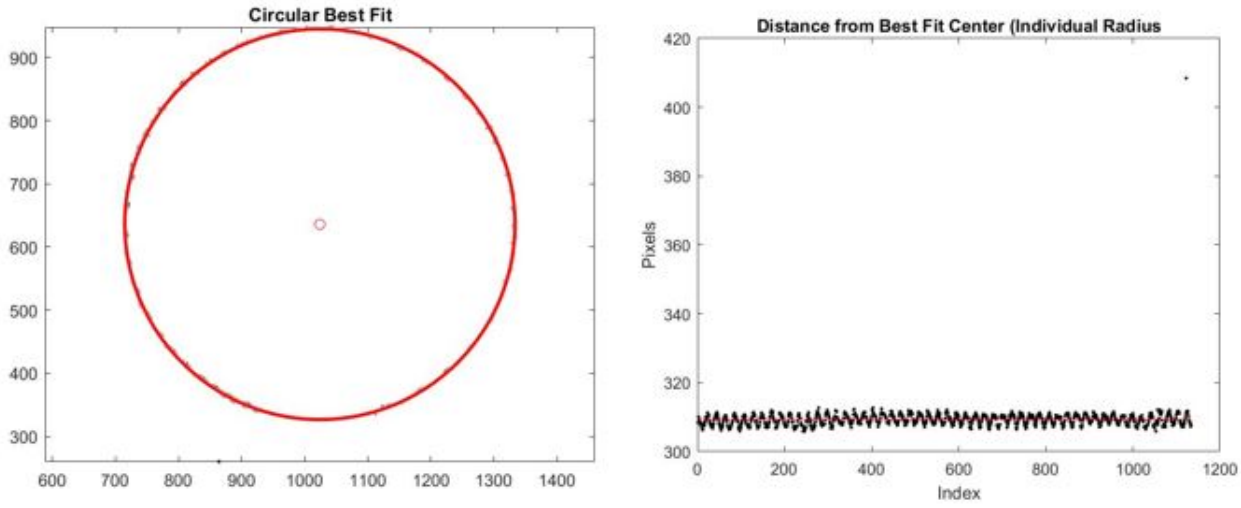

Figure 3.4. Image Processing Data Filtering

As seen in the figure, there was only one point at the end of the run where it found a circle way beyond the arc path of the blade. Any data point that was significantly off of the mean radius was removed from the data set. The variation in the radius was due to the small difference in diameter between the PVC and the model. While this "wobbling" most likely reduced the rotation of the model and would not occur in an actual WEC TENG system, it ensured that that friction was not a large factor in this experiment. The goal of the experimental set-up was to remove any outside factors and create a constant environment where the performance of each model could be objectively compared.

While this method solved the majority of the outliers, it would not remove points where the function found an incorrect circle on the arc path. To solve this, the data was manually viewed for any large discrepancies. The difference in position of the circle at each time step was relatively small, so the large discrepancies were easy to spot.

3.4 Post-Processing/Analysis

After the position data was properly filtered, the angular position over time was calculated. First, the positions were converted from pixel locations to polar coordinates

around the center of the circle. Then, the amount of rotation over time was determined from the first identified circle. Figure 3.5 shows an example of an angular position plot.

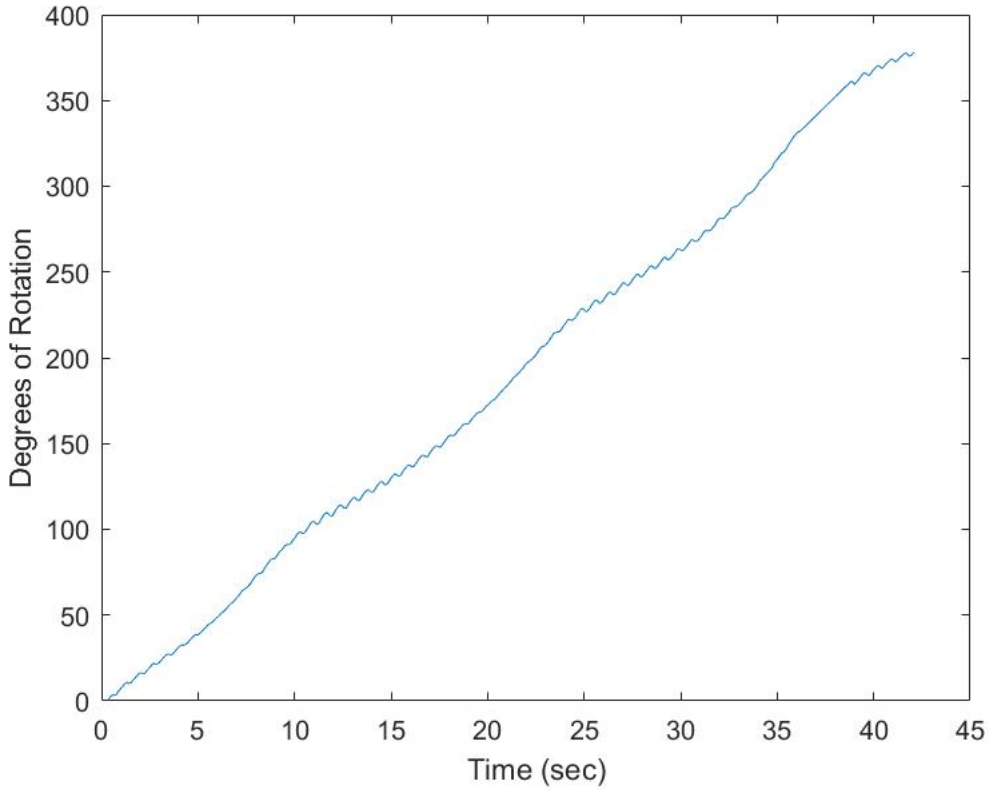

Figure 3.5. Model Degrees of Rotation Over Time Example

This figure provides a visual representation of the rotation over the entire trial that could be compared with different runs. This provides a qualitative analysis, but a quantitative metric was desired. The angular position data was differentiated to create a time based history of the angular speed. One limitation of this method was that the analysis of each run relied heavily on the accuracy of the image processing method. Even if the *imfindcircles* function was only slightly off on each circle, it would create unwanted noise in the data. This would have negative effects when calculating the angular rotation and angular speed of the model.

Figure 3.6 shows the angular speed as a function of time. In order to remove some of the unwanted noise due to the image processing code, frequencies greater than the wave frequency were filtered out of the data. This was because there could not be any frequencies in the data greater than the forcing frequency.

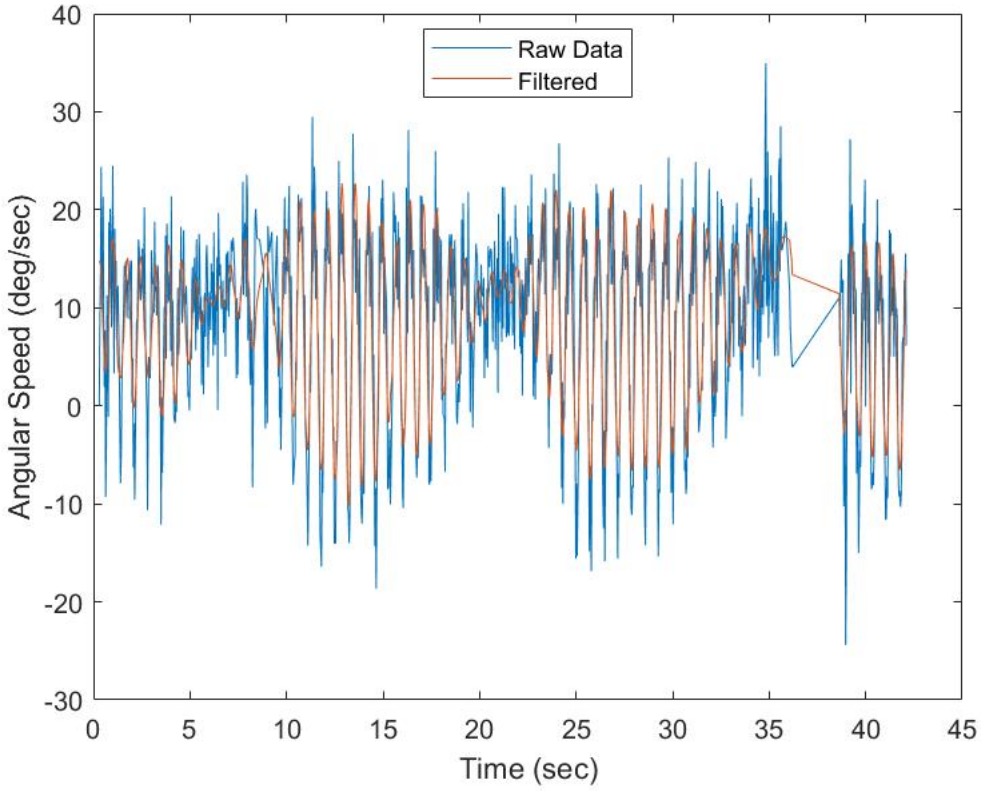

Figure 3.6. Angular Speed Over Time Example

From this data, the average angular speed was calculated by taking the integral of the absolute value of the angular speed over one full rotation of the model and divided by the full angle of one rotation (360 degrees). The direction of the rotation does not matter in a TENG, and the initial observation in some models were that there was some motion in both directions due to the oscillatory motion of the wave. This angular speed was also plotted as a function of blade position as seen in Figure 3.7.

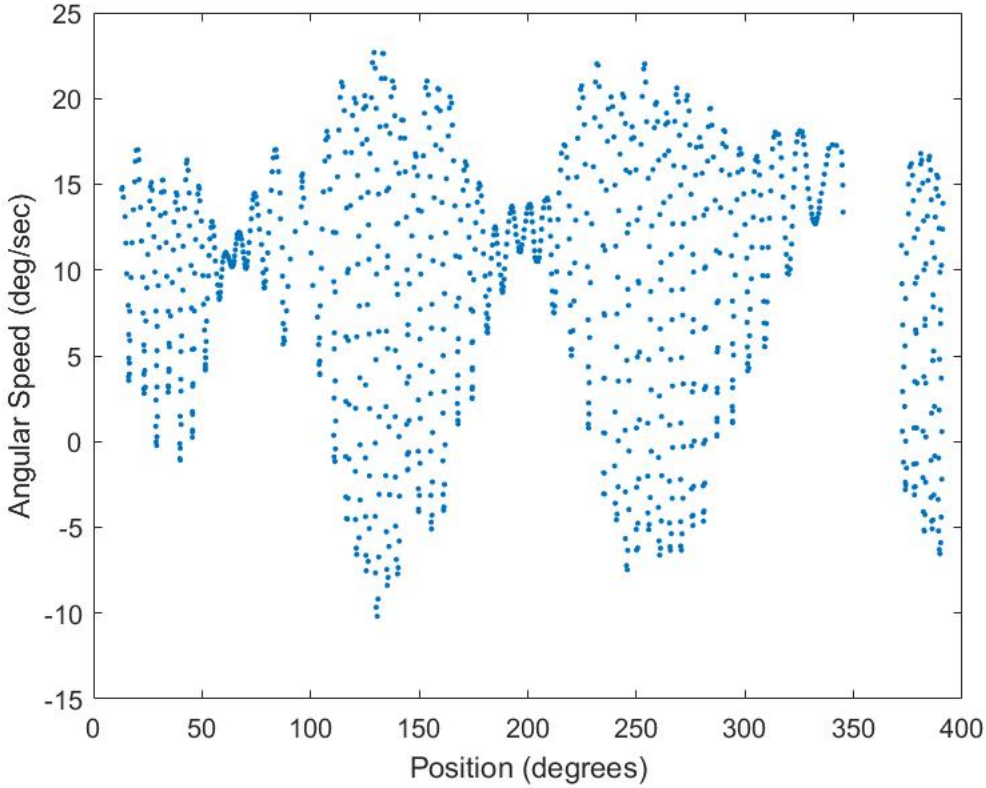

Figure 3.7. Angular Speed Over Position Example

The purpose of this plot was to identify the trends in angular speed and the orientation of the blades. Zero degrees was defined as when the marked blade was at the top of the arc path nearest to the free surface. The blind spot occurred at this position, and it can be seen in the figure between 340 degrees and 10 degrees.

In order for the average angular speed to be an accurate metric to compare models, several assumptions had to be true. First, the average angular speed was consistent over multiple full rotations and over different trials of the same condition. Second, the model would have to make a full rotation. And lastly, the variation between runs would have to be minimal. The image processing code takes a significant amount of time to run depending on the light conditions, so computational time was a limiting factor. The code could take

between 15 minutes to 2 hours for one single run. Using this data processing method, each run was analyzed and compared using both qualitative and quantitative metrics.

CHAPTER 4:
Results and Discussion

Experiments were conducted using the models outlined in chapter 2 to determine how each parameter affected the performance of the model. Ultimately, the maximum speed of a model was predicted and its behavior at different wave conditions was monitored to find the most optimal solution for a TENG design. The three blade model was considered the baseline design, and the majority of the testing was done with this concept. Therefore, each model in the analysis had three blades unless explicitly mentioned. As previously stated, Appendix A provides the conditions of each run that was conducted in this study.

In the testing data log, the rotation was categorized into the following behaviors:

- No Rotation
- Relatively Constant Speed, Full Rotations
- Interrupted (Non-Full Rotations) - Oscillating Steady State
- Interrupted (Non-Full Rotations) - No Oscillations
- Interrupted (Full Rotations)

The rotation type often varied between models and different wave conditions. "Interrupted" refers to any rotation where the speed was not approximately constant. Also, "oscillating steady state" is when there was some rotational speed occurring due to the waves, but the model was no longer making progress towards a full rotation. The purpose of categorizing each run was to determine if there was a pattern in the rotation behavior between the models. Specific comments about each run were also made in order to distinguish differences within the five categories. Notable observations from this analysis will be provided throughout this chapter.

While this chapter is organized into subsections of each studied parameter, it is important to note that many of these parameters are not independent from each other. In other words, a combination of different conditions could have caused a certain behavior or trend, and any theorized similarities were noted.

4.1 D_o Size

Figure 4.1 illustrates the impact of the model outer diameter with respect to the average angular speed. Each separate colored line represents the different incoming wavelengths tested. In this analysis, the proportions of the model were held constant at a (D/D_o) ratio of four, and each model was tested at a depth below the trough. For the models with a larger outer diameter, the blade size was also larger. Therefore, the centroid of the model was technically more submerged than the smaller models. However, the distance from the tip of the blade to the free surface was held constant.

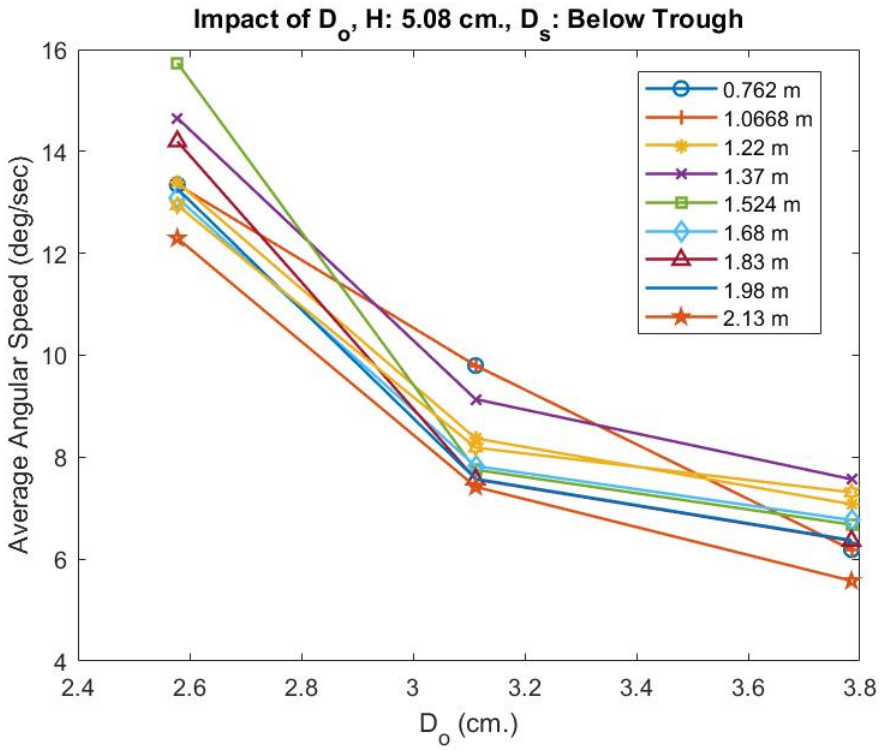

Figure 4.1. Impact of Model Outer Diameter

Based off of Figure 4.1, it is clear that an increase in model outer diameter caused a decrease in performance. A larger blade would receive more force from the wave, but would also increase the drag. In other words, the blade would have to push more water to rotate the model.

Since the total force from the wave at each specific wavelength trial remained constant in these tests, it was concluded that the benefit of receiving more of the wave force from a larger blade was less significant than the increased drag. Also, the orbital motion of the wave particles would have also remained constant due to the identical wave profiles, so a larger model would take more force to generate the same amount of rotation.

In terms of rotation behavior, Figure 4.2 compares the three different diameters tested at three different wavelengths.

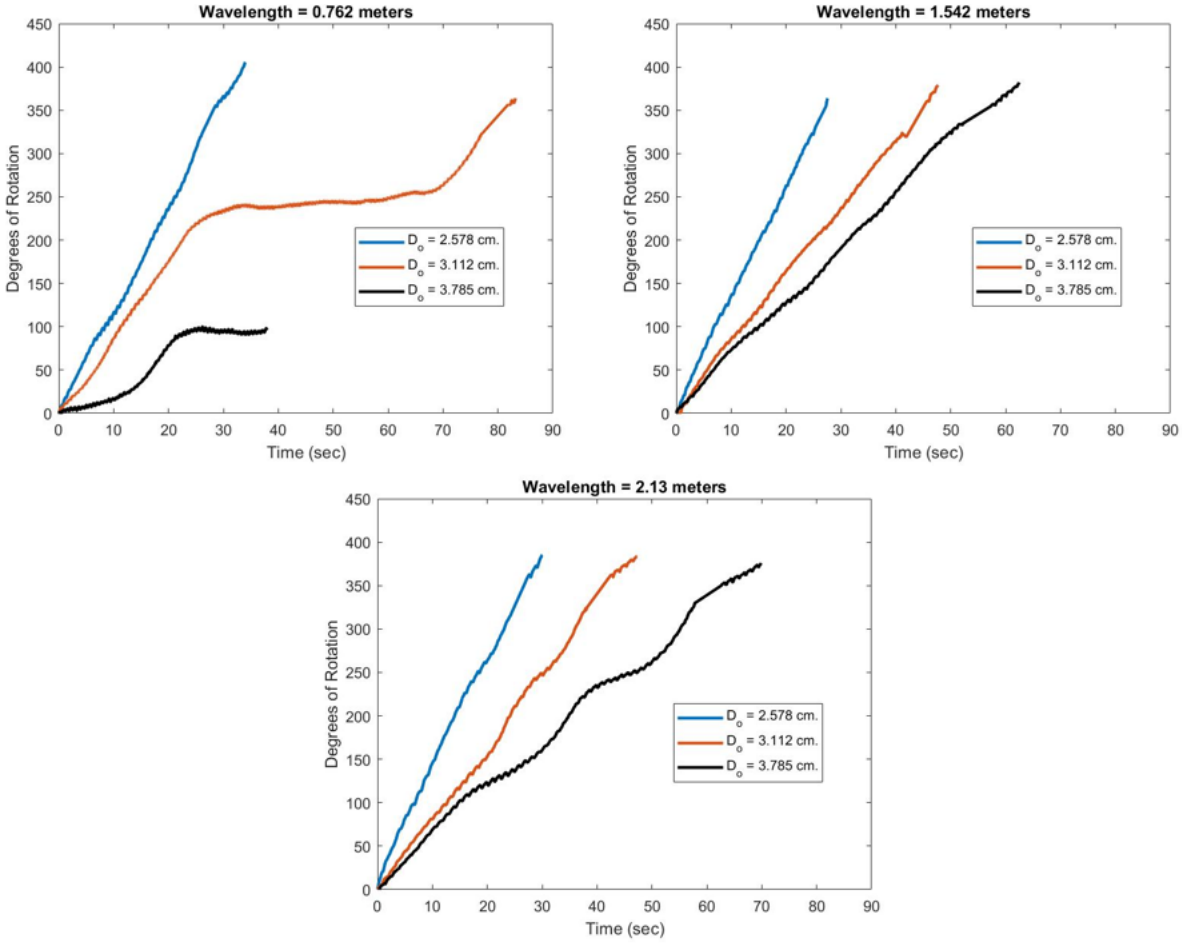

Figure 4.2. Rotational Behavior With D_o

At a wavelength of 1.524 meters, the motion was relatively constant for all three models. However, in the two extreme wavelengths, there appeared to be blade orientations around the rotational path where the speed was slower. As seen in the plot with the wavelength of 2.13 meters, there was repeating slower and faster sections. The slower sections occurred where a blade was close to the free surface. With three blades, one blade could have been receiving a force that contributed to the rotation of the model while the other two could have received a force that acted against the other blade. This hypothesis was analyzed later in the chapter. However, in regards to the general size of the model, with a longer or shorter wavelength, the rotational speed was not constant over one rotation.

With a wavelength of 0.762 meters, the largest model was not able to rotate past one of the slower sections and stopped rotating. However, the medium sized model remained in the slower sections for a long period of time and incrementally rotated to move into the faster section unlike the largest model. With a short wavelength and thus a quicker wave period, the blade did not have enough time with a contributing wave force to make any significant amounts of rotation while fully submerged. In other words, the wave would be acting against the model and it would lose its momentum. With the increase of the outer diameter and the size of the model, this only emphasized this effect. Conversely, the 2.13 meter wavelength trial would not have this same issue as the period of the wave was 1.71 times greater than the 0.762 meter trial. However, the increased drag and added mass from the larger blades and body caused it to rotate slower than the smaller models. In this case, a moderate wavelength would minimize the negative attributes of each extreme wavelength.

It is important to note that the average angular speed calculation does not find the rotation per wave cycle. Thus, if two runs at different wavelengths had the same average angular speed, the shorter wavelength trial would have been subjected to more wave encounters.

According to Figure 4.1, the average rotational speed of the smallest model was greatest at the 1.524 meter wavelength while approximately the same for the other two wavelengths. In the two larger models, the speed was approximately the same for the 1.524 meters and 2.13 meter wavelength tests. If the large slower section of the medium sized model was ignored, the speed was also approximately the same.

From these results, it was concluded that while the model was smaller, the benefit

of the higher energy and shorter wavelength waves was greater than the negative of the higher forcing oscillations. In other words, the smaller model was able to rotate a sufficient amount from the higher energy waves before the wave began hindering motion. This would allow the model to rotate past sections of slower angular speed. For the larger models, the model was not rotating nearly enough before the wave started acting against positive rotation. Therefore, the higher frequency forcing oscillations were more of a negative factor for larger models.

4.2 Wave Height

To determine the effect of wave height on the performance of a three bladed model, runs were analyzed using wave heights of 2.54 cm, 5.08 cm, and 7.62 cm. The wavemaker was only capable of making continuous 7.62 cm waves for wavelengths of 1.68 m, 1.83 m, and 1.98 m. The depth was held constant at below the trough, and multiple different D/D_o models were tested at these conditions. The results are shown in Figure 4.3

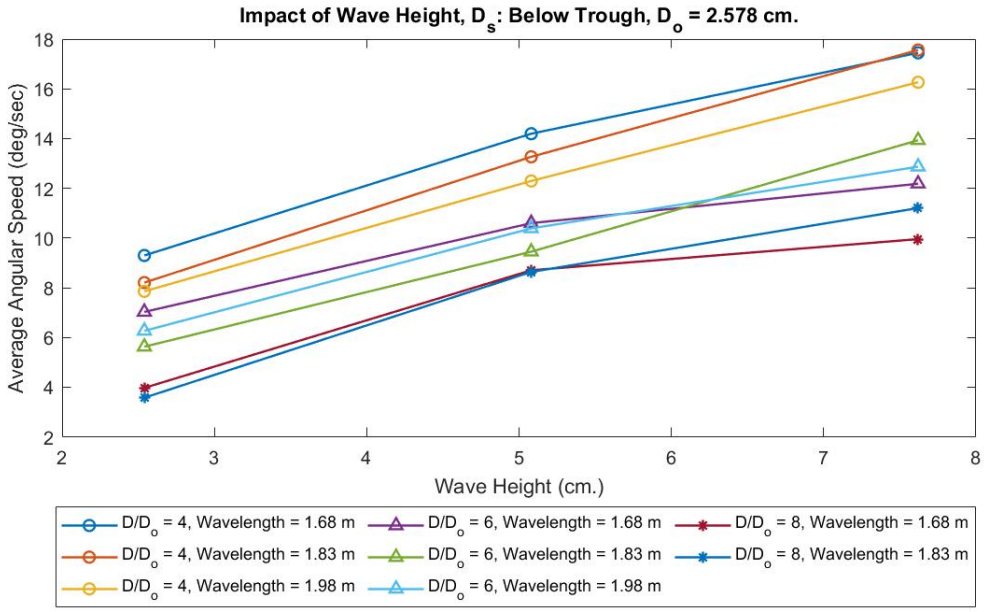

Figure 4.3. Impact of Wave Height

The figure clearly displays a positive relationship between wave height and average angular speed. Also, there was not a lot of difference in performance at different wavelengths within each different model size. A larger wave height at the same wavelength would have more energy than a smaller wave, which increased the force that the blades received from the wave particles. By holding all other parameters constant, the benefit can be easily seen.

The rotation behavior was consistent among different models, and example of the comparison is shown in Figure 4.4.

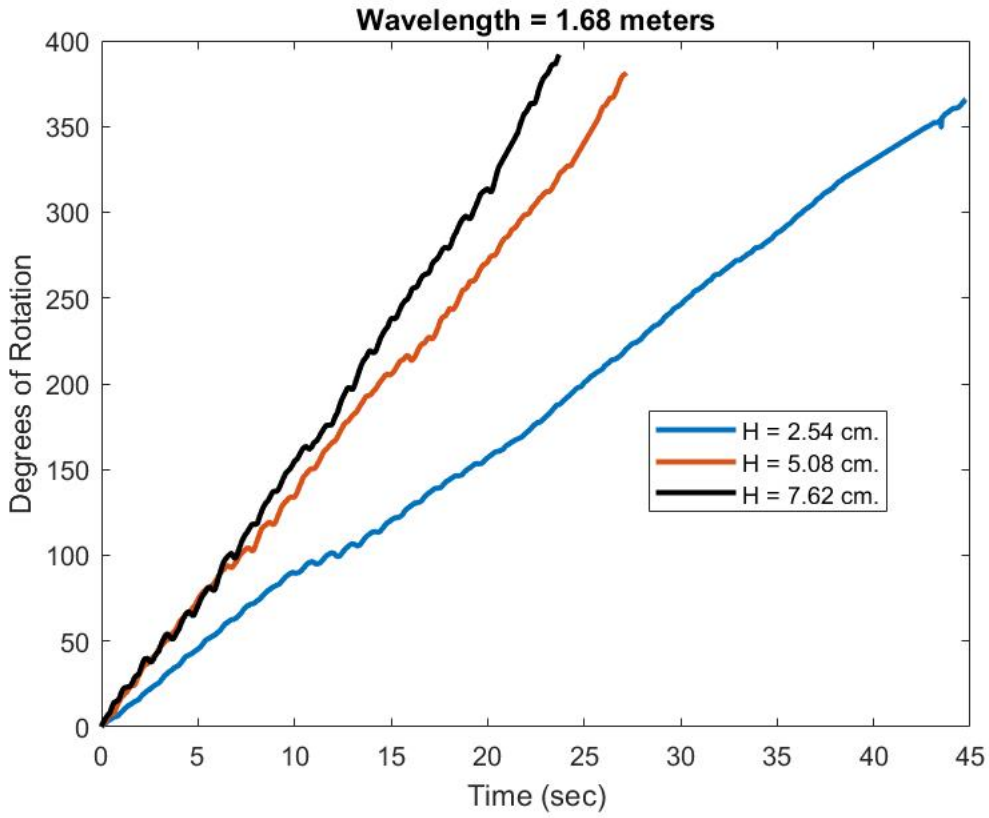

Figure 4.4. Impact of Wave Height on Rotation Behavior(D/Do = 4)

The angular speed remained relatively constant at each wave height, which can be seen with the constant slope. At the large wave heights, there was larger periodic back and forth motion in the model at each wave period. This is observed through the smoothness of

each curve. In other words, the larger the wave height, the less smooth the curve became. Also, the figure suggests that there is a limit to how much the wave height will benefit the performance of the model. Between 2.54 cm and 5.08 cm, the increase in speed was much greater than the increase between 5.08 cm and 7.62 cm.

While one blade may be benefiting from the increase in wave energy, the other blades could have increased forces that are resisting rotation. However, the benefit from the larger wave height is still apparent. If larger waves were tested, this trend would be expected to continue.

4.3 Wavelength

While the effect of wavelength was analyzed in conjunction with many other parameters, tests were conducted at the full bandwidth of wavelengths at each wave height for three different three bladed models. The purpose of these tests were to observe any trends in wavelengths with the models at differing blade lengths. Figure 4.5 displays the results at a wave height of 2.54 cm.

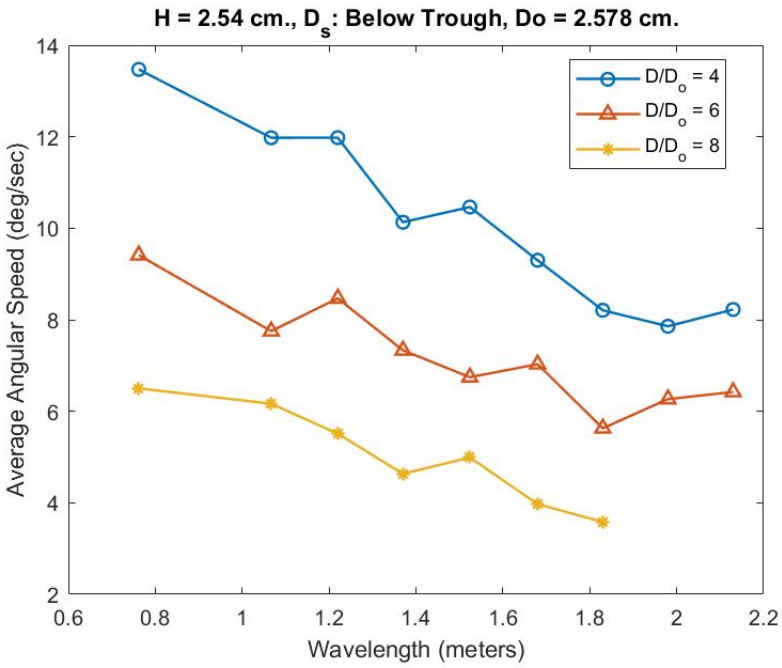

Figure 4.5. Wavelength Performance at Wave Height of 2.54 cm.

In all three models that were tested, there was a negative relationship between wavelength and average angular speed at a wave height of 2.54 cm. The smallest blade size also performed best, but that variable will be further tested later in the chapter. The rotational behavior during this trial is depicted in Figure 4.6.

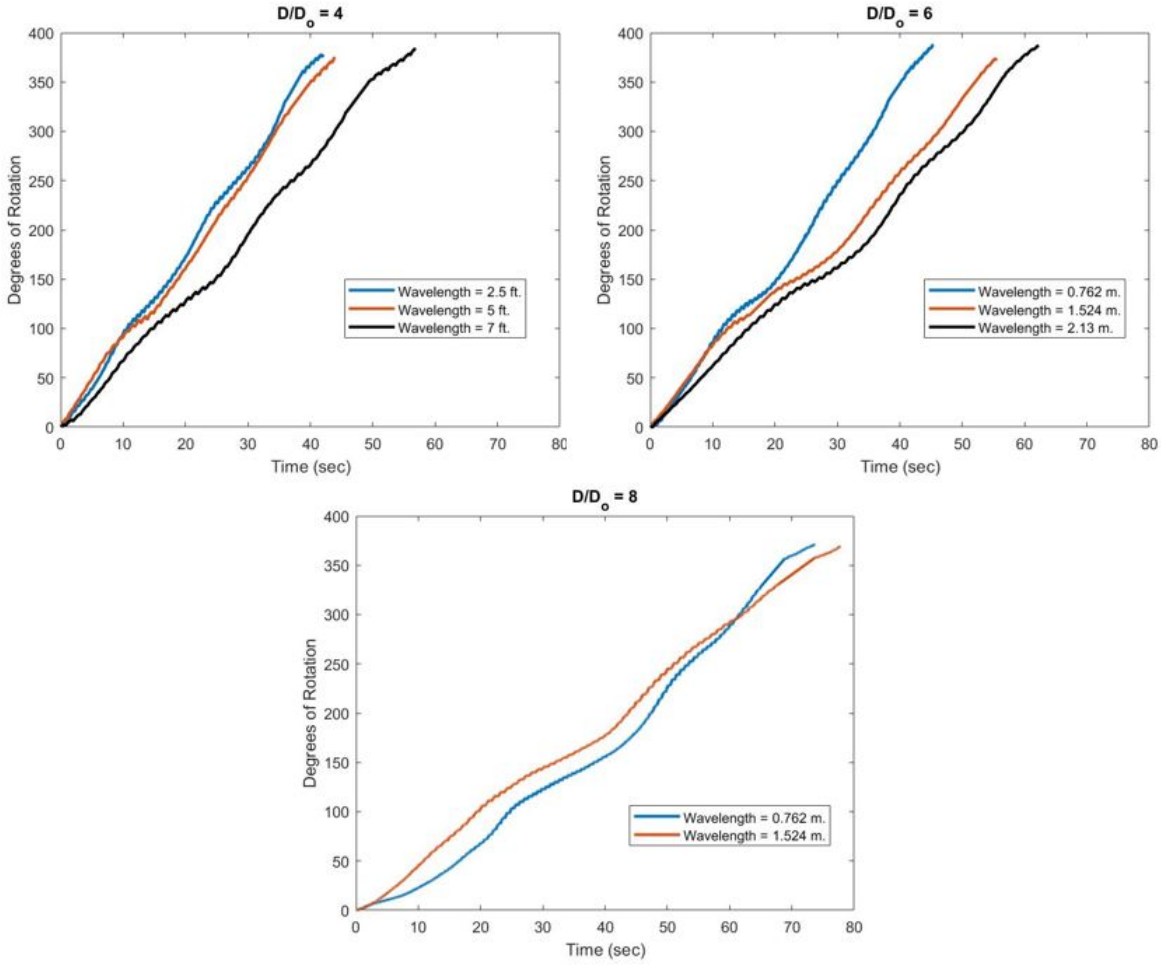

Figure 4.6. Wavelength Testing Rotational Behavior at Wave Height of 2.54 cm.

In the largest D/D$_o$ model, there was no rotation in the model for the 2.13 meter wavelength case, so its curve was omitted from the plot. The shorter wavelengths typically performed better than the longer wavelengths, except in the largest D/D$_o$ model where it was approximately the same. All runs exhibited some form of slower and faster sections, but as D/D$_o$ increased, the slower sections became more pronounced and significantly hindered rotation. This also occurred at shorter wavelengths for the two larger D/D$_o$ models compared to the smallest D/D$_o$ model. The same testing was done at a wave height of 5.08 cm as seen

in Figure 4.7.

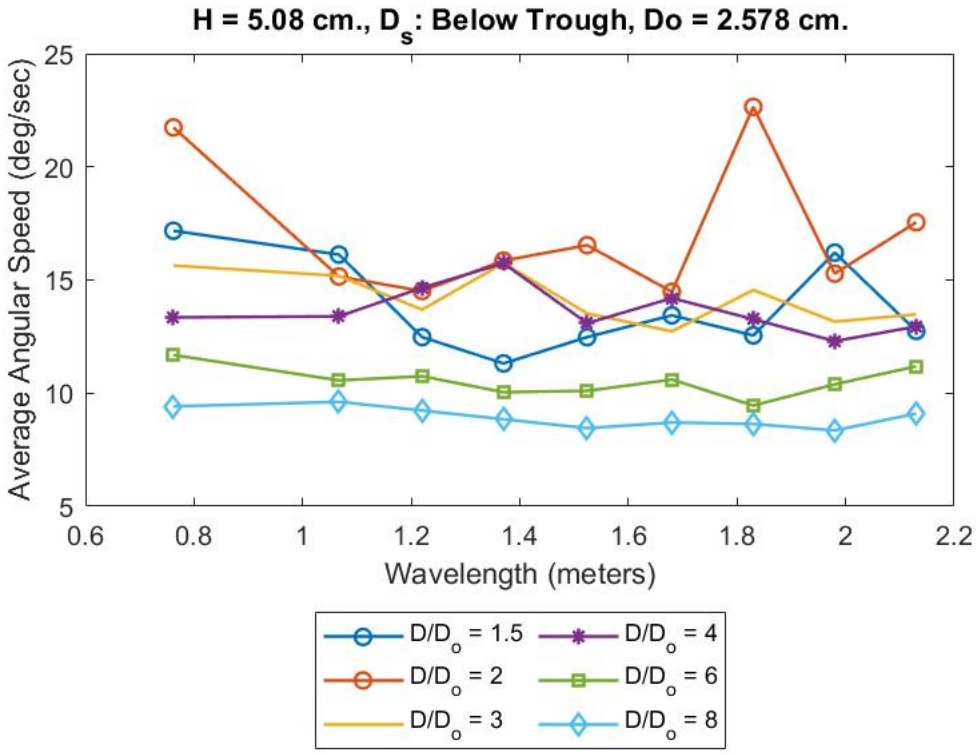

Figure 4.7. Wavelength Performance at Wave Height of 5.08 cm.

The performance of each model was mostly even across all wavelengths, with the exception of the three smallest blade size models. The D/D_o ratio of 2 was not tested at a wave height of 2.54 cm, so this data could not be compared against other wave heights. However, it is significant that the smaller blade sizes behaved in this fashion for a wave height of 5.08 cm. This suggested that more variability in performance occurs at smaller blade sizes. This behavior was further investigated in Figure 4.8.

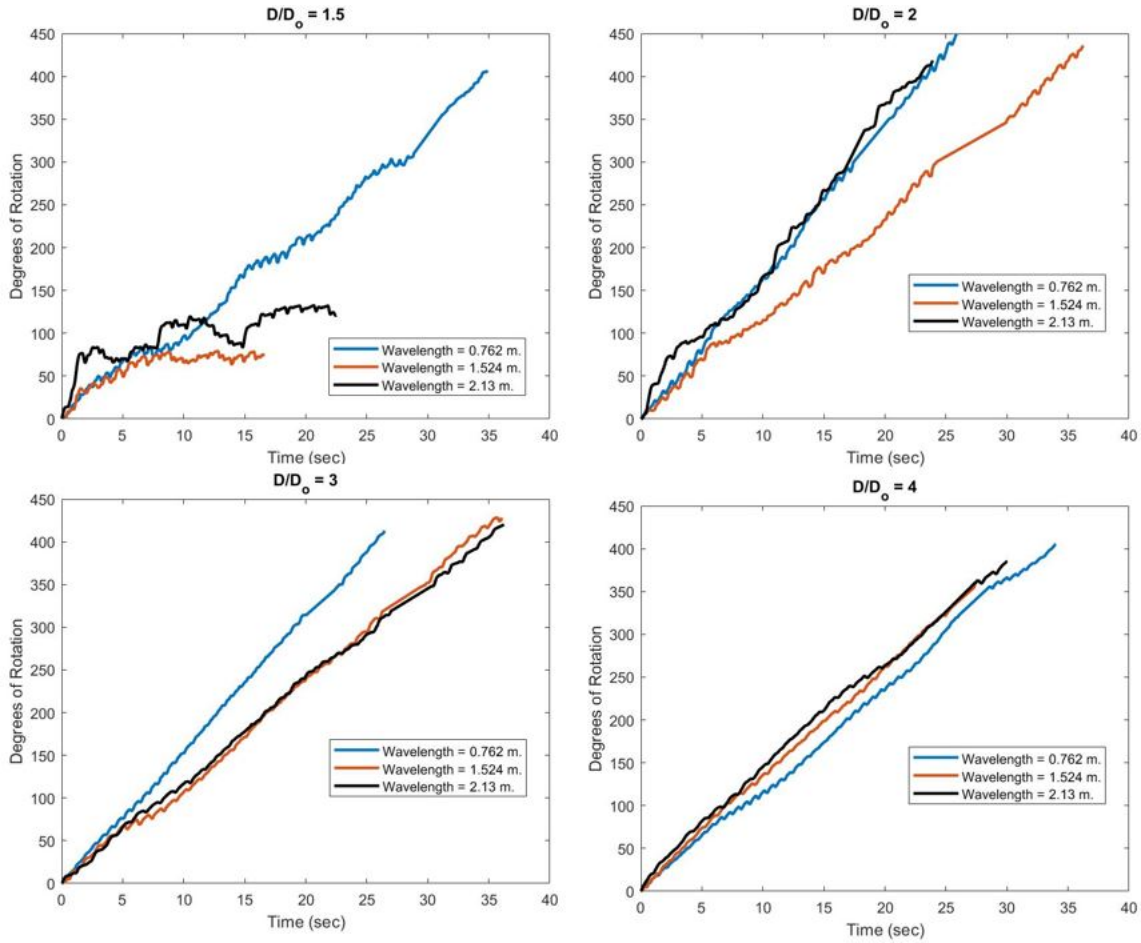

Figure 4.8. Wavelength Testing Rotational Behavior at Wave Height of 5.08 cm.

As seen in Figure 4.8, the intermediate wavelength in the smallest D/D_o ratio performed the best compared to the shortest and longest wavelength, where it did not complete a full rotation. Also, the smallest D/D$_o$ model had a less smooth rotational behavior. With a much smaller blade size, the drag caused by the blade is reduced. Although the force imposed on the blade is smaller, the reduced drag had a greater influence on the rotation of the model. In terms of wavelength, the reduced drag caused the model to be more subjected to the oscillating nature of the wave particles. This caused the rotational behavior to be more jagged.

The shortest wavelength performed the best in the D/D_o ratio of 3 model, and then the larger D/D_o models held constant performance. The models with a D/D_o larger than four maintained the same relationship as the model with a D/D_o of four. Lastly, the same testing was done at a wave height of 7.62 cm as seen in Figure 4.9.

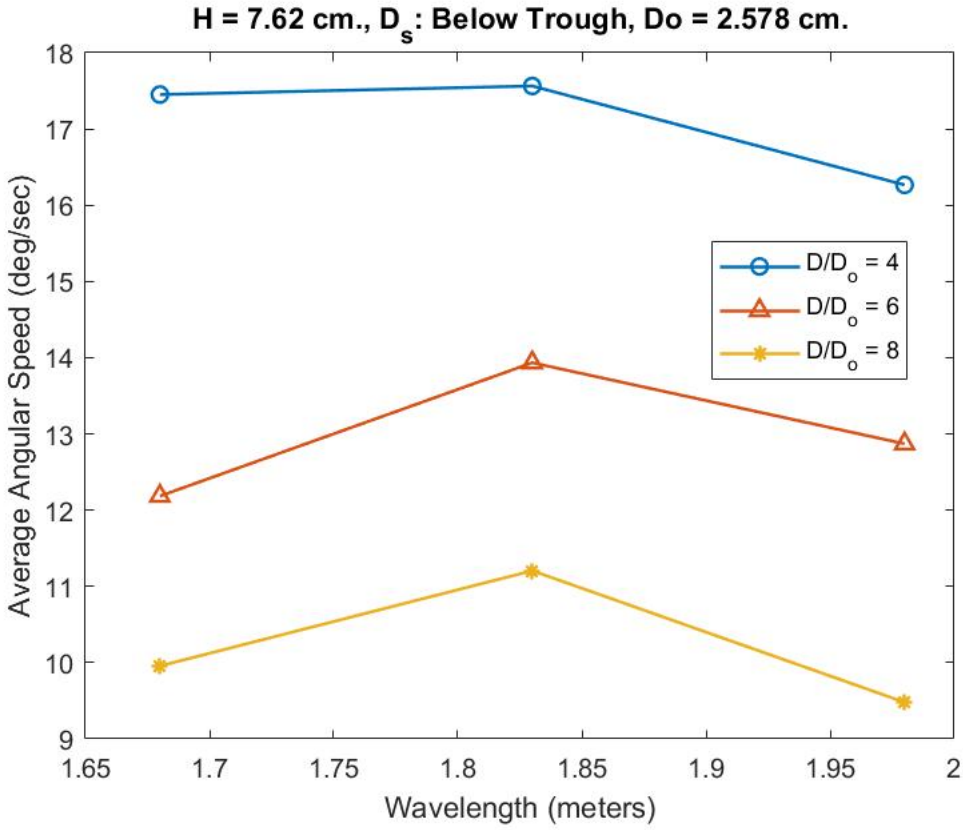

Figure 4.9. Wavelength Performance at Wave Height of 7.62 cm.

The performance of each model remained relatively constant at the tested wavelengths. However, any large variance would occur at the shortest wavelength, which was unable to be tested in the wave-maker. The rotational behavior remained consistent with the testing shown in Figure 3.4.

The wavelength tests were conducted at a submergence depth directly below the trough. While this held the distance from the top of the model to the free surface constant,

tests were also performed at a constant depth of 13.335 cm. The results are shown in Figure 4.10.

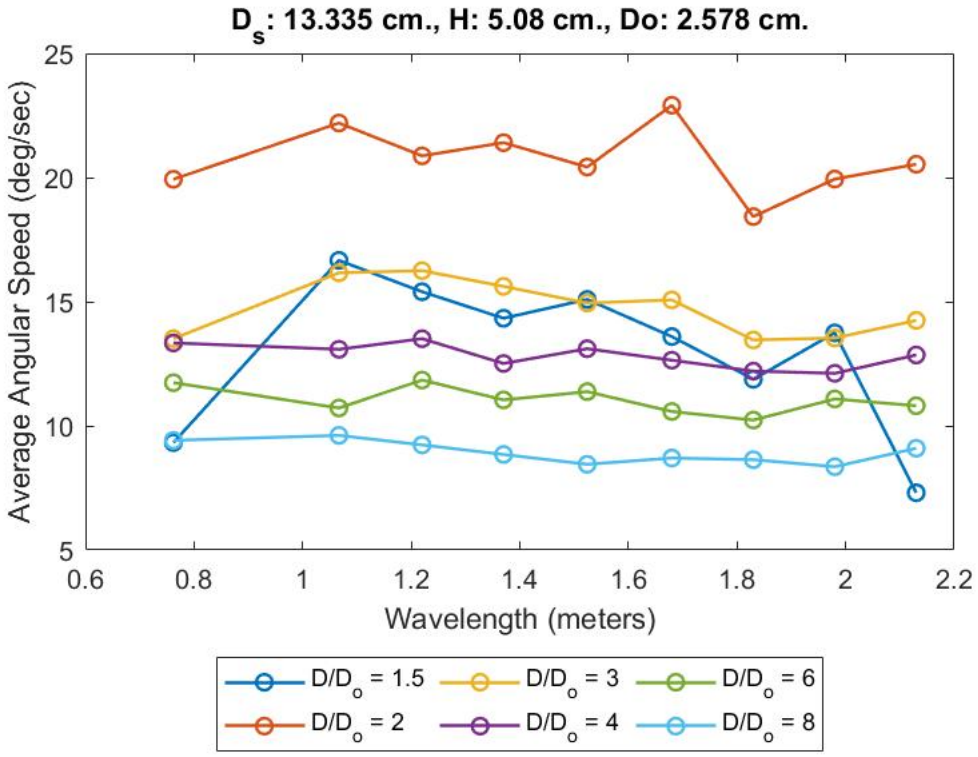

Figure 4.10. Wavelength Performance at Submerged Depth and Wave Height of 5.08 cm.

The relationship between the submerged depth and the blade size will be analyzed further, but it is clear to see that the smaller blade size resulted in greater average angular speed except for the smallest D/D_o ratio. This suggests that there is an optimal blade size, and that a smaller blade is not always the best solution for a three bladed model.

In terms of wavelength for each model, the performance was relatively constant except for the smallest D/D_o ratio model. There was reduced performance at the shortest and longest wavelengths. As the blade size was reduced at the submerged depth, the distance

from the tip of the blade and the free surface increased. As previously mentioned, the orbital motion of the wave particles decrease exponentially with depth. Therefore, the smaller blade received less force from the wave, which led to the decreased performance. This would be especially true for a shorter wavelength, which would not extend down as far for a shorter wave than it does for a longer wavelength. However, it also performed poorly for the longest wavelength, which would penetrate the furthest out of all runs. Figure 4.11 further investigated these claims.

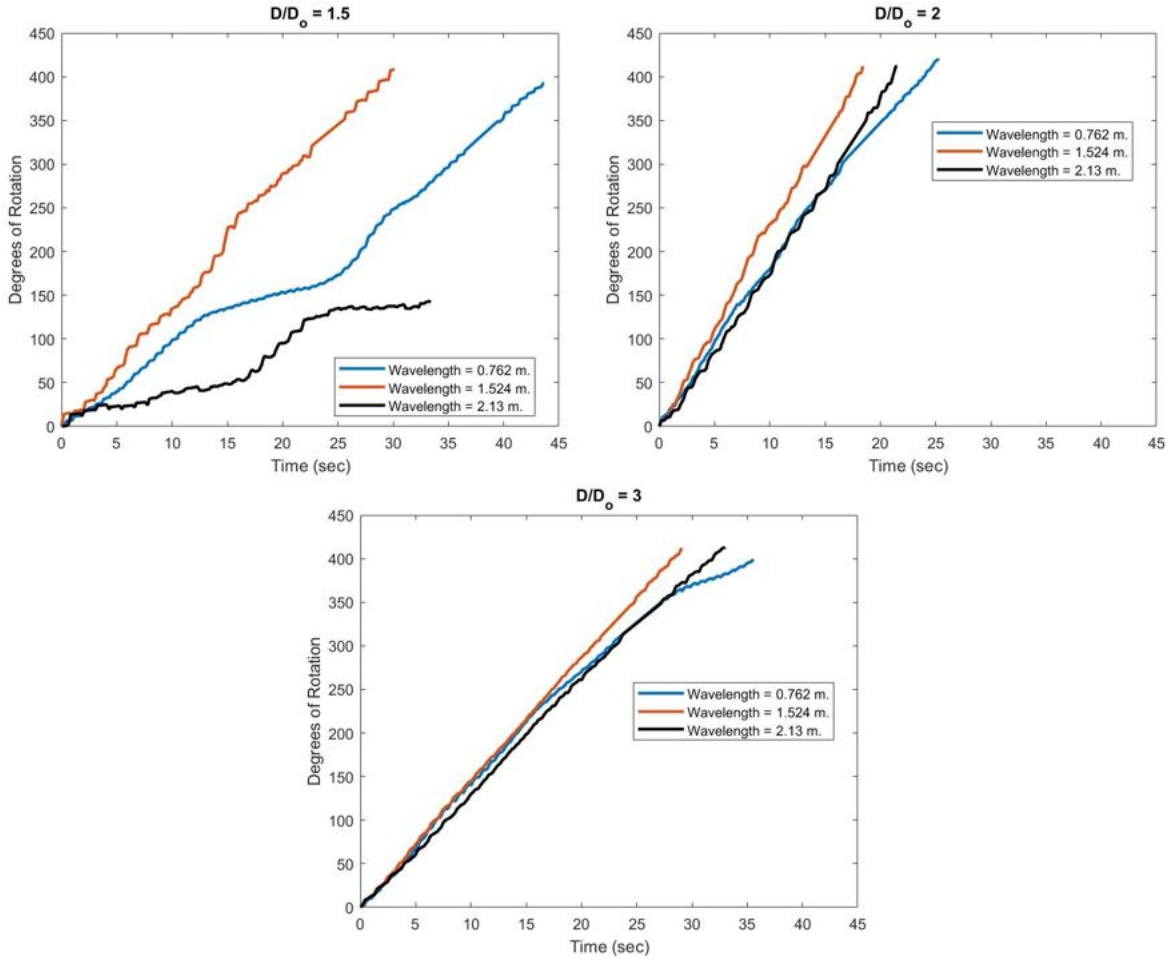

Figure 4.11. Wavelength Testing Rotational Behavior at Submerged Depth and Wave Height of 5.08 cm.

In the smallest D/D_o ratio model, the shortest and longest wavelengths had a decreased performance and the slower sections were more pronounced. In the longest wavelength, however, it was unable to make a full rotation. If the trial was extended, it may have made a full revolution, but the time required to make a full revolution would have been significantly longer.

While the previous statements about wave energy decay may be true, this effect could have been caused by the wave frequency and overall reduced orbital motion. The orbital motion would be reduced at all wavelengths, so the difference between the blade contributing to rotation and the blades restricting motion would also decrease. At the shorter wavelengths, more wave cycles would allow the model to rotate through the slower sections of the revolution faster.

For wavelengths, there was not an obvious trend. At times, it appeared that short and long wavelengths caused decreased performance. This parameter is most likely a secondary effect, and other parameters could have a more significant effect on the behaviors that were observed.

4.4 D/D_o Ratio

The effect of D/D_o ratio has already been mentioned in this analysis, but additional tests at six different blade sizes for the three bladed model was done in order to determine if there was an optimal size. Runs were conducted at a wave height of 5.08 cm and at both test depths. Figure 4.12 displays the results the depth directly below the trough.

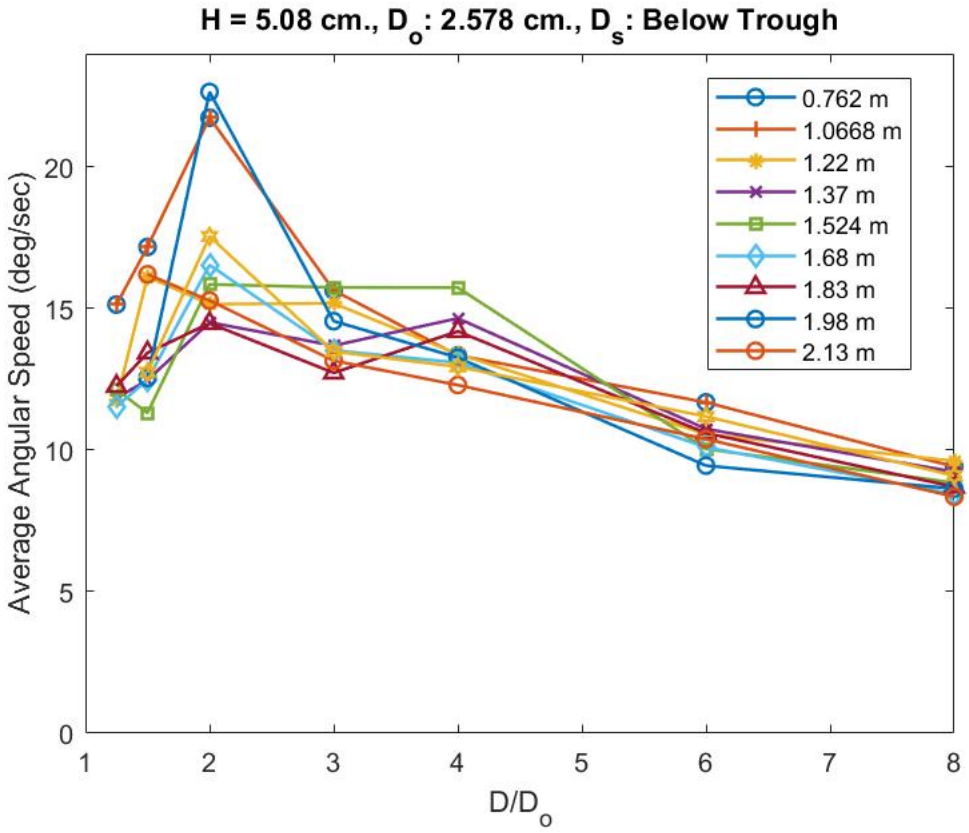

Figure 4.12. Impact of D/Do Ratio at Trough Depth

A D/D_o ratio between 2 and 3 was shown to have the most optimal average angular speed at this depth. A ratio of 1 would mean that no blades would exist on the model. A blade-less model was tested, and it yielded no significant rotation. The model would very slightly wobble due to the waves, but would not create any measurable rotation past the starting point. Therefore, it is assumed that the left side of the curve would approach zero at the ratio of one. Also, similar to prior observations, a larger blade size resulted in decreased performance. This optimum D/D_o ratio, however, suggested that a smaller blade size does not receive enough wave force in order to rotate efficiently. The rotational behavior as a function of D/D_o ratio is illustrated in Figure 4.13.

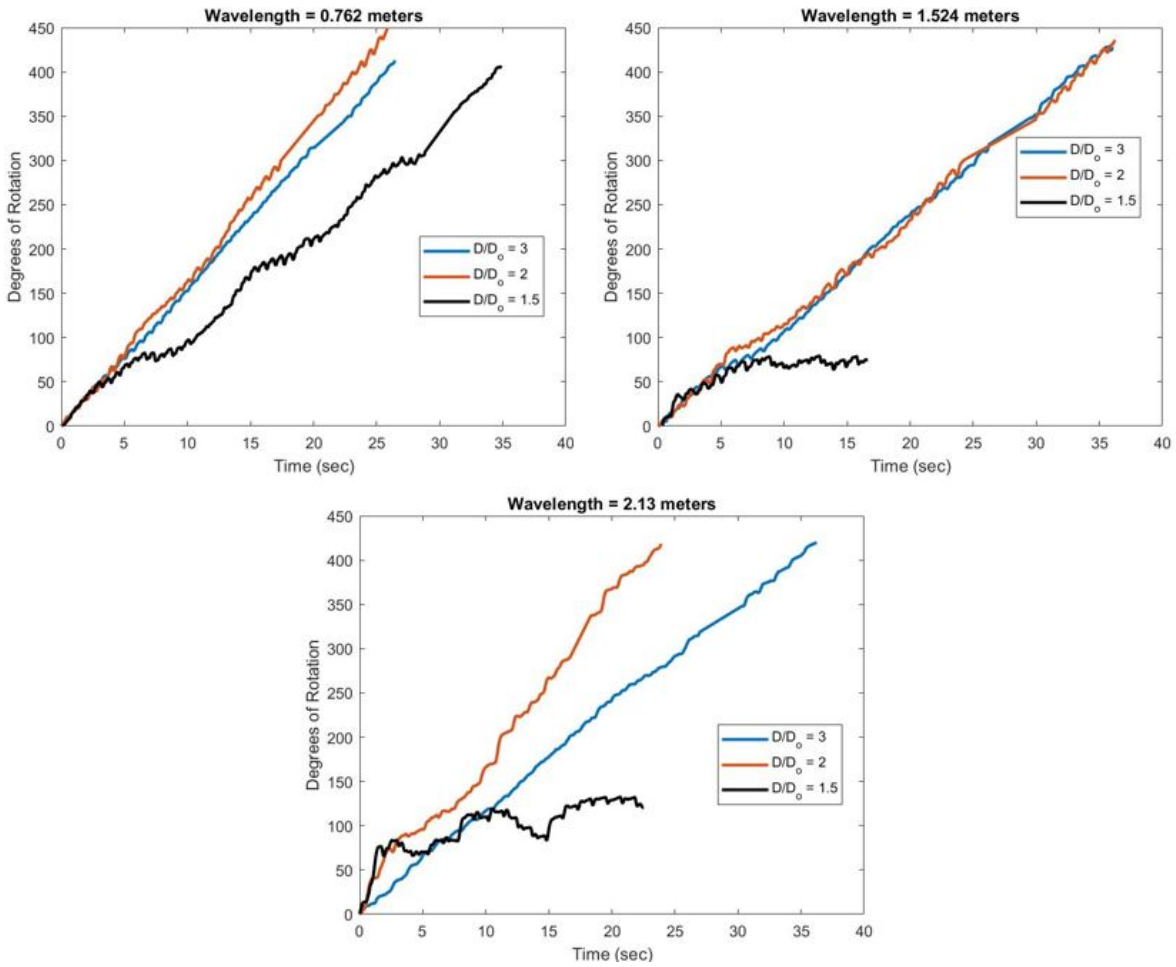

Figure 4.13. D/Do Testing Rotational Behavior at Trough Depth and Wave Height of 5.08 cm.

The blade sizes around the most optimum condition were analyzed. At the shortest wavelength, the shortest blade size was the only model that did not have relatively constant angular speed through the rotation. It was inconsistent and appeared to have faster and slower sections around the rotation path. The shortest model also did not complete a rotation in the other two longer wavelengths and stopped rotating at about the same position. As previously stated, it was predicted that the smaller blade area was not receiving enough force from the wave. While there is less drag from a smaller blade, if it could not rotate out of a position of

slower angular speed, then it would be stuck in that position. Also, at the longest wavelength, the model with a D/D$_o$ ratio of 2 had an inconsistent rotational speed compared to the model with a D/D$_o$ ratio of 3. This was also seen in the other wavelengths, but not to the extent of the seven foot wavelength trial. The same analysis was conducted at the submerged depth as seen in Figure 4.14.

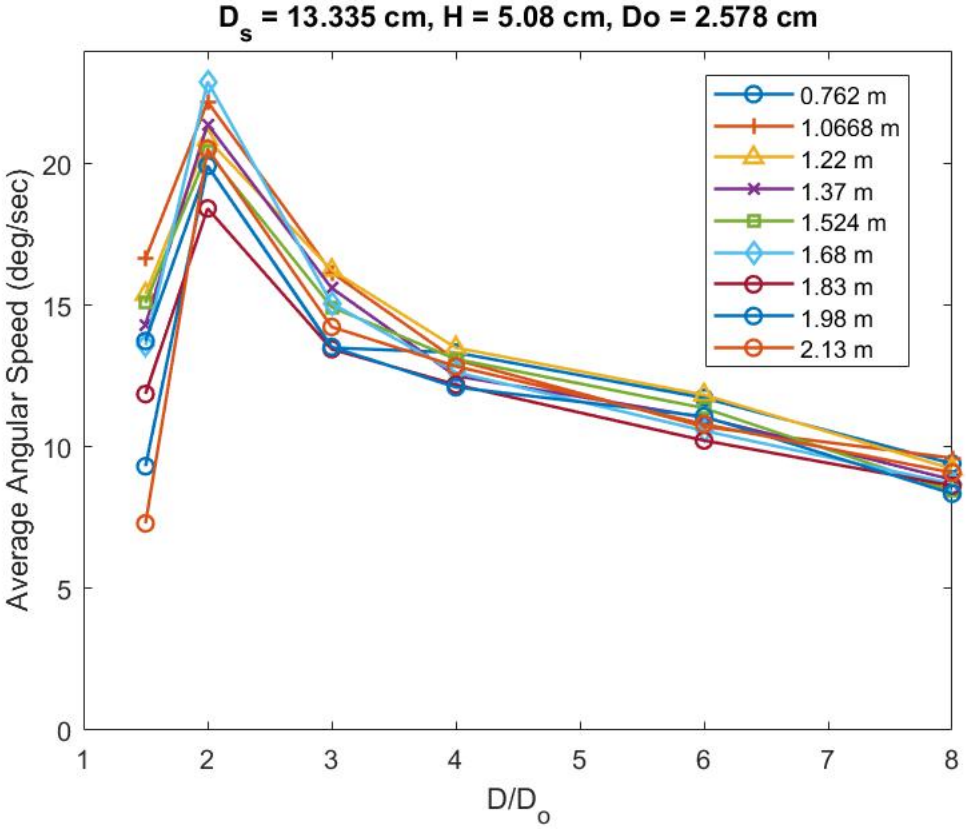

Figure 4.14. Impact of D/Do at Submergence Depth

The results at the submerged depth yielded the same conclusion that a D/D$_o$ ratio between 2 and 3 was optimal for the three bladed model. There was much less variability at each model in this test with the exception of the 1.5 ratio model. This was most likely due to the negative attributes of the model as previously described. The rotational behavior as a function of D/D$_o$ ratio at the submerged depth is illustrated in Figure 4.15.

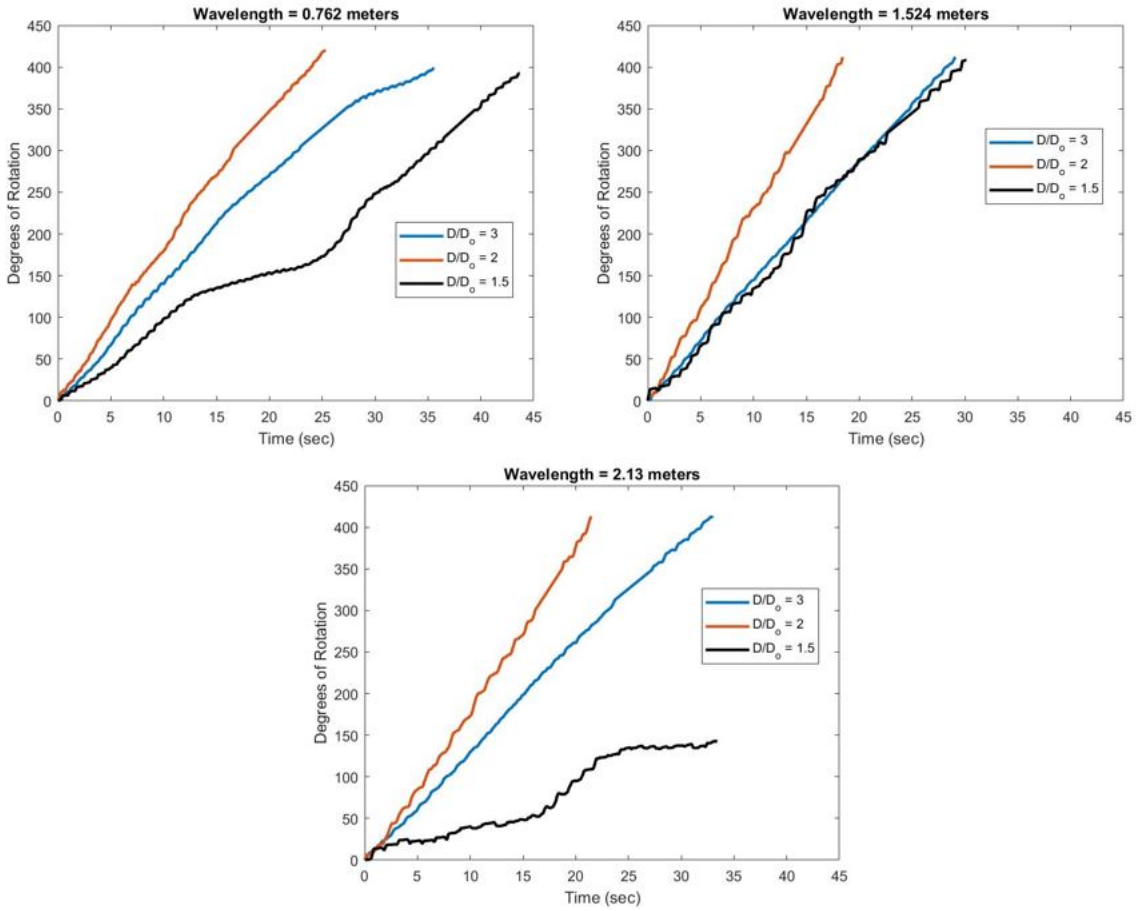

Figure 4.15. D/Do Testing Rotational Behavior at Submerged Depth and Wave Height of 5.08 cm.

At the submerged depth, the difference between the D/D$_o$ ratio of 2 and D/D$_o$ ratio of 3 models were more significant than at the trough depth. Also, the rotational behavior according to Figure 4.15 of the two models were much more consistent at this depth. The smallest ratio model was able to complete rotations at all of the wavelengths except for the 2.13 meter trial. In the 1.524 meter wavelength trial, it actually performed identical to the model with a D/D$_o$ ratio of 3. When submerged at a greater depth, the forcing from the wave decreases. It is predicted that the smaller wave force allowed the rotation to be less erratic while still providing enough force for rotation. At the 2.5 ft wavelength trial, the model with

a D/D_o ratio of 1.5 was stuck in the position of slower angular speed for longer than at the trough depth. This would suggest that the prediction could be true.

4.5 Submergence

In addition to the two different experimental depths that all models were tested at, one model was tested at incremental depths until the performance significantly decreased. Figure 4.16 displays the results.

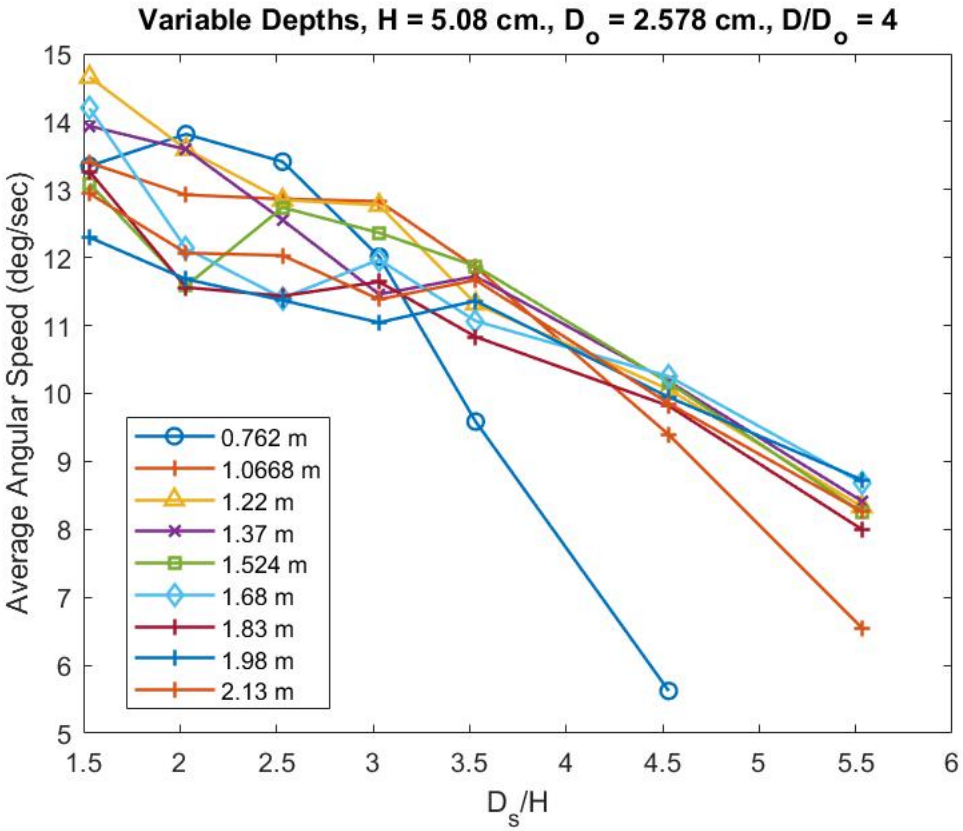

Figure 4.16. Impact of Model Depth

As previously mentioned, the energy from the wave decreases exponentially with depth, with its lower limit as one half of the wavelength. Therefore, the shorter wavelengths

should experience the most effect from increasing depth. This was proven to be true, as the shortest wavelength experienced decreased performance almost immediately and ultimately could not rotate at the deepest tested depth. Most of the wavelengths were not significantly affected by the depth, since the deepest test depth was 28.1 cm. If the experiment was extended, then the other wavelengths would follow in a similar trend to the 0.762 meter wavelength trials. Another illustration of the data is provided in Figure 4.17.

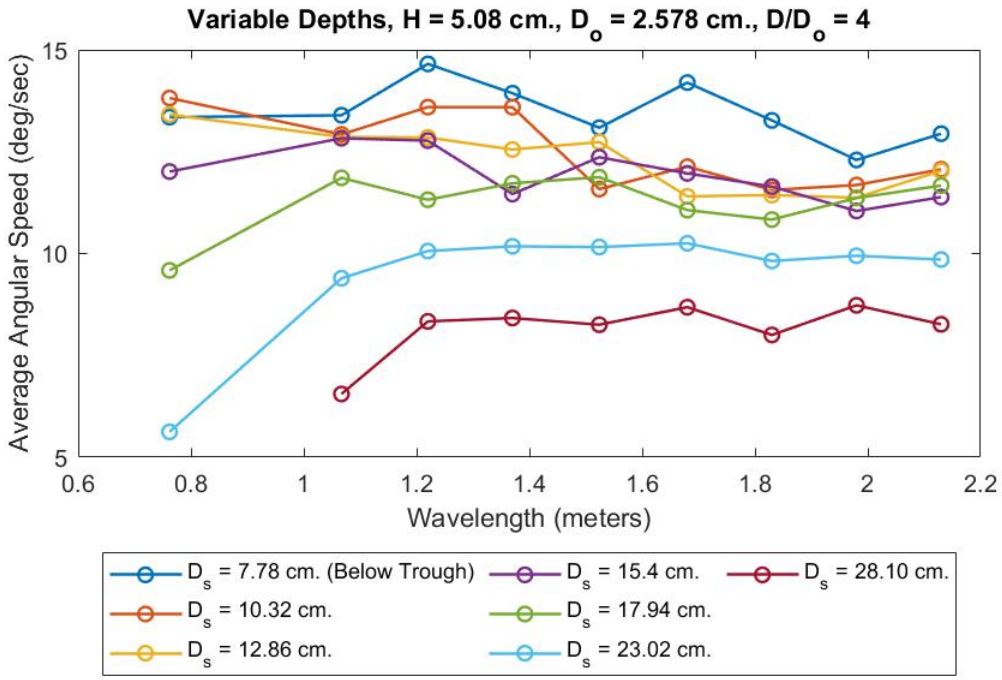

Figure 4.17. Impact of Depth as a Function of Wavelength

This plot clearly shows the decrease in performance at the smaller wavelengths. The performance is mostly unaffected except when the submergence depth surpasses 17.94 cm. To classify the change in behavior of the rotation as a function of depth, Figure 4.18 was analyzed.

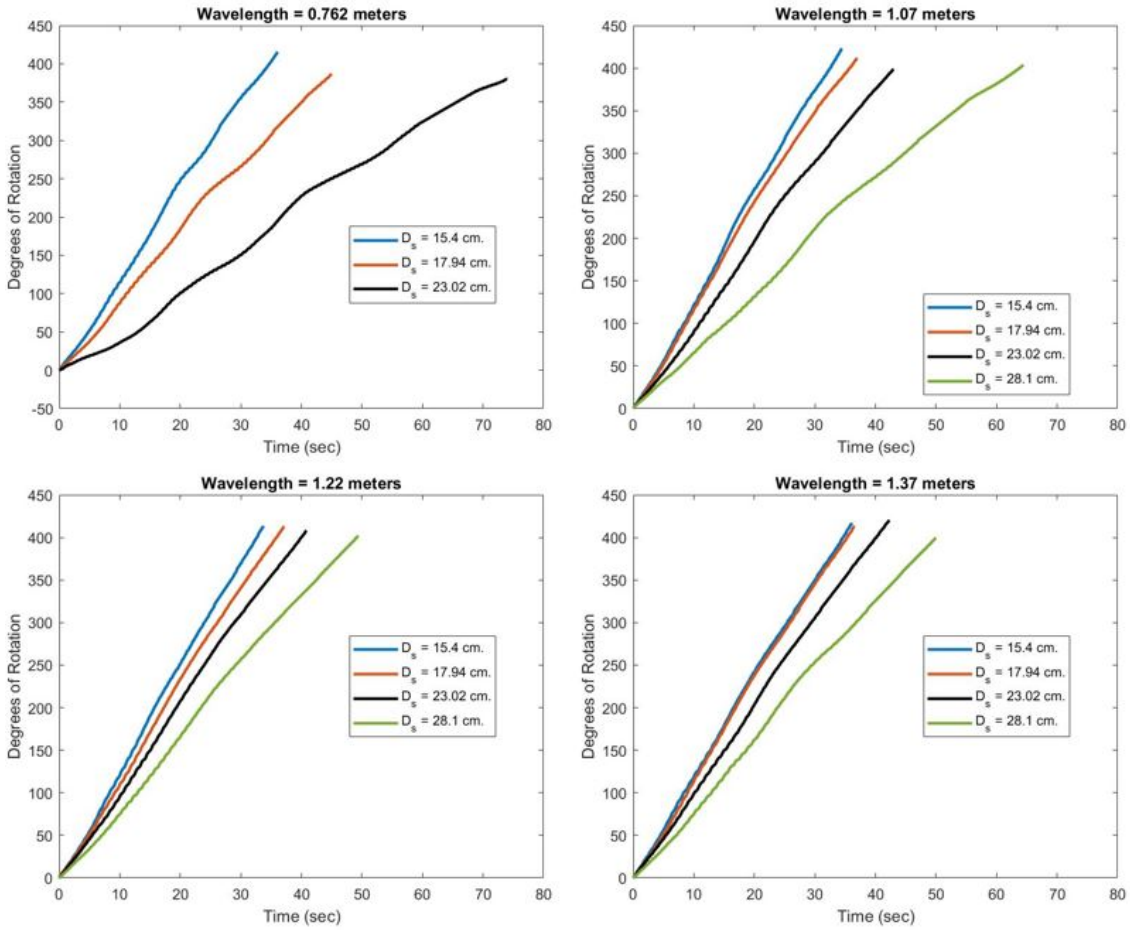

Figure 4.18. Depth Testing Rotational Behavior at Wave Height of 5.08 cm.

As the wavelength increased, the difference in performance between the different test depths decreased, and the rotational behavior became more consistent. At the shorter wavelengths, there was less force from the wave, so it would be more difficult for the model to rotate in the slower speed sections. However, since the longer wavelengths penetrate deeper in the water column, the effect was less pronounced. Depth decreases performance of the model as expected, especially at shorter wavelengths.

4.6 Number of Blades

For the majority of the experiments, three bladed models were used as the baseline to determine the effect of different parameters. In this portion, the number of blades, the size of the blades, and the orientation of the blades were tested in order to observe any noticeable changes in rotation or performance. Figure 4.19 illustrates the cross sections of the one and two blade models. The first experiment tested a one bladed model with the results shown in Figure 4.20.

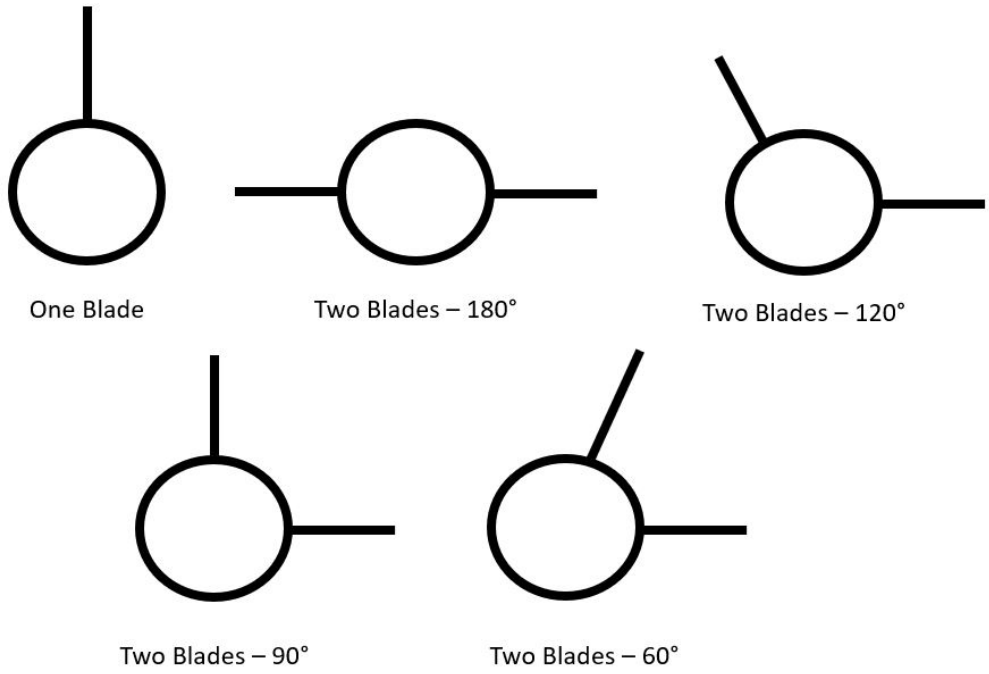

Figure 4.19. One and Two Blade Model Cross Sections

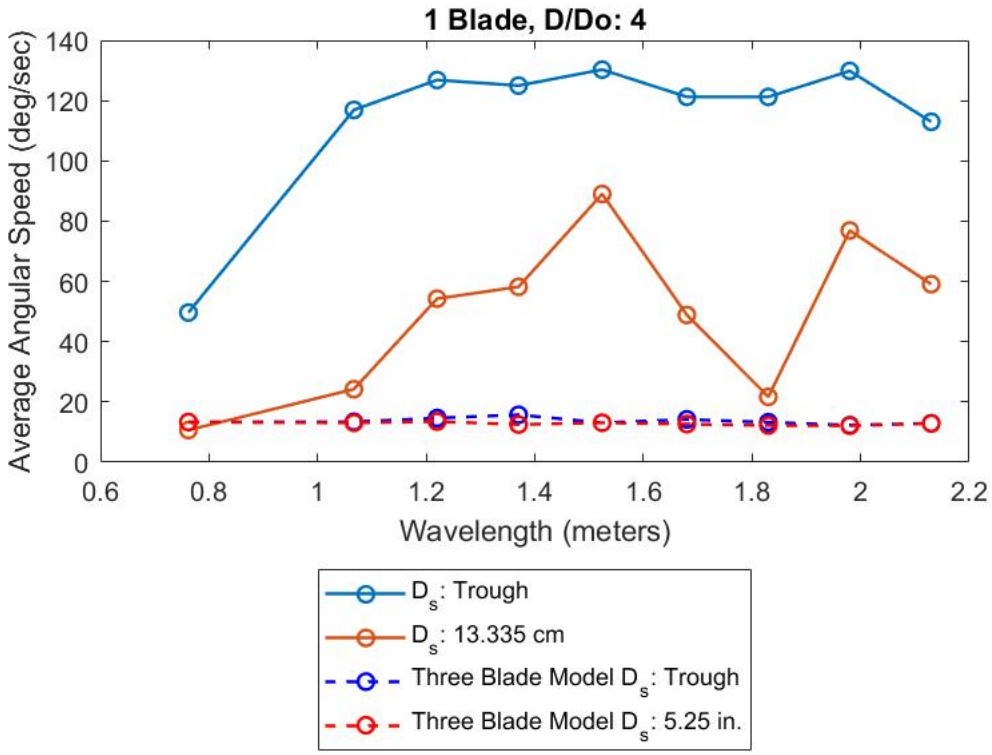

Figure 4.20. One Blade Model Performance

This plot clearly shows that the one blade model outperforms the three blade model at both depths. However, the average angular speed is misleading in this case. In both of the 0.762 meter wavelength trials, and all of the submerged depth trials, the model did not fully rotate. Instead, it would oscillate at a fairly steady value. For those trials, the steady state average angular speed was calculated and plotted on Figure 4.20. To analyze the rotational behavior of the model, Figure 4.21 is shown.

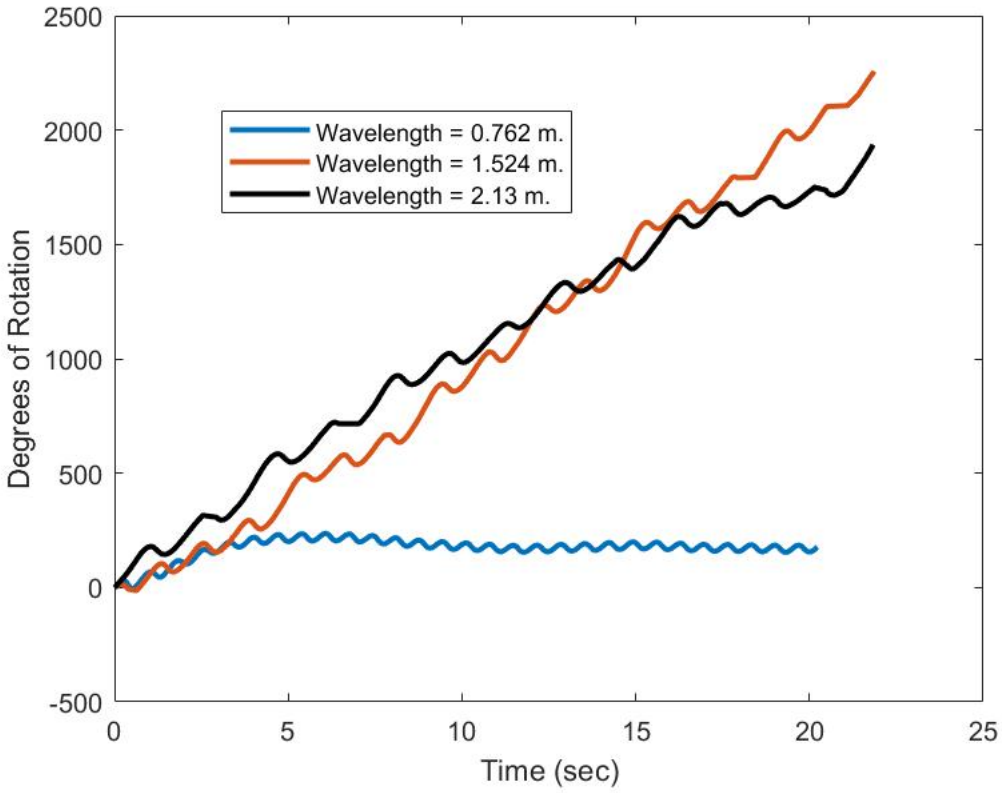

Figure 4.21. One Blade Rotational Behavior at Trough Depth

The steady state amplitude of the shortest wavelength trial was 18 degrees per second, which was slightly lower than the performance of the three blade model. In these models, it took multiple wave cycles to make one full motion. When the period of the wave was too small, it would not have time to sync with the frequency of the wave. In other words, it would not have time to be in the correct position to benefit from the wave at all times. This is clearly seen in the 0.762 meter wavelength trial.

Based off of these results, it is clear that added blades average angular speed. While the one blade design increased the average angular speed, two blade models were tested next as seen in Figures 4.22 and 4.24.

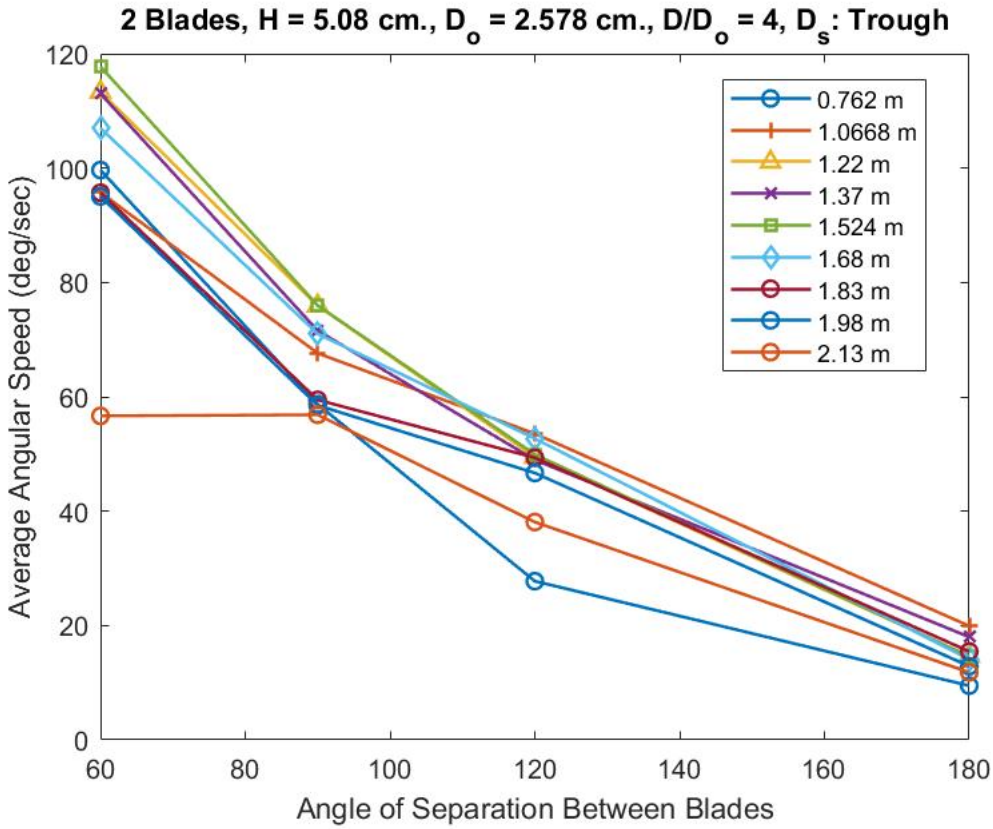

Figure 4.22. Two Blade Performance at Trough Depth

At the trough depth, the average angular speed of the two blade model with 60 degrees of separation was roughly equal to the one blade model. When the angle of separation increased, the speed decreased fairly drastically. In the smaller angle of separation models, both blades were most likely contributing to the positive rotation. Conversely, the blades in the larger angular of separation models were most likely acting against each other. However, when the blades were not 180 degrees apart, the model was no longer balanced around the center of its axis of rotation. Therefore, its natural resting position would be where the blades are pointing towards the bottom of the tank. The rotational behavior was investigated in Figure 4.23.

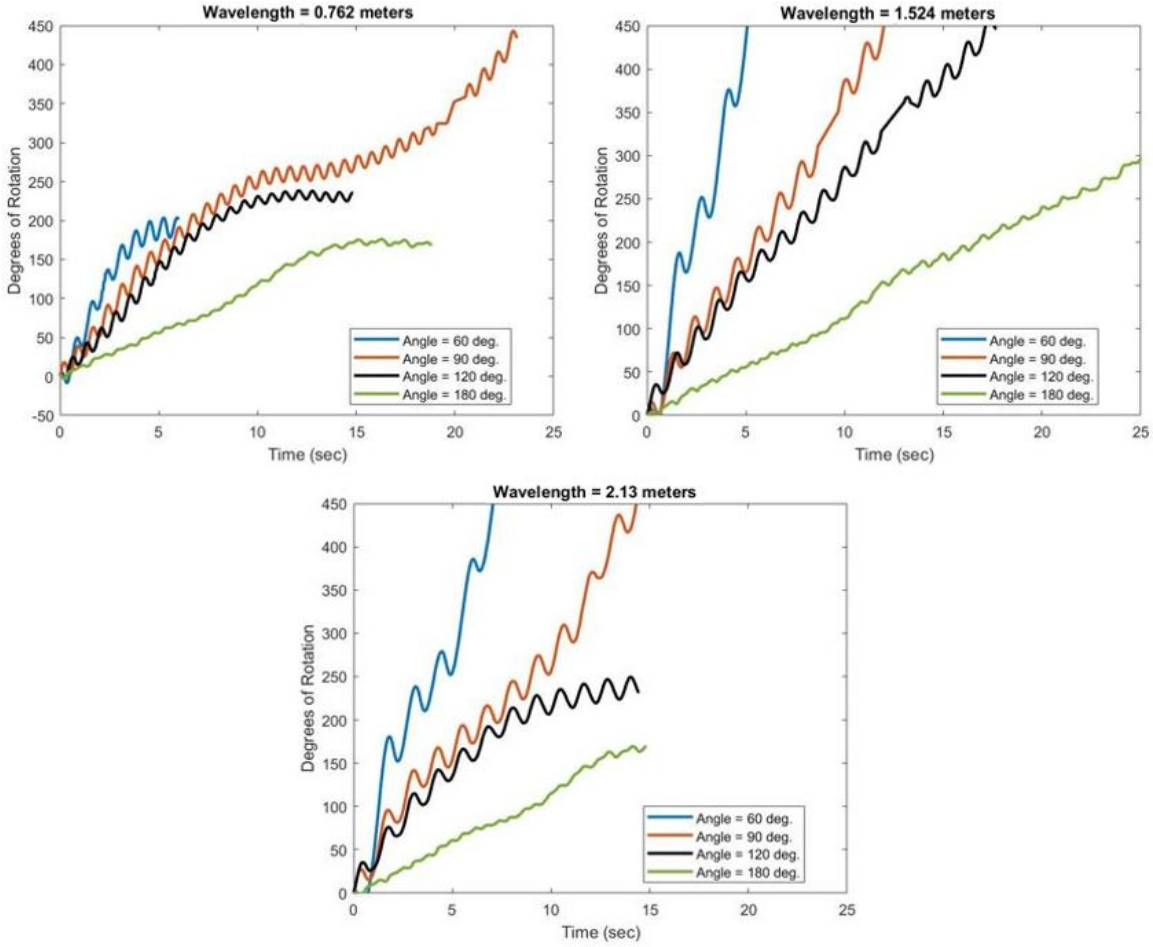

Figure 4.23. Two Blade Rotational Behavior at Trough Depth

For the shortest wavelength, all models were incapable of making a full rotation except for the 90 degree model. The performance significantly slowed down on the back half of the circular path, and the 90 degree model was the only one capable of making it back to the top. For the 180 degree model, the interruption was most likely due to the two blades fighting against each other while the other non-symmetrical models were affected by gravity more. The wave period was most likely too small, so it did not have enough time to rotate past the back half of the circle, or the positions where the model would most likely get stuck.

In the longest wavelength, the 60 degree and 90 degree models completed the full rotation. Both blades were most likely contributing to rotation, and the length of the wave period allowed it to rotate past the positions that it was most likely to get stuck. For 120 degree and 180 degree model, the net positive force received from the wave was most likely not enough to overcome the force of gravity and the opposing force from the wave. The middle wavelengths were the most optimal solution that allowed all models to make consistent rotations. The same analysis was conducted at the submerged depth as seen in Figure 4.24.

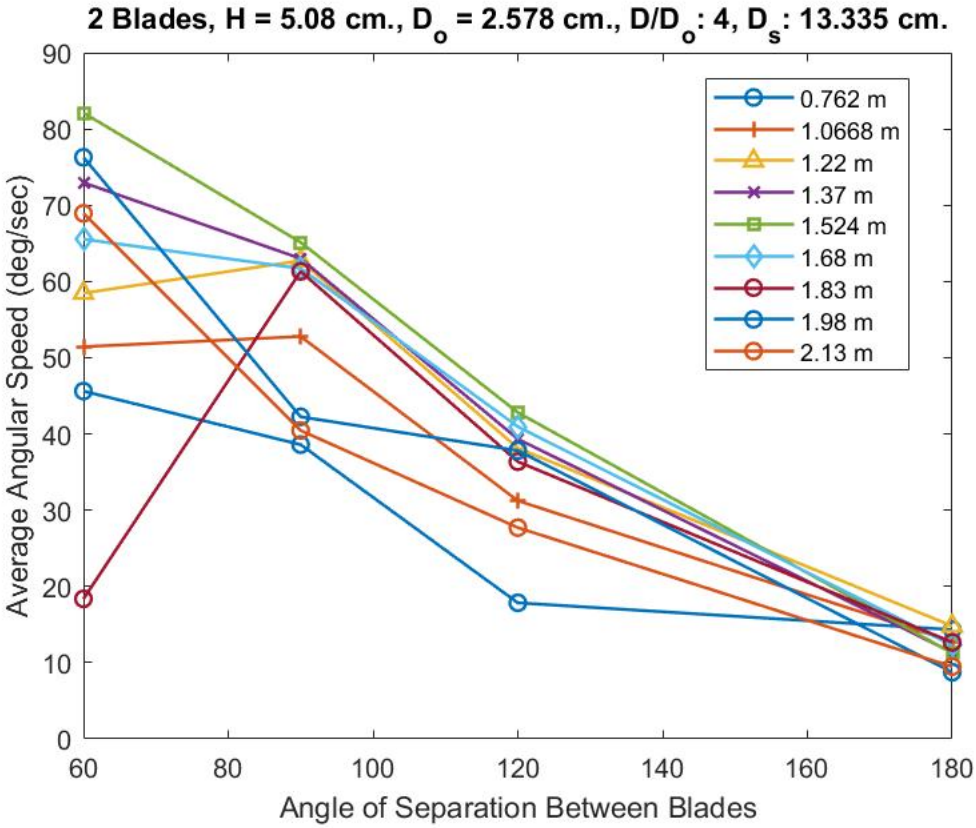

Figure 4.24. Two Blade Performance at Submerged Depth

The performance trend was the same as it was in the trough, but the average angular speed was decreased for all models. Also, many more runs resulted in non-full rotations.

The complete list of trials that did not complete a full rotation is provided in Appendix A. This behavior was further investigated in Figure 4.25.

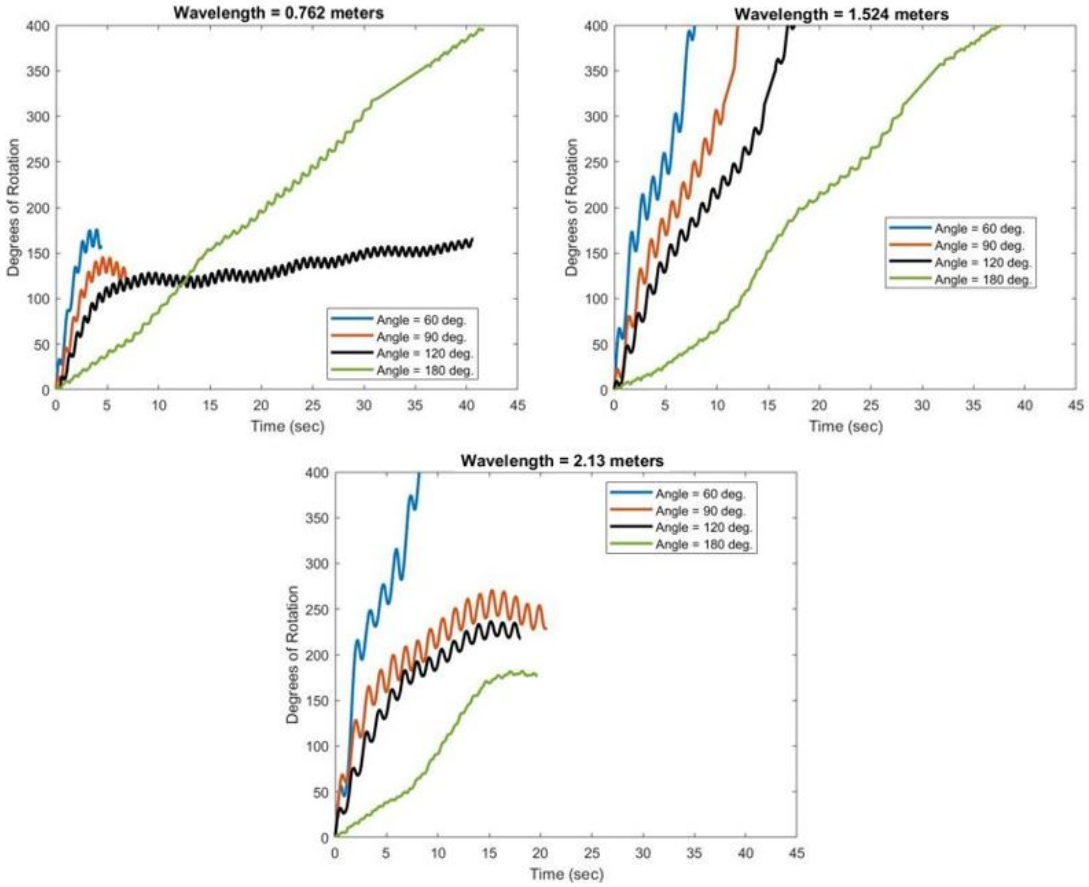

Figure 4.25. Two Blade Rotational Behavior at Submerged Depth

In the submerged case, the blades are receiving less force from the wave. At the same wave period and wavelength, this reduced force caused the model to get stuck either at or slightly past the bottom of the circle. From there, the force was too small to overcome the gravity of the unbalanced model or the negative contribution from the second blade. However, the 180 degree model was capable of making a full rotation at the submerged depth while not at the shallower depth. It was suggested that the blade on the bottom half of the model was receiving less force due to the submergence while the blade closer to the

free surface was causing more positive contribution towards rotation. All in all, putting two blades closer together caused the performance to increase, but the consistency in making a full rotation decreased compared to the three blade models of the same blade size.

Since the single blade model had the fastest average angular speed, the blade size was changed to closer to the three blade optimal D_o ratio. Figure 4.26 displays the results from this test.

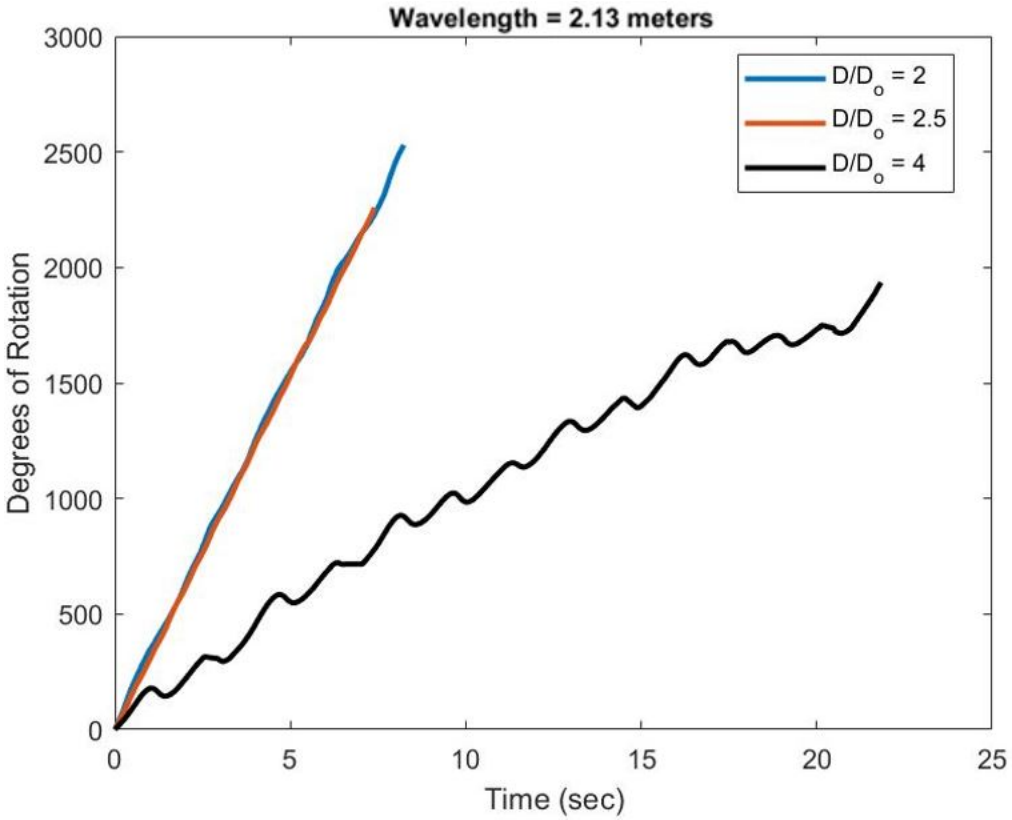

Figure 4.26. One Blade D/Do Performance Testing at Trough Depth and Wave Height of 5.08 cm.

The blue and red line models are both rotating at a constant rate of approximately the wave frequency. The figure only displays the results for the 2.13 meter wavelength trial because the black dot was too blurry for the image processing code to work on wavelength

trials shorter than 2.13 meters. This also only displays the results of the model at the trough depth. In this case, the single blade with the smaller D_o ratios would attempt to sync up with the wave. However, in the smallest blade size case, the rotation would not be consistent. The figure displays results when the blade was in sync with the wave, but it could not maintain this performance for an extended period of time. In addition, the same tests were conducted at the submerged depth. The majority of the runs resulted in non-full rotations for each model. The blade would make it towards the bottom of the circular path, but it would not have enough momentum or force from the wave to make a full rotation.

For the medium blade size in Figure 4.26, the rotation was consistently at the speed of the frequency of the wave. The model could rotate for over three minutes without a disruption in the rotation shown in the figure. Overall, the smaller blade sizes were able to reach the upper bound in performance for this model's angular speed, but the larger blade sizes were able to make full rotations more consistently.

4.7 Blade Mass

The purpose of this test was to determine if the blade mass had any significant effect on the difference in performance between the models. In this test, the thickness of the blade of the 2.5 D/D_o ratio was increased so the force of gravity of the blade was equivalent to the 4 D/D_o ratio model. The results are provided in Figure 4.27.

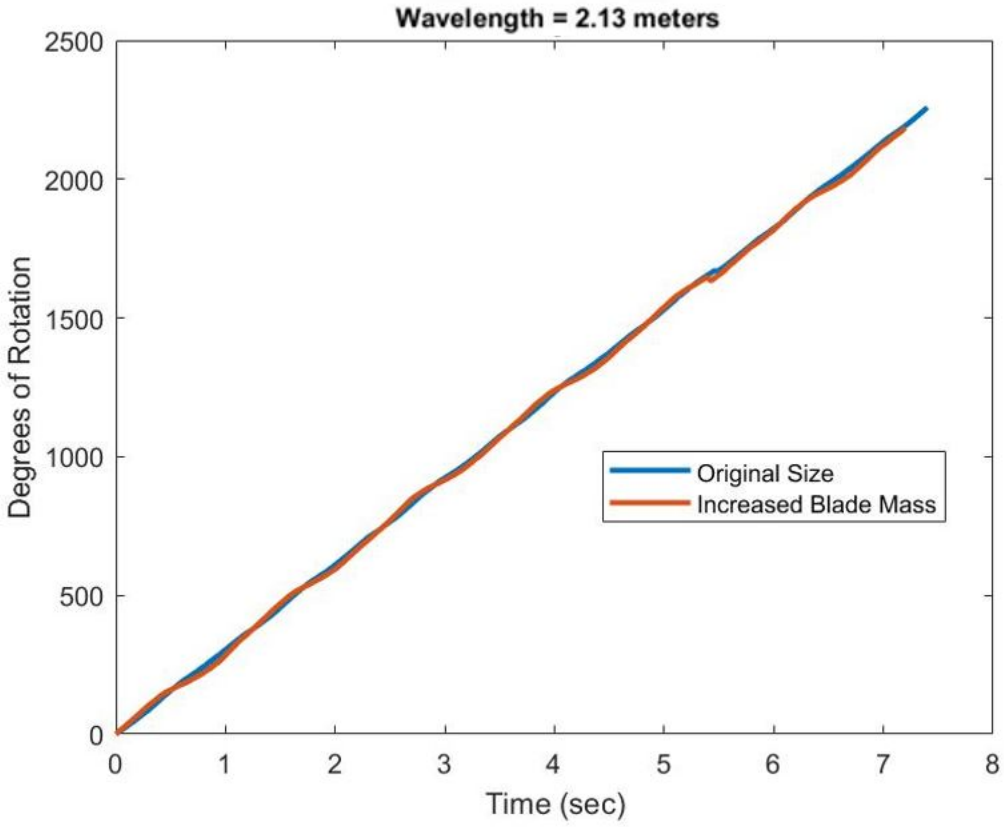

Figure 4.27. One Blade Gravity Performance Testing at Trough Depth and Wave Height of 5.08 cm.

The difference between the two tests were negligible. Therefore, it was assumed that the effect of the mass of the blade between the tested models would be negligible for the one blade tests. While blade mass could have an effect on the overall performance, the difference in mass would need to be larger in order to observe this change. A greater blade mass would increase the force of gravity acting on the blade, which would inhibit motion when rotating back up towards the free surface.

4.8 Test Variability

Variability tests were conducted to measure the change in average angular speed and rotational behavior at the same conditions for three trials. Due to the image processing time constraints, it was not feasible to conduct multiple trials for every condition. Figure 4.28 displays the results of the variability tests.

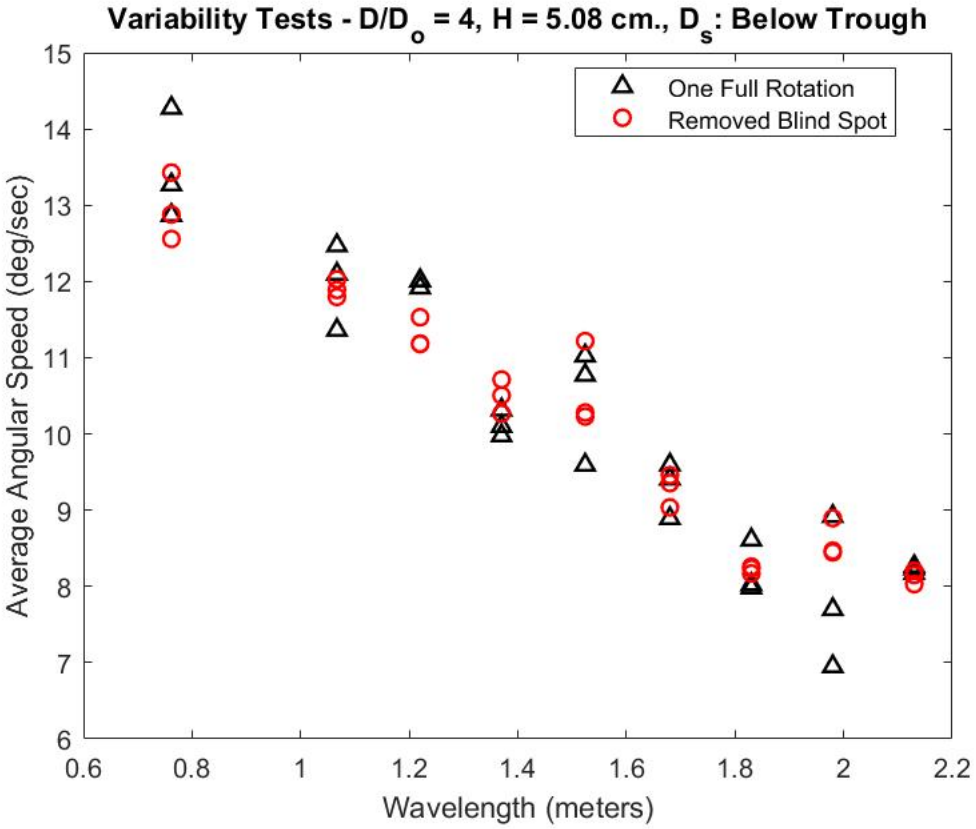

Figure 4.28. Average Angular Speeds Variability Tests

In general, the range of average angular speeds was approximately 1.5 degrees per second for each wave condition in the three blade models. In the image processing code, the average angular speed "removing the blind spot" was also conducted in order to see if there was any major differences in the performance without the constant speed assumption through the blind spot. The angular speed was calculated up until the last circle was detected

before it moved behind the end cap. The difference was mostly negligible and there was no trend in the difference between the speeds of one full rotation and without the blind spot. Therefore, the assumption was valid. The rotational behavior was investigated in Figure 4.29.

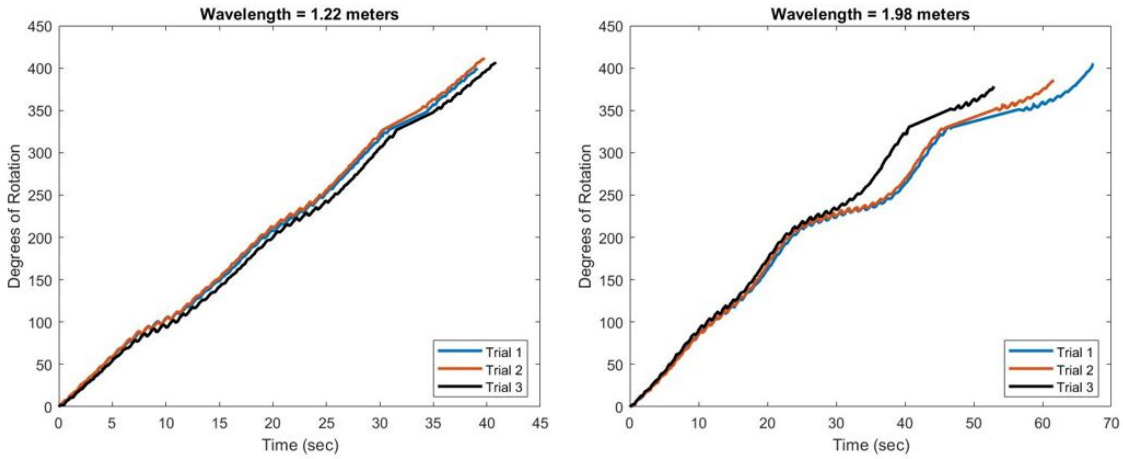

Figure 4.29. Rotational Behavior Variability Testing

For the trials that had a larger range in average angular speeds, it appeared that at least one of the trials was more successful in rotating out of one of the slower sections of the circle. This could have been due to multiple factors including a slightly different starting position of the blade. Overall, the general trends of the rotational behavior was the same, and the difference in the average angular rotation between three different trials was not significant enough to cast doubt on the observations made from that metric.

4.9 Wave Height Verification

In order to measure the wave height of the wave maker inputs more accurately, verification tests were conducted using acoustic sensors. Each wave input was ran once, and four different wave probes measured the average wave height for a 60 second run. Figures 4.30 and 4.31 display the results from the wave variability tests for wave heights of 2.54 cm and 5.08 cm.

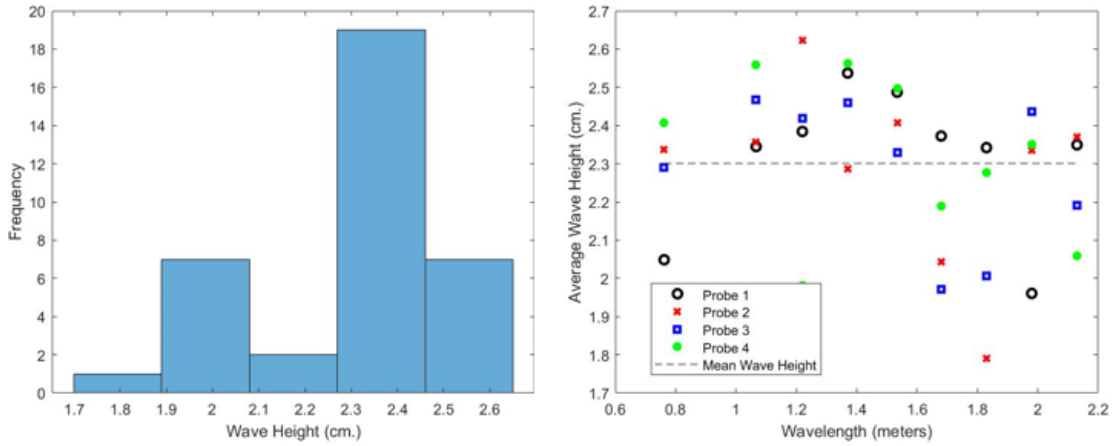

Figure 4.30. Wavemaker Variability Data for Wave Heights of 2.54 cm.

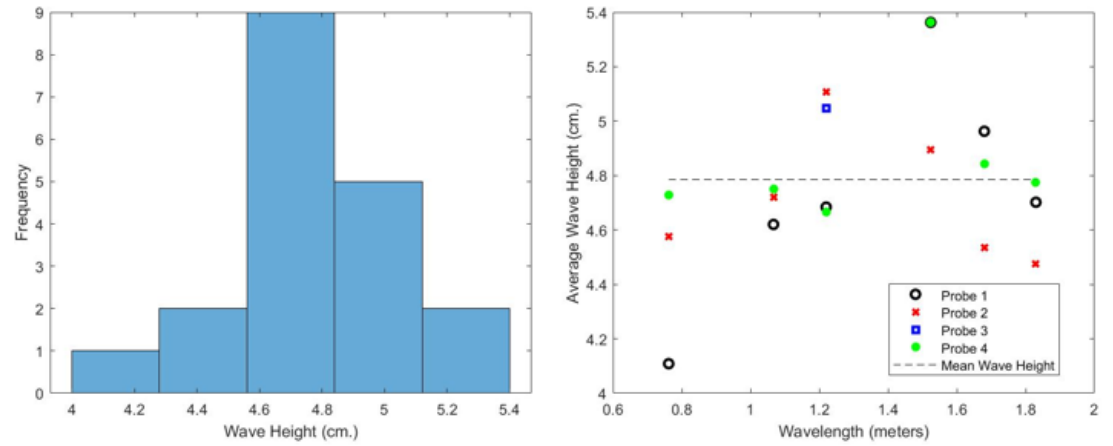

Figure 4.31. Wavemaker Variability Data for Wave Heights of 5.08 cm.

The average wave heights for each input was 2.3 cm and 4.79 cm, respectively. This average was calculated by taking the average wave heights from each probe and combining it with the other trials with the same wave height. Each individual probe data was also plotted in order to determine if there was a bias in the wave probes and if there was a trend in wave height as a function of wave length. It did not appear that this was the case. While the wave heights were not exactly 2.54 cm and 5.08 cm, the wave heights were within 90

percent of the intended input and the 5.08 cm waves were approximately double the 2.54 cm waves. The same analysis was conducted for the 7.62 cm wave heights, and there were no observable trends in that data as well. The average wave height for the 7.62 cm wave input was 7.34 cm.

CHAPTER 5:
Conclusion

5.1 Summary of Results

In this experiment, several trends in performance were observed due to a change in model parameters. While it is not definitively known why these changes occurred, the experiment provided useful information that was used in determining optimal hydro-turbine design for a TENG. A summary of the results from chapter 4 is provided for convenience.

A larger sized model caused a decrease in average angular speed over one full rotation. By increasing the model outer diameter or the blade size, it required more force to generate the same amount of rotation. The larger blades would receive more force from the wave, but the added mass and drag would also increase. In this case, the increased added mass and drag had a greater negative effect. Also, when the waves were shorter and thus the forcing frequency increased, the larger models could not benefit from its momentum. The model was receiving more force from the wave, but before it could fully rotate, the wave would already be acting against the blades. However, in small models, the higher forcing frequency allowed significant rotation to move past blade positions that yielded slower angular speed.

A larger incoming wave height yielded faster rotation in every model that was tested. In addition, the increase in speed from 2.54 cm to 5.08 cm was greater than the increase in speed from 5.08 cm to 7.62 cm. The rotational behavior became more "jagged" at larger wave heights, so this could have attributed to this behavior.

There was no significant relationship between average angular speed and wavelength, but the wavelength contributed towards the rotational behavior and if the model could produce full rotations. As previously mentioned, larger models struggled more at the shorter wavelengths due to the higher forcing frequency. Also, at a wave height of 2.54 cm, there was a negative relationship between wavelength and average angular speed. However, at 5.08 cm, the performance was approximately the same for each model. At the shorter wavelengths, models could not rotate quick enough to rotate past positions that caused slower angular

speed. In the two bladed models, too high of a forcing frequency did not allow the model enough time to work against gravity back up to the free surface. Conversely, too low of a frequency would allow the blades to fall back down towards the bottom of the tank before receiving a contributing wave force.

Blade size had a significant impact on rotational speed. For three blade models, it was determined that the optimal value for the D/D_o ratio was between two and three. If the blade size was too small, not enough wave force would be received to rotate efficiently. Also, smaller blades were less likely to complete a full rotation, especially at more submerged depths.

From the two major depths that all models were tested at, the more submerged models performed worse than if they were positioned directly underneath the free surface. This was expected since the force from the wave decreased exponentially with depth. When incrementally increasing the depth, the force from the shorter wavelengths became too small to rotate the model while the longer wavelengths only had a marginal decrease in performance.

Out of all of the parameters, the number of blades had the most significant effect on the average angular speed. The fastest a three bladed model could rotate was approximately 23 degrees per second, and the slowest one bladed model tested at the trough depth had an average angular speed of 50 degrees per second. Even if the one blade model could not complete a full rotation, the average angular speed when oscillating around a fixed point was still greater than any three bladed model case. It was believed that not all blades in the three bladed model were positively contributing to the rotation. For the two bladed models, as the angle of separation between the blades decreased, it approached the performance of the one blade model. However, the model would become more off balanced, and it would hinder its ability to always make a full rotation.

All in all, the one blade model at a D/D_o ratio of 2.5 rotated the fastest at 526 degrees per second. The speed was in tune with the wave frequency of 1.462 Hz and a wave height of 5.08 centimeters. It was theorized that for the model at this scale, the fastest it could rotate was the period of the wave.

5.2 Practical Application of Results

In regards to TENG, the direction of the rotation does not matter. Therefore, the average angular speed was analyzed rather than the average angular velocity. With a greater speed, more rotation would occur, and thus greater relative motion between the two materials. This would increase the friction and power output. Full rotations as also not a requirement, so the cases where the model oscillates back and forth around a fixed point would still contribute towards energy harvesting.

In order to utilize a TENG WEC on a UUV, the model would need to have a balance between rotational speed, consistency, and versatility. If the model was only able to rotate at a certain wavelength or wave height, then it would be less useful in an unpredictable ocean environment. Also, it was assumed that a UUV would be capable of changing its depth to a more optimal location. While some models were not effective at larger depths, the submerged performance was not considered because of this assumption.

The three blade models were always more consistent in terms of completing a full rotation, but the speed of a one blade model would create significantly more energy. At the D/D_o ratio of 2.5, the model was able to consistently make rotations at the wave frequency close to the free surface. In prior thesis work, rotating the TENG at 90 RPM was able to light 120 LEDs (90 Volts). At the 0.762 meter wavelength with a wave frequency of 1.46, it is predicted that the model could produce a similar output.

The prior testing conducted by June Capelle was done in a controlled environment. In other words, there was very little source of error when rotating one of the cylinders with a motor on dry land. In a wave energy device, the TENG would have to be water tight for the electrical components. Also, there was a slight gap between the PVC and inner diameter of the model in this experiment. In order for the TENG to be most efficient, there needs to be as much contact area between the two materials as possible. Therefore, the rotation due to waves would be slightly different. The gap most likely hindered rotation since the models would “wobble” due to the waves, but the contact area would increase friction towards rotation. In a more practical TENG model, this gap would not exist.

5.3 Future Work/Suggestions

While this experiment uncovered several behaviors and trends in a wave powered horizontal axis hydro-turbine, it was not definitively clear why the behaviors occurred. In order to better understand the flow around the model, illuminating beads or neutrally buoyant particles could be placed in the tank to observe the fluid flow during a run. More specifically, it would be beneficial to understand how the flow around the blades influenced rotation. Also, a CFD simulation could be used to qualitatively predict how a parameter would affect the performance of the model.

In terms of quantifying the energy output of the model, a TENG of identical size could be created and tested out of the water. For every run, there is data for the degrees of rotation over time. A motor could be used to replicate the rotation of the model due to the waves, and then the energy output could be measured. This would provide a more accurate prediction on the capability of one of the models.

An actual TENG model could be designed and placed into the tank to measure the energy output of the WEC. Water proofing the electrical components would be a difficult design process. The data could also be compared to the testing done out of the tank to understand the efficiency of the model and errors due to the wave energy source.

Lastly, it was unknown how much energy was being absorbed by the model while fully submerged. The model was absorbing some of the energy of the wave in order to rotate, so the downstream wave should have slightly lower energy than the upstream wave. This can be measured as a ratio between the two wave heights. Using this measurement, it would determine the amount of energy from the incoming wave that was absorbed by the model and the overall efficiency of the TENG WEC.

APPENDIX A:
Experimental Data Log

Misc. Comments

Color Legend

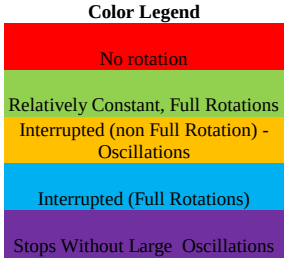

Analysis Files --> Add _Trim to Video Filename

T - Submergence Depth just below trough

Date	Model	Wave Height (in.)	Wavelength (ft.)	Submergence (in.)	Misc.	Video File	.mat Filename	Rotation Type
10-Dec-21	1	1	2.5	T	N/A	10DEC_Test1	D1T1	
10-Dec-21	1	1	3.5	T	N/A	10DEC_Test2	D1T2	
10-Dec-21	1	1	4	T	N/A	10DEC_Test3	D1T3	
10-Dec-21	1	1	4.5	T	N/A	10DEC_Test4	D1T4	
10-Dec-21	1	1	5	T	N/A	10DEC_Test5	D1T5	
10-Dec-21	1	1	5.5	T	N/A	10DEC_Test6	D1T6	
10-Dec-21	1	1	6	T	N/A	10DEC_Test7	D1T7	
10-Dec-21	1	1	6.5	T	N/A	10DEC_Test8	D1T8	
10-Dec-21	1	1	7	T	N/A	10DEC_Test9	D1T9	
10-Dec-21	1	2	2.5	T	N/A	10DEC_Test11	D1T11	
10-Dec-21	1	2	3.5	T	N/A	10DEC_Test12	D1T12	
10-Dec-21	1	2	4	T	N/A	10DEC_Test13	D1T13	
10-Dec-21	1	2	4.5	T	N/A	10DEC_Test14	D1T14	
10-Dec-21	1	2	5	T	N/A	10DEC_Test15	D1T15	
10-Dec-21	1	2	5.5	T	N/A	10DEC_Test16	D1T16	
10-Dec-21	1	2	6	T	N/A	10DEC_Test17	D1T17	
10-Dec-21	1	2	6.5	T	N/A	10DEC_Test18	D1T18	
10-Dec-21	1	2	7	T	N/A	10DEC_Test19	D1T19	
10-Dec-21	1	3	5.5	T	N/A	10DEC_Test21	D1T21	
10-Dec-21	1	3	6	T	N/A	10DEC_Test22	D1T22	
10-Dec-21	1	3	6.5	T	N/A	10DEC_Test23	D1T23	
16-Dec-21	2	1	2.5	T	N/A	16DEC_Test1	D2T1	
16-Dec-21	2	1	3.5	T	N/A	16DEC_Test2	D2T2	
16-Dec-21	2	1	4	T	N/A	16DEC_Test3	D2T3	
16-Dec-21	2	1	4.5	T	N/A	16DEC_Test4	D2T4	
16-Dec-21	2	1	5	T	N/A	16DEC_Test5	D2T5	
16-Dec-21	2	1	5.5	T	N/A	16DEC_Test6	D2T6	
16-Dec-21	2	1	6	T	N/A	16DEC_Test7	D2T7	
16-Dec-21	2	1	6.5	T	N/A	16DEC_Test8	D2T8	
16-Dec-21	2	1	7	T	N/A	16DEC_Test9	D2T9	
16-Dec-21	2	2	2.5	T	N/A	16DEC_Test11	D2T11	
16-Dec-21	2	2	3.5	T	N/A	16DEC_Test12	D2T12	
16-Dec-21	2	2	4	T	N/A	16DEC_Test13	D2T13	
16-Dec-21	2	2	4.5	T	N/A	16DEC_Test14	D2T14	
16-Dec-21	2	2	5	T	N/A	16DEC_Test15	D2T15	
16-Dec-21	2	2	5.5	T	N/A	16DEC_Test16	D2T16	
16-Dec-21	2	2	6	T	N/A	16DEC_Test17	D2T17	

16-Dec-21	2	2	6.5	T	N/A	16DEC_Test18	D2T18	
16-Dec-21	2	2	7	T	N/A	16DEC_Test19	D2T19	
16-Dec-21	2	3	5.5	T	N/A	16DEC_Test21	D2T20	
16-Dec-21	2	3	6	T	N/A	16DEC_Test22	D2T21	
16-Dec-21	2	3	6.5	T	N/A	16DEC_Test23	D2T22	
16-Dec-21	3	1	2.5	T	N/A	16DEC_Test31	D3T1	
16-Dec-21	3	1	3.5	T	N/A	16DEC_Test32	D3T2	
16-Dec-21	3	1	4	T	N/A	16DEC_Test33	D3T3	
16-Dec-21	3	1	4.5	T	N/A	16DEC_Test34	D3T4	
16-Dec-21	3	1	5	T	N/A	16DEC_Test35	D3T5	
16-Dec-21	3	1	5.5	T	N/A	16DEC_Test36	D3T6	
16-Dec-21	3	1	6	T	N/A	16DEC_Test37	D3T7	
16-Dec-21	3	2	2.5	T	N/A	16DEC_Test41	D3T11	
16-Dec-21	3	2	3.5	T	N/A	16DEC_Test42	D3T12	
16-Dec-21	3	2	4	T	N/A	16DEC_Test43	D3T13	
16-Dec-21	3	2	4.5	T	N/A	16DEC_Test44	D3T14	
16-Dec-21	3	2	5	T	N/A	16DEC_Test45	D3T15	
16-Dec-21	3	2	5.5	T	N/A	16DEC_Test46	D3T16	
16-Dec-21	3	2	6	T	N/A	16DEC_Test47	D3T17	
16-Dec-21	3	2	6.5	T	N/A	16DEC_Test48	D3T18	
16-Dec-21	3	2	7	T	N/A	16DEC_Test49	D3T19	
16-Dec-21	3	3	5.5	T	N/A	16DEC_Test51	D3T21	
16-Dec-21	3	3	6	T	N/A	16DEC_Test52	D3T22	
16-Dec-21	3	3	6.5	T	N/A	16DEC_Test53	D3T23	
4-Jan-22	4	1	2.5	T	N/A	4JAN_Test1	D4T1	
4-Jan-22	4	1	3.5	T	N/A	4JAN_Test2	D4T2	
4-Jan-22	4	1	4	T	N/A	4JAN_Test3	D4T3	
4-Jan-22	4	1	4.5	T	N/A	4JAN_Test4	D4T4	
4-Jan-22	4	1	5	T	N/A	4JAN_Test5	D4T5	
4-Jan-22	4	1	5.5	T	N/A	4JAN_Test6	D4T6	
4-Jan-22	4	1	6	T	N/A	4JAN_Test7	D4T7	
4-Jan-22	4	1	6.5	T	N/A	4JAN_Test8	D4T8	
4-Jan-22	4	1	7	T	N/A	4JAN_Test9	D4T9	
4-Jan-22	4	2	2.5	T	N/A	4JAN_Test11	D4T11	
4-Jan-22	4	2	3.5	T	N/A	4JAN_Test12	D4T12	
4-Jan-22	4	2	4	T	N/A	4JAN_Test13	D4T13	
4-Jan-22	4	2	4.5	T	N/A	4JAN_Test14	D4T14	
4-Jan-22	4	2	5	T	N/A	4JAN_Test15	D4T15	

4-Jan-22	4	2	5.5	T	N/A	4JAN_Test16	D4T16
4-Jan-22	4	2	6	T	N/A	4JAN_Test17	D4T17
4-Jan-22	4	2	6.5	T	N/A	4JAN_Test18	D4T18
4-Jan-22	4	2	7	T	N/A	4JAN_Test19	D4T19
4-Jan-22	4	3	5.5	T	N/A	4JAN_Test21	D4T21
4-Jan-22	4	3	6	T	N/A	4JAN_Test22	D4T22
4-Jan-22	4	3	6.5	T	N/A	4JAN_Test23	D4T23
6-Jan-22	1	2	2.5.	T	Variability Testing	6JAN_Test11	D1RT11
6-Jan-22	1	2	2.5	T	Variability Testing	6JAN_Test12	D1RT12
6-Jan-22	1	2	2.5	T	Variability Testing	6JAN_Test13	D1RT13
6-Jan-22	1	2	3.5	T	Variability Testing	6JAN_Test21	D1RT21
6-Jan-22	1	2	3.5	T	Variability Testing	6JAN_Test22	D1RT22
6-Jan-22	1	2	3.5	T	Variability Testing	6JAN_Test23	D1RT23
6-Jan-22	1	2	4	T	Variability Testing	6JAN_Test31	D1RT31
6-Jan-22	1	2	4	T	Variability Testing	6JAN_Test32	D1RT32
6-Jan-22	1	2	4	T	Variability Testing	6JAN_Test33	D1RT33
6-Jan-22	1	2	4.5	T	Variability Testing	6JAN_Test41	D1RT41
6-Jan-22	1	2	4.5	T	Variability Testing	6JAN_Test42	D1RT42
6-Jan-22	1	2	4.5	T	Variability Testing	6JAN_Test43	D1RT43
6-Jan-22	1	2	5	T	Variability Testing	6JAN_Test51	D1RT51
6-Jan-22	1	2	5	T	Variability Testing	6JAN_Test52	D1RT52
6-Jan-22	1	2	5	T	Variability Testing	6JAN_Test53	D1RT53
6-Jan-22	1	2	5.5	T	Variability Testing	6JAN_Test61	D1RT61
6-Jan-22	1	2	5.5	T	Variability Testing	6JAN_Test62	D1RT62
6-Jan-22	1	2	5.5	T	Variability Testing	6JAN_Test63	D1RT63
6-Jan-22	1	2	6	T	Variability Testing	6JAN_Test71	D1RT71
6-Jan-22	1	2	6	T	Variability Testing	6JAN_Test72	D1RT72
6-Jan-22	1	2	6	T	Variability Testing	6JAN_Test73	D1RT73
6-Jan-22	1	2	6.5	T	Variability Testing	6JAN_Test81	D1RT81
6-Jan-22	1	2	6.5	T	Variability Testing	6JAN_Test82	D1RT82
6-Jan-22	1	2	6.5	T	Variability Testing	6JAN_Test83	D1RT83
6-Jan-22	1	2	7	T	Variability Testing	6JAN_Test91	D1RT91
6-Jan-22	1	2	7	T	Variability Testing	6JAN_Test92	D1RT92
6-Jan-22	1	2	7	T	Variability Testing	6JAN_Test93	D1RT93
10-Jan-22	6	2	2.5	T	N/A	10JAN_Test1	D6T11
10-Jan-22	6	2	3.5	T	N/A	10JAN_Test2	D6T12
10-Jan-22	6	2	4	T	N/A	10JAN_Test3	D6T13
10-Jan-22	6	2	4.5	T	N/A	10JAN_Test4	D6T14

10-Jan-22	6	2	5	T	N/A	10JAN_Test5	D6T15
10-Jan-22	6	2	5.5	T	N/A	10JAN_Test6	D6T16
10-Jan-22	6	2	6	T	N/A	10JAN_Test7	D6T17
10-Jan-22	6	2	6.5	T	N/A	10JAN_Test8	D6T18
10-Jan-22	6	2	7	T	N/A	10JAN_Test9	D6T19
10-Jan-22	7	2	2.5	T	N/A	10JAN_Test11	D7T11
10-Jan-22	7	2	3.5	T	N/A	10JAN_Test12	D7T12
10-Jan-22	7	2	4	T	N/A	10JAN_Test13	D7T13
10-Jan-22	7	2	4.5	T	N/A	10JAN_Test14	D7T14
10-Jan-22	7	2	5	T	N/A	10JAN_Test15	D7T15
10-Jan-22	7	2	5.5	T	N/A	10JAN_Test16	D7T16
10-Jan-22	7	2	6	T	N/A	10JAN_Test17	D7T17
10-Jan-22	7	2	6.5	T	N/A	10JAN_Test18	D7T18
10-Jan-22	7	2	7	T	N/A	10JAN_Test19	D7T19
12-Jan-22	5	2	2.5	T	N/A	12JAN_Test11	D5T11
12-Jan-22	5	2	3.5	T	N/A	12JAN_Test12	D5T12
12-Jan-22	5	2	4	T	N/A	12JAN_Test13	D5T13
12-Jan-22	5	2	4.5	T	N/A	12JAN_Test14	D5T14
12-Jan-22	5	2	5	T	N/A	12JAN_Test15	D5T15
12-Jan-22	5	2	5.5	T	N/A	12JAN_Test16	D5T16
12-Jan-22	5	2	6	T	N/A	12JAN_Test17	D5T17
12-Jan-22	5	2	6.5	T	N/A	12JAN_Test18	D5T18
12-Jan-22	5	2	7	T	N/A	12JAN_Test19	D5T19
13-Jan-22	3	2	2.5	5.25	Submergence Testing	13JAN_Test1	D3ST11
13-Jan-22	3	2	3.5	5.25	Submergence Testing	13JAN_Test2	D3ST12
13-Jan-22	3	2	4	5.25	Submergence Testing	13JAN_Test3	D3ST13
13-Jan-22	3	2	4.5	5.25	Submergence Testing	13JAN_Test4	D3ST14
13-Jan-22	3	2	5	5.25	Submergence Testing	13JAN_Test5	D3ST15
13-Jan-22	3	2	5.5	5.25	Submergence Testing	13JAN_Test6	D3ST16
13-Jan-22	3	2	6	5.25	Submergence Testing	13JAN_Test7	D3ST17
13-Jan-22	3	2	6.5	5.25	Submergence Testing	13JAN_Test8	D3ST18
13-Jan-22	3	2	7	5.25	Submergence Testing	13JAN_Test9	D3ST19
13-Jan-22	2	2	2.5	5.25	Submergence Testing	13JAN_Test11	D2ST11
13-Jan-22	2	2	3.5	5.25	Submergence Testing	13JAN_Test12	D2ST12
13-Jan-22	2	2	4	5.25	Submergence Testing	13JAN_Test13	D2ST13
13-Jan-22	2	2	4.5	5.25	Submergence Testing	13JAN_Test14	D2ST14
13-Jan-22	2	2	5	5.25	Submergence Testing	13JAN_Test15	D2ST15
13-Jan-22	2	2	5.5	5.25	Submergence Testing	13JAN_Test16	D2ST16

13-Jan-22	2	2	6	5.25	Submergence Testing	13JAN_Test17	D2ST17
13-Jan-22	2	2	6.5	5.25	Submergence Testing	13JAN_Test18	D2ST18
13-Jan-22	2	2	7	5.25	Submergence Testing	13JAN_Test19	D2ST19
18-Jan-22	1	2	2.5	5.25	Submergence Testing	18JAN_Test1	D1ST11
18-Jan-22	1	2	3.5	5.25	Submergence Testing	18JAN_Test2	D1ST12
18-Jan-22	1	2	4	5.25	Submergence Testing	18JAN_Test3	D1ST13
18-Jan-22	1	2	4.5	5.25	Submergence Testing	18JAN_Test4	D1ST14
18-Jan-22	1	2	5	5.25	Submergence Testing	18JAN_Test5	D1ST15
18-Jan-22	1	2	5.5	5.25	Submergence Testing	18JAN_Test6	D1ST16
18-Jan-22	1	2	6	5.25	Submergence Testing	18JAN_Test7	D1ST17
18-Jan-22	1	2	6.5	5.25	Submergence Testing	18JAN_Test8	D1ST18
18-Jan-22	1	2	7	5.25	Submergence Testing	18JAN_Test9	D1ST19
18-Jan-22	6	2	2.5	5.25	Submergence Testing	18JAN_Test11	D6ST11
18-Jan-22	6	2	3.5	5.25	Submergence Testing	18JAN_Test12	D6ST12
18-Jan-22	6	2	4	5.25	Submergence Testing	18JAN_Test13	D6ST13
18-Jan-22	6	2	4.5	5.25	Submergence Testing	18JAN_Test14	D6ST14
18-Jan-22	6	2	5	5.25	Submergence Testing	18JAN_Test15	D6ST15
18-Jan-22	6	2	5.5	5.25	Submergence Testing	18JAN_Test16	D6ST16
18-Jan-22	6	2	6	5.25	Submergence Testing	18JAN_Test17	D6ST17
18-Jan-22	6	2	6.5	5.25	Submergence Testing	18JAN_Test18	D6ST18
18-Jan-22	6	2	7	5.25	Submergence Testing	18JAN_Test19	D6ST19
18-Jan-22	7	2	2.5	5.25	Submergence Testing	18JAN_Test21	D7ST11
18-Jan-22	7	2	3.5	5.25	Submergence Testing	18JAN_Test22	D7ST12
18-Jan-22	7	2	4	5.25	Submergence Testing	18JAN_Test23	D7ST13
18-Jan-22	7	2	4.5	5.25	Submergence Testing	18JAN_Test24	D7ST14
18-Jan-22	7	2	5	5.25	Submergence Testing	18JAN_Test25	D7ST15
18-Jan-22	7	2	5.5	5.25	Submergence Testing	18JAN_Test26	D7ST16
18-Jan-22	7	2	6	5.25	Submergence Testing	18JAN_Test27	D7ST17
18-Jan-22	7	2	6.5	5.25	Submergence Testing	18JAN_Test28	D7ST18
18-Jan-22	7	2	7	5.25	Submergence Testing	18JAN_Test29	D7ST19
19-Jan-22	1	2	2.5	T	Variable Depth Testing	19JAN_Test1	D1V0T11
19-Jan-22	1	2	3.5	T	Variable Depth Testing	19JAN_Test2	D1V0T12
19-Jan-22	1	2	4	T	Variable Depth Testing	19JAN_Test3	D1V0T13
19-Jan-22	1	2	4.5	T	Variable Depth Testing	19JAN_Test4	D1V0T14
19-Jan-22	1	2	5	T	Variable Depth Testing	19JAN_Test5	D1V0T15
19-Jan-22	1	2	5.5	T	Variable Depth Testing	19JAN_Test6	D1V0T16
19-Jan-22	1	2	6	T	Variable Depth Testing	19JAN_Test7	D1V0T17
19-Jan-22	1	2	6.5	T	Variable Depth Testing	19JAN_Test8	D1V0T18

19-Jan-22	1	2	7	T	Variable Depth Testing	19JAN_Test9	D1V0T19
19-Jan-22	1	2	2.5	T-1	Variable Depth Testing	19JAN_Test11	D1V1T11
19-Jan-22	1	2	3.5	T-1	Variable Depth Testing	19JAN_Test12	D1V1T12
19-Jan-22	1	2	4	T-1	Variable Depth Testing	19JAN_Test13	D1V1T13
19-Jan-22	1	2	4.5	T-1	Variable Depth Testing	19JAN_Test14	D1V1T14
19-Jan-22	1	2	5	T-1	Variable Depth Testing	19JAN_Test15	D1V1T15
19-Jan-22	1	2	5.5	T-1	Variable Depth Testing	19JAN_Test16	D1V1T16
19-Jan-22	1	2	6	T-1	Variable Depth Testing	19JAN_Test17	D1V1T17
19-Jan-22	1	2	6.5	T-1	Variable Depth Testing	19JAN_Test18	D1V1T18
19-Jan-22	1	2	7	T-1	Variable Depth Testing	19JAN_Test19	D1V1T19
19-Jan-22	1	2	2.5	T-2	Variable Depth Testing	19JAN_Test21	D1V2T11
19-Jan-22	1	2	3.5	T-2	Variable Depth Testing	19JAN_Test22	D1V2T12
19-Jan-22	1	2	4	T-2	Variable Depth Testing	19JAN_Test23	D1V2T13
19-Jan-22	1	2	4.5	T-2	Variable Depth Testing	19JAN_Test24	D1V2T14
19-Jan-22	1	2	5	T-2	Variable Depth Testing	19JAN_Test25	D1V2T15
19-Jan-22	1	2	5.5	T-2	Variable Depth Testing	19JAN_Test26	D1V2T16
19-Jan-22	1	2	6	T-2	Variable Depth Testing	19JAN_Test27	D1V2T17
19-Jan-22	1	2	6.5	T-2	Variable Depth Testing	19JAN_Test28	D1V2T18
19-Jan-22	1	2	7	T-2	Variable Depth Testing	19JAN_Test29	D1V2T19
20-Jan-22	1	2	2.5	T-3	Variable Depth Testing	20JAN_Test1	D1V3T11
20-Jan-22	1	2	3.5	T-3	Variable Depth Testing	20JAN_Test2	D1V3T12
20-Jan-22	1	2	4	T-3	Variable Depth Testing	20JAN_Test3	D1V3T13
20-Jan-22	1	2	4.5	T-3	Variable Depth Testing	20JAN_Test4	D1V3T14
20-Jan-22	1	2	5	T-3	Variable Depth Testing	20JAN_Test5	D1V3T15
20-Jan-22	1	2	5.5	T-3	Variable Depth Testing	20JAN_Test6	D1V3T16
20-Jan-22	1	2	6	T-3	Variable Depth Testing	20JAN_Test7	D1V3T17
20-Jan-22	1	2	6.5	T-3	Variable Depth Testing	20JAN_Test8	D1V3T18
20-Jan-22	1	2	7	T-3	Variable Depth Testing	20JAN_Test9	D1V3T19
20-Jan-22	1	2	2.5	T-4	Variable Depth Testing	20JAN_Test11	D1V4T11
20-Jan-22	1	2	3.5	T-4	Variable Depth Testing	20JAN_Test12	D1V4T12
20-Jan-22	1	2	4	T-4	Variable Depth Testing	20JAN_Test13	D1V4T13
20-Jan-22	1	2	4.5	T-4	Variable Depth Testing	20JAN_Test14	D1V4T14
20-Jan-22	1	2	5	T-4	Variable Depth Testing	20JAN_Test15	D1V4T15
20-Jan-22	1	2	5.5	T-4	Variable Depth Testing	20JAN_Test16	D1V4T16
20-Jan-22	1	2	6	T-4	Variable Depth Testing	20JAN_Test17	D1V4T17
20-Jan-22	1	2	6.5	T-4	Variable Depth Testing	20JAN_Test18	D1V4T18
20-Jan-22	1	2	7	T-4	Variable Depth Testing	20JAN_Test19	D1V4T19
20-Jan-22	1	2	2.5	T-6	Variable Depth Testing	20JAN_Test21	D1V6T11

20-Jan-22	1	2	3.5	T-6	Variable Depth Testing	20JAN_Test22	D1V6T12	
20-Jan-22	1	2	4	T-6	Variable Depth Testing	20JAN_Test23	D1V6T13	
20-Jan-22	1	2	4.5	T-6	Variable Depth Testing	20JAN_Test24	D1V6T14	
20-Jan-22	1	2	5	T-6	Variable Depth Testing	20JAN_Test25	D1V6T15	
20-Jan-22	1	2	5.5	T-6	Variable Depth Testing	20JAN_Test26	D1V6T16	
20-Jan-22	1	2	6	T-6	Variable Depth Testing	20JAN_Test27	D1V6T17	
20-Jan-22	1	2	6.5	T-6	Variable Depth Testing	20JAN_Test28	D1V6T18	
20-Jan-22	1	2	7	T-6	Variable Depth Testing	20JAN_Test29	D1V6T19	
20-Jan-22	1	2	2.5	T-8	Variable Depth Testing			
20-Jan-22	1	2	3.5	T-8	Variable Depth Testing	20JAN_Test32	D1V8T12	
20-Jan-22	1	2	4	T-8	Variable Depth Testing	20JAN_Test33	D1V8T13	
20-Jan-22	1	2	4.5	T-8	Variable Depth Testing	20JAN_Test34	D1V8T14	
20-Jan-22	1	2	5	T-8	Variable Depth Testing	20JAN_Test35	D1V8T15	
20-Jan-22	1	2	5.5	T-8	Variable Depth Testing	20JAN_Test36	D1V8T16	
20-Jan-22	1	2	6	T-8	Variable Depth Testing	20JAN_Test37	D1V8T17	
20-Jan-22	1	2	6.5	T-8	Variable Depth Testing	20JAN_Test38	D1V8T18	
20-Jan-22	1	2	7	T-8	Variable Depth Testing	20JAN_Test39	D1V8T19	
28-Jan-22	8	2	2.5	5.25	Submergence Testing	28JAN_Test1	D8ST11	
28-Jan-22	8	2	3.5	5.25	Submergence Testing	28JAN_Test2	D8ST12	
28-Jan-22	8	2	4	5.25	Submergence Testing	28JAN_Test3	D8ST13	
28-Jan-22	8	2	4.5	5.25	Submergence Testing	28JAN_Test4	D8ST14	
28-Jan-22	8	2	5	5.25	Submergence Testing	28JAN_Test5	D8ST15	
28-Jan-22	8	2	5.5	5.25	Submergence Testing	28JAN_Test6	D8ST16	
28-Jan-22	8	2	6	5.25	Submergence Testing	28JAN_Test7	D8ST17	
28-Jan-22	8	2	6.5	5.25	Submergence Testing	28JAN_Test8	D8ST18	
28-Jan-22	8	2	7	5.25	Submergence Testing	28JAN_Test9	D8ST19	
2-Feb-22	8	2	2.5	T	N/A	2FEB_Test21	D8T11	
2-Feb-22	8	2	3.5	T	N/A	2FEB_Test22	D8T12	
2-Feb-22	8	2	4	T	N/A	2FEB_Test23	D8T13	
2-Feb-22	8	2	4.5	T	N/A	2FEB_Test24	D8T14	
2-Feb-22	8	2	5	T	N/A	2FEB_Test25	D8T15	
2-Feb-22	8	2	5.5	T	N/A	2FEB_Test26	D8T16	
2-Feb-22	8	2	6	T	N/A	2FEB_Test27	D8T17	
2-Feb-22	8	2	6.5	T	N/A	2FEB_Test28	D8T18	
2-Feb-22	8	2	7	T	N/A	2FEB_Test29	D8T19	
2-Feb-22	9	2	2.5	T	N/A	2FEB_Test31	D9T11	
2-Feb-22	9	2	3.5	T	N/A	2FEB_Test32	D9T12	
2-Feb-22	9	2	4	T	N/A	2FEB_Test33	D9T13	

2-Feb-22	9	2	4.5	T	N/A	2FEB_Test34	D9T14	
2-Feb-22	9	2	5	T	N/A	2FEB_Test35	D9T15	
2-Feb-22	9	2	5.5	T	N/A	2FEB_Test36	D9T16	
2-Feb-22	9	2	6	T	N/A	2FEB_Test37	D9T17	
2-Feb-22	1 - 1 BLADE	2	2.5	T	N/A	2FEB_Test1	D1BT11	
2-Feb-22	1 - 1 BLADE	2	3.5	T	N/A	2FEB_Test2	D1BT12	
2-Feb-22	1 - 1 BLADE	2	4	T	N/A	2FEB_Test3	D1BT13	
2-Feb-22	1 - 1 BLADE	2	4.5	T	N/A	2FEB_Test4	D1BT14	
2-Feb-22	1 - 1 BLADE	2	5	T	N/A	2FEB_Test5	D1BT15	
2-Feb-22	1 - 1 BLADE	2	5.5	T	N/A	2FEB_Test6	D1BT16	
2-Feb-22	1 - 1 BLADE	2	6	T	N/A	2FEB_Test7	D1BT17	
2-Feb-22	1 - 1 BLADE	2	6.5	T	N/A	2FEB_Test8	D1BT18	
2-Feb-22	1 - 1 BLADE	2	7	T	N/A	2FEB_Test9	D1BT19	
2-Feb-22	1 - 1 BLADE	2	2.5	5.25	Submergence Testing	2FEB_Test11	D1BST11	
2-Feb-22	1 - 1 BLADE	2	3.5	5.25	Submergence Testing	2FEB_Test12	D1BST12	
2-Feb-22	1 - 1 BLADE	2	4	5.25	Submergence Testing	2FEB_Test13	D1BST13	
2-Feb-22	1 - 1 BLADE	2	4.5	5.25	Submergence Testing	2FEB_Test14	D1BST14	
2-Feb-22	1 - 1 BLADE	2	5	5.25	Submergence Testing	2FEB_Test15	D1BST15	
2-Feb-22	1 - 1 BLADE	2	5.5	5.25	Submergence Testing	2FEB_Test16	D1BST16	
2-Feb-22	1 - 1 BLADE	2	6	5.25	Submergence Testing	2FEB_Test17	D1BST17	
2-Feb-22	1 - 1 BLADE	2	6.5	5.25	Submergence Testing	2FEB_Test18	D1BST18	
2-Feb-22	1 - 1 BLADE	2	7	5.25	Submergence Testing	2FEB_Test19	D1BST19	
4-Feb-22	1 - 2 BLADE (180 DEG)	2	2.5	5.25	Submergence Testing	4FEB_Test1	D2B180ST11	
4-Feb-22	1 - 2 BLADE (180 DEG)	2	3.5	5.25	Submergence Testing	4FEB_Test2	D2B180ST12	
4-Feb-22	1 - 2 BLADE (180 DEG)	2	4	5.25	Submergence Testing	4FEB_Test3	D2B180ST13	
4-Feb-22	1 - 2 BLADE (180 DEG)	2	4.5	5.25	Submergence Testing	4FEB_Test4	D2B180ST14	
4-Feb-22	1 - 2 BLADE (180 DEG)	2	5	5.25	Submergence Testing	4FEB_Test5	D2B180ST15	
4-Feb-22	1 - 2 BLADE (180 DEG)	2	5.5	5.25	Submergence Testing	4FEB_Test6	D2B180ST16	
4-Feb-22	1 - 2 BLADE (180 DEG)	2	6	5.25	Submergence Testing	4FEB_Test7	D2B180ST17	
4-Feb-22	1 - 2 BLADE (180 DEG)	2	6.5	5.25	Submergence Testing	4FEB_Test8	D2B180ST18	
4-Feb-22	1 - 2 BLADE (180 DEG)	2	7	5.25	Submergence Testing	4FEB_Test9	D2B180ST19	
4-Feb-22	1 - 2 BLADE (120 DEG)	2	2.5	5.25	Submergence Testing	4FEB_Test11	D2B120ST11	
4-Feb-22	1 - 2 BLADE (120 DEG)	2	3.5	5.25	Submergence Testing	4FEB_Test12	D2B120ST12	
4-Feb-22	1 - 2 BLADE (120 DEG)	2	4	5.25	Submergence Testing	4FEB_Test13	D2B120ST13	
4-Feb-22	1 - 2 BLADE (120 DEG)	2	4.5	5.25	Submergence Testing	4FEB_Test14	D2B120ST14	
4-Feb-22	1 - 2 BLADE (120 DEG)	2	5	5.25	Submergence Testing	4FEB_Test15	D2B120ST15	
4-Feb-22	1 - 2 BLADE (120 DEG)	2	5.5	5.25	Submergence Testing	4FEB_Test16	D2B120ST16	
4-Feb-22	1 - 2 BLADE (120 DEG)	2	6	5.25	Submergence Testing	4FEB_Test17	D2B120ST17	

4-Feb-22	1 - 2 BLADE (120 DEG)	2	6.5	5.25	Submergence Testing	4FEB_Test18	D2B120ST18	
4-Feb-22	1 - 2 BLADE (120 DEG)	2	7	5.25	Submergence Testing	4FEB_Test19	D2B120ST19	
4-Feb-22	1 - 2 BLADE (120 DEG)	2	2.5	T	N/A	4FEB_Test21	D2B120T11	
4-Feb-22	1 - 2 BLADE (120 DEG)	2	3.5	T	N/A	4FEB_Test22	D2B120T12	
4-Feb-22	1 - 2 BLADE (120 DEG)	2	4	T	N/A	4FEB_Test23	D2B120T13	
4-Feb-22	1 - 2 BLADE (120 DEG)	2	4.5	T	N/A	4FEB_Test24	D2B120T14	
4-Feb-22	1 - 2 BLADE (120 DEG)	2	5	T	N/A	4FEB_Test25	D2B120T15	
4-Feb-22	1 - 2 BLADE (120 DEG)	2	5.5	T	N/A	4FEB_Test26	D2B120T16	
4-Feb-22	1 - 2 BLADE (120 DEG)	2	6	T	N/A	4FEB_Test27	D2B120T17	
4-Feb-22	1 - 2 BLADE (120 DEG)	2	6.5	T	N/A	4FEB_Test28	D2B120T18	
4-Feb-22	1 - 2 BLADE (120 DEG)	2	7	T	N/A	4FEB_Test29	D2B120T19	
4-Feb-22	1 - 2 BLADE (180 DEG)	2	2.5	T	N/A	4FEB_Test31	D2B180T11	
4-Feb-22	1 - 2 BLADE (180 DEG)	2	3.5	T	N/A	4FEB_Test32	D2B180T12	
4-Feb-22	1 - 2 BLADE (180 DEG)	2	4	T	N/A	4FEB_Test33	D2B180T13	
4-Feb-22	1 - 2 BLADE (180 DEG)	2	4.5	T	N/A	4FEB_Test34	D2B180T14	
4-Feb-22	1 - 2 BLADE (180 DEG)	2	5	T	N/A	4FEB_Test35	D2B180T15	
4-Feb-22	1 - 2 BLADE (180 DEG)	2	5.5	T	N/A	4FEB_Test36	D2B180T16	
4-Feb-22	1 - 2 BLADE (180 DEG)	2	6	T	N/A	4FEB_Test37	D2B180T17	
4-Feb-22	1 - 2 BLADE (180 DEG)	2	6.5	T	N/A	4FEB_Test38	D2B180T18	
4-Feb-22	1 - 2 BLADE (180 DEG)	2	7	T	N/A	4FEB_Test39	D2B180T19	
7-Feb-22	1 -2 BLADE (90 DEG)	2	2.5	T	N/A	7FEB_Test1	D2B90T11	
7-Feb-22	1 -2 BLADE (90 DEG)	2	3.5	T	N/A	7FEB_Test2	D2B90T12	
7-Feb-22	1 -2 BLADE (90 DEG)	2	4	T	N/A	7FEB_Test3	D2B90T13	
7-Feb-22	1 -2 BLADE (90 DEG)	2	4.5	T	N/A	7FEB_Test4	D2B90T14	
7-Feb-22	1 -2 BLADE (90 DEG)	2	5	T	N/A	7FEB_Test5	D2B90T15	
7-Feb-22	1 -2 BLADE (90 DEG)	2	5.5	T	N/A	7FEB_Test6	D2B90T16	
7-Feb-22	1 -2 BLADE (90 DEG)	2	6	T	N/A	7FEB_Test7	D2B90T17	
7-Feb-22	1 -2 BLADE (90 DEG)	2	6.5	T	N/A	7FEB_Test8	D2B90T18	
7-Feb-22	1 -2 BLADE (90 DEG)	2	7	T	N/A	7FEB_Test9	D2B90T19	
7-Feb-22	1 -2 BLADE (60 DEG)	2	2.5	T	N/A	7FEB_Test11	D2B60T11	
7-Feb-22	1 -2 BLADE (60 DEG)	2	3.5	T	N/A	7FEB_Test12	D2B60T12	
7-Feb-22	1 -2 BLADE (60 DEG)	2	4	T	N/A	7FEB_Test13	D2B60T13	
7-Feb-22	1 -2 BLADE (60 DEG)	2	4.5	T	N/A	7FEB_Test14	D2B60T14	
7-Feb-22	1 -2 BLADE (60 DEG)	2	5	T	N/A	7FEB_Test15	D2B60T15	
7-Feb-22	1 -2 BLADE (60 DEG)	2	5.5	T	N/A	7FEB_Test16	D2B60T16	
7-Feb-22	1 -2 BLADE (60 DEG)	2	6	T	N/A	7FEB_Test17	D2B60T17	
7-Feb-22	1 -2 BLADE (60 DEG)	2	6.5	T	N/A	7FEB_Test18	D2B60T18	
7-Feb-22	1 -2 BLADE (60 DEG)	2	7	T	N/A	7FEB_Test19	D2B60T19	

7-Feb-22	1 -2 BLADE (60 DEG)	2	2.5	5.25	Submergence Testing	7FEB_Test21	D2B60ST11	
7-Feb-22	1 -2 BLADE (60 DEG)	2	3.5	5.25	Submergence Testing	7FEB_Test22	D2B60ST12	
7-Feb-22	1 -2 BLADE (60 DEG)	2	4	5.25	Submergence Testing	7FEB_Test23	D2B60ST13	
7-Feb-22	1 -2 BLADE (60 DEG)	2	4.5	5.25	Submergence Testing	7FEB_Test24	D2B60ST14	
7-Feb-22	1 -2 BLADE (60 DEG)	2	5	5.25	Submergence Testing	7FEB_Test25	D2B60ST15	
7-Feb-22	1 -2 BLADE (60 DEG)	2	5.5	5.25	Submergence Testing	7FEB_Test26	D2B60ST16	
7-Feb-22	1 -2 BLADE (60 DEG)	2	6	5.25	Submergence Testing	7FEB_Test27	D2B60ST17	
7-Feb-22	1 -2 BLADE (60 DEG)	2	6.5	5.25	Submergence Testing	7FEB_Test28	D2B60ST18	
7-Feb-22	1 -2 BLADE (60 DEG)	2	7	5.25	Submergence Testing	7FEB_Test29	D2B60ST19	
7-Feb-22	1 -2 BLADE (90 DEG)	2	2.5	5.25	Submergence Testing	7FEB_Test31	D2B60ST11	
7-Feb-22	1 -2 BLADE (90 DEG)	2	3.5	5.25	Submergence Testing	7FEB_Test32	D2B60ST12	
7-Feb-22	1 -2 BLADE (90 DEG)	2	4	5.25	Submergence Testing	7FEB_Test33	D2B60ST13	
7-Feb-22	1 -2 BLADE (90 DEG)	2	4.5	5.25	Submergence Testing	7FEB_Test34	D2B60ST14	
7-Feb-22	1 -2 BLADE (90 DEG)	2	5	5.25	Submergence Testing	7FEB_Test35	D2B60ST15	
7-Feb-22	1 -2 BLADE (90 DEG)	2	5.5	5.25	Submergence Testing	7FEB_Test36	D2B60ST16	
7-Feb-22	1 -2 BLADE (90 DEG)	2	6	5.25	Submergence Testing	7FEB_Test37	D2B60ST17	
7-Feb-22	1 -2 BLADE (90 DEG)	2	6.5	5.25	Submergence Testing	7FEB_Test38	D2B60ST18	
7-Feb-22	1 -2 BLADE (90 DEG)	2	7	5.25	Submergence Testing	7FEB_Test39	D2B60ST19	

THIS PAGE INTENTIONALLY LEFT BLANK

APPENDIX B:
MATLAB Code

B.1 Image Loading

```
%% Read Video
% script for loading *.mov video files
%
% Created by: Luksa Luznik and modified by S.M. Graham,
% United States Naval
% Academy
%
% This script reads video file into MATLAB. Videos of more
% than 1000 frames
% could cause MATLAB to run very slowly or crash
clear all close all
% Change the string in ('filename' ) to your movie file name
%----------------------------------------
readerobj = VideoReader('onebladedmedium_Trim.mp4');
%----------------------------------------
% extract info from the object
numFrames = get(readerobj, 'NumberOfFrames');
frequency = get(readerobj, 'Framerate');
duration = get(readerobj, 'Duration');
NoPixV = get(readerobj, 'Height');
NoPixH = get(readerobj, 'Width');

fprintf('Number of frames in the movie= %.0f\n',numFrames);
fprintf('Sampling Frequency = %.2f (Hz)\n',frequency);
fprintf('Video Duration Time = %.1f (s) \n',duration);
fprintf('Number of Horizontal pixels = %.0f  ...
Number of Vertical pixels = %.0f \n',NoPixH, NoPixV);
%% Upload selected frames

% Prompt user to enter first frame number to be analyzed
prompt = {'Enter first frame number to be analyzed'};
```

```
dlgtitle = 'First Frame';
definput = {'1'};
opts.Interpreter = 'tex';
answer = inputdlg(prompt,dlgtitle,[1 40],definput,opts);
FirstFrame = str2num(answer{1});

% Prompt user to enter last frame number to be analyzed
prompt = {'Enter last frame number to be analyzed'};
dlgtitle = 'Last Frame';
definput = {'100'};
opts.Interpreter = 'tex';
answer = inputdlg(prompt,dlgtitle,[1 40],definput,opts);
LastFrame = str2num(answer{1});
% Read video
video=read(readerobj,[FirstFrame LastFrame]);
% Note: read command will create a 4dimensional object
(matrix) with the following structure: [(Height Width 3),numFrames]

% if you run out of memory, reduce number of frames to load
% by changing
% [FirstFrame LastFrame] to something less

% define number of video frames for analysis
numFramesAnalysis = LastFrame-FirstFrame+1; % this should
match 2700-1700+1, since Matlab will take fist(1700th frame)

% Loop through all frames and read 3 frames corresponding to
% blue red and green for each frame (which is a time step) in
% movie sequence and
% create a sequence of grayscale images for further processing
for I=1:1:numFramesAnalysis % select number of frames
(numFrames) to read into matrix
RED =  video(:,:,1,I);
BLUE = video(:,:,2,I);
GREEN= video(:,:,3,I);
% combine 3 different frames into RGB
RGB = cat(3, RED,BLUE,GREEN);
% convert to greyscale
ImageGrey2(:,:,I) = rgb2gray(RGB);
fprintf('Creating Gray scale Image= %1.0f \n',I);
```

```
72 end
73 %get rid of original video object to manage memory for
74 % further processing
75 clear video
```

B.2 Image Analysis

```
%% Find Circle centers
% Find centroid of the black stickers using MATLAB
% "imfindcircles" function
% MATLAB function imfindcircles requires several inputs:
% 'Object Polarity' and 'dark' indicate to look for an object % that is
% dark in comparison to the background
% 'Sensitivity' indicates an input for the search algorithm
% of 0.95.

tic
for I=1:numFramesAnalysis

frame_analysis = ImageGrey2(:,:,I);

frame_analysis =imadjust(frame_analysis,[0 0.44],[1 .1],1);

 [centers,radii]=imfindcircles(frame_analysis,[25 50], ...
 'ObjectPolarity','bright','Sensitivity',0.85,'EdgeThreshold',.0125);

 % there is a high possibility that more than one object will % be found in
 % each frame, so constrains need to be placed on the "found" % objects
 % Objective is to find ONLY ONE sphere center in every
 % frame.
 % To accomplish this you will need to run this loop several
 % times and optimize
 % by changing range of radius input , e.g. [30 50],
 % or by changing Sensitivity value, e.g. 0.96 or 0.94 etc..
 %--------------------------------------
 % Additionally if more than one center is found, remove
 % obvious ones that are
 % off-center in the tube.
 % If no center is found flag with NaN at that time step.
 % you will need to run this loop several times and optimize
 % by changing range of radius input , e.g. [30 50], or by
 % changing Sensitivity value, e.g. 0.96 or 0.94 etc..

%  if length(centers) > 1 % if found more than 1 center
```

```
%     [rowsBelow]=find(centers(:,1)>150); % remove centers
% that do not make physical sense
%     [rowsAbove]=find(centers(:,1)<10);
%     rows=[rowsBelow' rowsAbove']';
%     centers(rows,:)=[];
%     radii(rows,:)=[];
%  end

 [noRows noColumns]=size(centers);

 if  noRows >= 2 % if still more than 1 centers interpolate
                 % to get one center
     centers = mean(centers,1);
     radii = mean(radii,1);
 else
     centers=centers;
     radii=radii;
 end

 if length(centers) == 0 % if no centers are found use NaN's
 % for placeholders
     centers =[NaN NaN];
     radii = NaN;
 end
 BallCenters(I,:)=centers;
 BallRadii(I)=radii;
 fprintf('Analyzing Image No#= %1.0f \n',I);
% ------------------------------------------------------------
% you can visualize centers by plotting each frame with
% superimposed "found" circles.
% Note that this visualizing portion will crash if NaN is
% found, i.e. if
% "imfindcircles" did not found a sphere center.
% For now I keep this visualizing part commented out
figure (1)
 image(frame_analysis,'CDataMapping','scaled');
 colormap('gray')
 axis image
 title(sprintf('Frame Number= %.0f;   CenterXLoc= %.1f
 (pixels);    CenterYLoc= %.1f (pixels)',I,
```

```
 BallCenters(I,1),BallCenters(I,2)), 'FontSize', 12);
 hold;
 % superimpose circle location on the image
  viscircles(centers, radii,'EdgeColor','b');
% %%%%%%%%%%%%%%%%%%%%%%%%%%%%%%%%%%%%%%%%%%%%%%%%%%%%%%%%%%%%%%%%%%%%%%%%%%%
end

%% Pre Processing
close all, clc
% Inputs
Hz = 30; % Frame Rate of video
D = 4.06; % tip to tip diameter

% Create Time Vector
delta_t = 1/Hz;
t = linspace(0,length(BallCenters)*delta_t,length(BallCenters))';

% Filter NaN's out of Data
[locations]=find(isnan(BallCenters(:,1))); % this will find
row numbers of times when the circle was not found

% now remove those locations
BallCenters_revised = BallCenters;
t_revised = t;
BallCenters_revised(locations,:)=[];
t_revised(locations) = [];

figure (2)
plot(BallCenters_revised(:,1),BallCenters_revised(:,2),'k.')
grid on
axis equal
title('Raw Data - UNITS: pixels')

[xc,yc,R,a] = circfit(BallCenters_revised(:,1),BallCenters_revised(:,2));

% Plot circular best fit
figure (3)
plot(BallCenters_revised(:,1),BallCenters_revised(:,2),'k.')
hold on
plot(xc,yc,'ro')
```

```
viscircles([xc yc],R)
title('Circular Best Fit')

% Calculate inches/pixel
inches_per_pixel = D/(2*R);
d = 2*R*inches_per_pixel;

% Find distance from center for all points
for i = 1:length(BallCenters_revised);
    element_radius(i) =
    sqrt(abs(BallCenters_revised(i,2)-yc)^2+abs(BallCenters_r
    evised(i,1)-xc)^2);
end

figure (4)
plot(element_radius,'k.')
hold on
plot([0 length(element_radius)],[R R],'r-')
hold off
title('Distance from Best Fit Center (Individual Radius')
xlabel('Index')
ylabel('Pixels')

% Locate times when imfindcircles gave bad data points
BallCenters_filtered = BallCenters_revised;
t_filtered = t_revised;
[locations]=find(abs(element_radius-R)>20); % this will find
% row numbers of times when the circle was not found
BallCenters_filtered(locations,:)=[];
t_filtered(locations) = [];

GoodData = zeros(length(t_filtered),3);
GoodData(:,1)=t_filtered';
GoodData(:,2)=BallCenters_filtered(:,1);
GoodData(:,3)=BallCenters_filtered(:,2);

figure (6)
plot(GoodData(:,2),GoodData(:,3))
axis equal
toc
```

B.3 Data Analysis

```
clear all

% Load File
load D1V8T15

% Wave Freq
wavefreq = 0.854;

% Circular Best Fit
[xc,yc,R,a] = circfit(GoodData(:,2),GoodData(:,3));

t = GoodData(:,1);
x = GoodData(:,2);
y = GoodData(:,3);

% FPS of camera
dt = 1/30;

% convert to polar coordinates
% put center of circle at origin
x = x - xc;
y = y - yc;

figure (1)
plot(x,y)
hold on
plot(x(1),y(1),'ro')
grid on, axis equal

% calculate angular position

for i = 1:length(x)
          if atan2(y(i),x(i))>=0
                a(i) = (180/pi) * atan2(y(i),x(i));
          else
                 a(i) = (180/pi) * (atan2(y(i),x(i))+2*pi);
          end
```

```
38 end
39
40 % find the big discontinuity and translate down
41 for i = 2: length(x);
42 difference(i) = a(i)-a(i-1);
43 end
44
45 [max_d,element] = max(difference);
46 [d,el] = find(difference > 180);
47
48 for i = 2:length(x)
49        if a(i)-a(i-1)>100
50            a(i) = a(i)-360;
51        elseif a(i)-a(i-1)<-100
52            a(i) = a(i)+360;
53        else a(i) = a(i);
54        end
55 end
56
57 % What if there was more than one jump?
58 % repeat to find more errors if it was hovering around x-axis
59
60 figure (2)
61 plot(t,a)
62
63 % calculate angular position relative to zero
64
65 for i = 2:length(x)
66     theta(1) = 0;
67     theta(i) = -a(i)+a(1);
68 end
69
70 figure (3)
71 plot(t,theta,'linewidth',2)
72 xlabel('Time (sec)')
73 ylabel('Degrees of Rotation')
74 hold on
75
76 % Find time for one full rotation
77 one_full = find(theta>360);
```

```
[cross,time] = min(one_full);

time_rotation = t(one_full(time));

% angular velocity
for i = 2:length(theta);
     omega(i) = (theta(i)-theta(i-1))/(t(i)-t(i-1));
end

figure (4)
plot(t,omega)

[FilteredDataVector] =
function_DigitalFilter(t,omega,wavefreq);

hold on
plot(t,FilteredDataVector)

% find frequency of velocity data
[pks,locsP] = findpeaks(FilteredDataVector);
[trf,locsT] = findpeaks(-FilteredDataVector);

figure (5)
plot(t,FilteredDataVector)
hold on

for k = 2:length(locsP);
frequency_exp(k-1) = 1./(t(locsP(k))-t(locsP(k-1)));
end

frequency_ave = mean(frequency_exp);

% Find the velocity per position
figure (6)

start_point = 270 - a(1);
a_plot = theta+start_point;
plot(a_plot,FilteredDataVector,'.')
hold on
xlabel('Degrees')
```

```
ylabel('Angular Velocity (Deg/sec)')

% Find the average speed over one full rotation
% remove time and filtered velocity elements past one full
% rotation
t_avgspd = t;
FilteredDataVector_avgspd = FilteredDataVector;

[max_theta,maxloc] = max(theta);

if max(theta)-theta(1)<360
     avgspd_TIME_FULL =
     trapz(t_avgspd,abs(FilteredDataVector_avgspd))./t(end)
else
    FilteredDataVector_avgspd =
    FilteredDataVector_avgspd(1:one_full(1));
    t_avgspd = t_avgspd(1:one_full(1));
    avgspd_TIME_FULL =
    trapz(t_avgspd,abs(FilteredDataVector_avgspd))./time_rota
    tion
end

% average full speed using time until right before blind spot
% find where the blind spot is

for i = 2:length(t)
   diff_t(i-1) = t(i)-t(i-1);
end

[blindspot,bsloc] = max(diff_t);

t_avgspd = t;
FilteredDataVector_avgspd = FilteredDataVector;

if max(theta)-theta(1)<360
    avgspd_TIME_BS =
    trapz(t_avgspd,abs(FilteredDataVector_avgspd))./(t(end)-t
    (1))
else
    FilteredDataVector_avgspd(bsloc+1:end)=[];
```

```
158     t_avgspd(bsloc+1:end) = [];
159     avgspd_TIME_BS =
160     trapz(t_avgspd,abs(FilteredDataVector_avgspd))./(t(bsloc)
161     -t(1))
162 end
163 % Find the average speed using the position plot now ONE FULL
164 % ROTATION
165 a_plotp = a_plot;
166 FilteredDataVector_avgspdp = FilteredDataVector;
167
168 if max(theta)-theta(1)<360
169     avgspd_POS_FULL =
170     trapz(a_plotp,abs(FilteredDataVector_avgspdp))./(a_plot(e
171     nd)-a_plot(1))
172 else
173     FilteredDataVector_avgspdp(one_full(2:end))=[];
174     a_plotp(one_full(2:end)) = [];
175     avgspd_POS_FULL =
176     trapz(a_plotp,abs(FilteredDataVector_avgspdp))./(a_plot(o
177     ne_full(1))-a_plot(1))
178 end
179 % average full speed using position plot until right before
180 % blind spot
181 a_plotp = a_plot;
182 FilteredDataVector_avgspdp = FilteredDataVector;
183
184 if max(theta)-theta(1)<360
185     avgspd_POS_BS =
186     trapz(a_plotp,abs(FilteredDataVector_avgspdp))./(a_plot(e
187     nd)-a_plot(1))
188
189 else
190     FilteredDataVector_avgspdp(bsloc+1:end)=[];
191     a_plotp(bsloc+1:end) = [];
192     avgspd_POS_BS =
193     trapz(a_plotp,abs(FilteredDataVector_avgspdp))./(a_plot(b
194     sloc)-a_plot(1))
195 end
```

List of References

[1] R. K. Nichols, J. Ryan, H. C. Mumm, W. D. Lonstein, C. M. Carter, J. Shay, R. Mai, J. P. Hood, and M. Jackson, "UUV integrated autonomous missions and drone management," *Unmanned Vehicle Systems & Operations On Air, Sea, and Land*, 2020.

[2] B. Drew, A. R. Plummer, and M. N. Sahinkaya, "A review of wave energy converter technology," *Proceedings of the Institution of Mechanical Engineers, Part A: Journal of Power and Energy*, vol. 223, no. 8, pp. 887–902, 2009.

[3] "Triboelectric Nanogenerator." MRSEC Education Group. [Online]. Available: https://education.mrsec.wisc.edu/triboelectric-nanogenerator/.

[4] "Triboelectricity." Tribonet. [Online]. Available: https://www.tribonet.org/wiki/triboelectricity/.

[5] J. Wang, L. Zhou, C. Zhang, and Z. L. Wang, "Small-scale energy harvesting from environment by triboelectric nanogenerators," *A Guide to Small-Scale Energy Harvesting Techniques*, 2020.

[6] J. Capelle, "Rotational motion triboelectric nanogenerators (TENG)," Ph.D. dissertation, Naval Postgraduate School, 2020.

[7] H. Akimoto, Y. Kim, and K. Tanaka, "Configuration of the single-bucket wave turbine for the direct utilization of orbital fluid motion," *Grand Renewable Energy*, 2014.

[8] "Wave Devices." EMEC European Marine Energy Centre. [Online]. Available: http://www.emec.org.uk/marine-energy/wave-devices/

[9] U. Khan and S.-W. Kim, "Triboelectric nanogenerators for blue energy harvesting," *ACS Nano*, vol. 10, no. 7, pp. 6429–6432, 2016.

[10] "Can Renewable Energy Sources Power the World?" OpenLearn. [Online]. Available: https://www.open.edu/openlearn/ocw/mod/oucontent/view.php?id=73762\protect\T1\textsectionion=8

[11] Y.-D. Choi, C.-G. Kim, Y.-T. Kim, J.-I. Song, and Y.-H. Lee, "A performance study on a direct drive hydro turbine for wave energy converter," *Journal of Mechanical Science and Technology*, vol. 24, no. 11, pp. 2197–2206, 2010.

[12] "Waterotor." Waterotor Energy Technologies Inc. [Online]. Available: https://waterotor.com/

[13] M. Irwin. (2021). ”Japanese Turbines Catch the Waves to Harvest Energy and Protect the Coastline".” New Atlas. [Online]. Available: https://newatlas.com/wave-energy-turbines-tetrapods/51472/

[14] N. R. Maldar, C. Y. Ng, L. W. Ean, E. Oguz, A. Fitriadhy, and H. S. Kang, “A comparative study on the performance of a horizontal axis ocean current turbine considering deflector and operating depths,” *Sustainability*, vol. 12, no. 8, p. 3333, 2020.

[15] ”Triton WEC.” Oscilla Power. [Online]. Available: https://www.oscillapower.com/technology

[16] Y. Pei and Z. Mu, “The study on performance of drag based water turbine under non-immersive condition,” in *E3S Web of Conferences*. EDP Sciences, 2019, vol. 107, p. 01005.

Initial Distribution List

1. Defense Technical Information Center
   Ft. Belvoir, Virginia

2. Dudley Knox Library
   Naval Postgraduate School
   Monterey, California